Photothermal effects in micro/nano electromechanical systems

by

Naresh Miriyala

A thesis submitted in partial fulfillment of the requirements for the degree of

Doctor of Philosophy

in

Materials Engineering

Department of Chemical and Materials Engineering

University of Alberta

Abstract

Micro and nano electromechanical sensors have been explored for various applications as highly sensitive mass sensors up to a mass resolution of a single proton and even down to a level of yoctogram mass. Such gravimetric sensors lack intrinsic selectivity and typically rely on the chemo-selective interfaces which add complexity and give irreproducible results due to unspecific and weak nature of intermolecular interactions. On the other hand, spectroscopy techniques are simple, highly selective and provide molecular identification even in complex mixtures hence, they are widely explored in basic sciences. Conventional IR spectroscopy in the mid-IR range provides information on molecular vibrations that result in a sample-specific absorption spectrum, a so-called molecular fingerprint but, unfortunately, they suffer from erratic signals in case of the small quantity of samples ($\approx$ ng mass) and weak IR absorbing analytes. In contrast, photothermal spectroscopy techniques are highly sensitive and offer a direct way of measuring optical absorption keeping it away from scattering and reflection losses that interfere with signals. The basis of the photothermal technique is the photo-induced change in the thermal state of the sample.

The aim of this Ph.D. project is to explore the innovative and unexplored design of sensors to obtain spectroscopic information from trace amounts of mass ($\approx$ fg) and weak IR absorbing analytes such as liquids. To achieve this goal, two types of unexplored micro/nano mechanical resonators have been investigated; namely, a novel design of bimaterial microchannel cantilevers (BMC) that can contain picoliter volumes of liquid and nanomechanical string resonators. As temperature or heat is the external stimulus in spectroscopy, these sensors are treated as thermal sensors. Detailed theoretical and experimental investigations were carried out in optimizing the most influential parameters and understanding the basic thermomechanical behavior of these sensors. Photothermal spectroscopy applications are demonstrated with an improved sensitivity to obtain the chemical identity from trace amounts of samples. Efforts are made to observe the photothermal effect on functional material suspended nanowires such as $BiFeO_3$ (BFO) and in the process we have explored many interesting and anomalous photo properties of BFO under visible light. The underlying concept of all these devices presented in this thesis is the extremely low mass of the devices that makes them susceptible to minute changes in added mass and heat flux. Insights were drawn to extend the applications of these devices not just limited to nanomechanical IR photothermal spectrometry but also to use them as thermo-analytical tools.

Preface

The majority of the current thesis represents my ideas in my own words and where others ideas have been included, I have adequately cited and referenced the original sources. This research is supported by the Canada Excellence Research Chairs (CERC) program. The devices used in Chapter 3 and Chapter 4 were provided by Dr. Faheem Khan and Maryam Ghorashi from our group. All the experiments and analysis was performed by me in the case of Chapter 3. For Chapter 4, I was involved with Dr. Faheem Khan to develop the idea, conduct experiments and to analyze the results. Some of the research conducted for this thesis forms part of a research collaboration with Prof. John Davis from Department of Physics at the University of Alberta. Nanomechanical string devices and associated experimental set up used in Chapter 5 and Chapter 6 were provided by Tushar S Biswas, a student of Prof. John Davis. The complete thermomechanical analysis presented in Chapter 5 was my original work. We have conceived the idea, arranged mid-IR laser, deposited analytes, involved in experiments and analysis for the results presented in Chapter 6. The contents in Chapter 7 are my own work with the assistance from Dr. Kovur Prashanthi.

I declare that the contents of Chapter 6 of this thesis have been published in Analytical chemistry, 86(22):1136811372, 2014. All the figures used in this chapter are reprinted with permission from Analytical chemistry, 86(22):11368-11372. Copy right 2014 American Chemical Society. A section of Chapter 7 has been published in Physica status solidi (RRL) Rapid Research Letters, 7(9):668-671, 2013.

Dedication

To my awesome parents
and
uncle Dr. J. Jayanth Kumar

Mom, thank you for being such a source of inspiration and happiness. You are the reason for whatever I am today. Love you amma.

Acknowledgments

I would like to express my sincere gratitude to my supervisor Prof. Thomas Thundat who introduced me to the beautiful wonderland of research. I am greatly indebted for his constant support, encouragement, valuable guidance, insightful discussions and evaluation of my work throughout the doctorate journey. Without his support, this thesis would have not possible.

I would like to thank the members of my supervisory committee, Dr. Ken Cadien, and Dr. Weixing Chen, for their valuable inputs in the thesis and support during tough times.

I acknowledge Dr. John P Davis and his student Tushar Biswas from the department of Physics, the University of Alberta for providing nanomechanical string resonators and associated experimental setup.

I would like to thank my group members Dr. Faheem Khan and Maryam Ghoraishi for providing novel microchannel embedded microcantilever resonators and their support in lab activities.

I would like to acknowledge Canada Excellence Research Chair (CERC) program and the department of Chemical and Materials Engineering at University of Alberta for providing me the opportunity to do research and for the financial support during my program. I am greatly thankful to all personnel at Nano Fab, National Institute for Nanotechnology (NINT), Alberta Centre for Surface Engineering & Sciences (ACSES) and Oil Sands and Coal Interfacial Engineering Facility (OSCIEF) during the course. I am grateful to all the Chemical and Materials Engineering department office staff, machine shop staff, and IT personnel for their generous help at different stages.

I am thankful to all past and present members of Nano Interface and Molecular Engineering (NIME) group for their co-operation and useful discussions. I would like to thank Dr. Prashanthi Kovur from NIME group, for her overwhelming support at various occasions personally and professionally. I would like to thank Dr. Sam Kim, Dr. Dongkyu Lee, and Dr. Charles for their help and support. I would like to acknowledge the support of Behnam in analytical studies. Special thanks to Dr. Lana Norman, Dr. Shawn, Dr. Ravi Gaikwad, Dr. Ankur Gosami, Priyesh and Tinu Abraham for cheering me up every time I was feeling depressed. I express my special thanks to my friends Dr. Nagasiva Kumar Gunda, Ranjit Alampally, Dr. Mayank Pande, Nitya Iyer, Pankaj Kumar Sahu and Atreya Nitalla for the fun times and for making my stay memorable.

Finally, I would like to express my sincere thanks to my parents and my family members for their unconditional love, encouragement and understanding.

Contents

List of Figures

List of Tables

List of Abbreviations

- 1D: one-dimensional
- AAO: Anodized aluminum oxide
- AFM: Atomic force microscopy
- BFO: $BiFeO_3$
- BMC: Bimaterial microchannel cantilever
- DLE: Defect level emission
- DMMP: Dimethyl methylphosphonate
- EBL: Electron beam lithography
- EDS: Energy dispersive X-ray spectroscopy
- FTIR: Fourier transform infrared
- GHz: Giga Hertz
- IC: Integrated chip
- IR: Infrared
- LDV: Laser doppler vibrometer
- LOD: Limit of detection
- LOR: Limit of recognition
- LPCVD: Low-pressure chemical vapor deposition

- MB: Methylene blue
- MEMS: Microelectromechanical systems
- NBE: Near band emission
- NEF: Noise equivalent flux
- NEMS: Nanoelectromechanical system
- NEP: Noise equivalent power
- NETD: Noise equivalent temperature detection
- NPs: Nanoparticles
- NTA: Nanothermal analysis
- NTs: Nanotubes
- NWs: Nanowires
- ORNL: Oak ridge national laboratory
- PCA: Photocatalytic activity
- PCDS: Photothermal cantilever deflection spectroscopy
- PL: Photoluminescence
- PLL: Phase lock loop
- POC: Point of care
- PSD: Position sensitive detector
- PVP: Polyvinylpyrolidene
- PZT: $PbZrTiO_3$
- QCL: Quantum cascade laser
- QTF: Quartz crystal tuning fork
- SAM: Self assembled monolayer

- SEM: Scanning electron microscopy
- SiN: Silicon nitride
- SiNx: Silicon nitride
- SMR: Suspended microchannel resonator
- SNR: Signal to noise ratio
- SRN: Silicon rich nitride
- TEM: Transmission electron microscopy
- XPS: X-Ray photoelectron spectroscopy
- XRD: X-Ray diffraction

Chapter 1

Introduction

Microfabricated sensors are promising as excellent gravimetric sensors due to their minuscule mass, miniature size, high sensitivity, portability, low cost and low power consumption [1]. Rapid advancements in microfabrication found many applications in sensing such as national security [2], forensics, environment monitoring [3], as miniaturized analytical tools and human health care applications [4]. In all these applications, detection, speciation, and quantification of extremely small concentrations of analytes is vital. A race to the bottom ensued with demonstrations of ever better levels of sensitivities from femtogram (10^{-15} g) [5] to sub zeptogram (10^{-22} g) [6] mass measurements. Recently, an unprecedented mass sensitivity of weighing up to a single proton (yocto gram(10^{-24} g)) [7] has been achieved using these devices by further miniaturization. Microfabricated sensors offer potential platforms for label-free detection of trace quantities of mass for quantitative measurements. Among all the microfabricated sensors, microcantilevers [8] and microstrings [9] were explored as excellent gravimetric sensors due to their high susceptibility to added mass and relatively easy detection systems developed. Underlying these advances are the minuscule mass of the device and capability to attain high-quality factors, making them extremely sensitive to adsorbed mass, surface stress, refractive index, resistance, capacitance and temperature [10]. Despite having many advantages, these sensors suffer from poor chemical selectivity thus limiting the real-time applications. Real-time applications demand more stringent conditions such as extremely high sensitivity in the case of volatile explosive detection, detection of a specific analyte in a mixture, in the presence of liquid environment, repeatability, high dynamic range, high measurement throughput, regeneration of surface and stability [11]. This thesis is emphasized on attributing chemical selectivity to cantilevers like micromechanical structures and nanomechanical strings.

1.1 Motivation

So far, chemical selectivity in sensing has been achieved by providing immobilized chemoselective interfaces, that have high affinity to a specific analyte under investigation [12]. However, the process of immobilization and immobilization protocols are not only cumbersome but also, in most instances pose a threat to damage the device. In reality, they can only provide partial selectivity due to unspecific nature and weak chemical binding (mostly hydrogen binding), resulting in unacceptable levels of false positives. This scenario becomes worse in the detection of the analyte in a mixture due to interference between signals from different analytes [13]. An array of sensors with each device having an affinity to a specific analyte has been proposed to overcome chemical detection in a mixture. But individual immobilization, surface functionalization efficiency, and different immobilization protocols to each device make it challenging in real time applications. Moreover, once the sensor surface is functionalized, it is difficult to regenerate the surface for other uses and separate regeneration methods have to be incorporated making it more difficult to operate in real time [14]. In addition to these challenges, the trace amounts of analytes reaching the sensor surface and bio-sensors operated in the liquid environment make it further difficult to realize a field deployable sensor [15]. In the immediate need of addressing chemical selectivity, spectroscopic techniques based on unique molecular vibrational transitions in the mid Infrared (IR) molecular fingerprint regime appears to be a worthwhile investigation [16]. Hence, we chose to combine high thermal sensitivity of microfabricated sensors with highly selective mid-IR spectroscopy techniques to obtain molecular signatures from trace amounts of analytes. In this thesis, efforts were made to explore two new sensing platforms as thermal sensors, provided a detailed theoretical and experimental investigations about thermal sensitivity and demonstrated molecular signature from the minimum recognizable amounts on a sensor surface. A similar concept has been extended to fabricate ultra-low thermal mass, suspended nanostructures of a functional material and investigated the photo effects of that material.

1.2 Objective and methodology

The current thesis emphasizes chemical identification from extremely small amounts of analytes on a sensor surface. Photothermal spectroscopy has been identified as an alternative technique for molecular recognition that can be combined with highly sensitive gravimetric sensors to give quantitative and qualitative information about the analytes. As photothermal spectroscopy involves investigation of photoinduced change in thermal state of the material, the current sensing platforms are explored as thermal sensors [17]. Two novel sensing platforms namely, bimaterial microchannel cantilevers (BMC) and nanomechanical strings were investigated as thermal sensors. Though bimaterial cantilevers are explored as excellent thermal sensors, the real time application for biosensing is still a challenging task due to heavy damping because of the presence of liquid around. The innovative approach of having liquid inside the cantilever not only solves the problem of over damping in fluid based mass sensing but also provides a sensitive platform for the fundamental studies of fluid-particle interactions [18]. One of the objectives of the current thesis is to explore these novel BMC platforms as thermal sensors to find out the minimum fluid based mass detection possible through photothermal spectroscopy. In this thesis, the photo induced thermal changes, heat transfer to and from the sensor surface and most influential parameters effecting the sensitivity have been investigated in detail. The BMCs were fabricated by Dr. Faheem khan and Maryam Ghorashi, from our group. I hereby acknowledge their support and encouragement. In the case of BMC, the static deflection of BMC was considered as dependent parameter against IR wavenumber. Though the innovative design of BMC is a bit bulky in terms of mass, they are very well suited for biosensing applications.

Recently unprecedented mass sensitivity has been achieved using silicon nitride nanomechanical string resonators. Underlying these advances is the high susceptibility to added mass that is characteristic of miniaturization and ultra-high quality factors due to excess pre-stress [19]. The other objective of the current thesis is to investigate the dynamic thermomechanical response of nanomechanical strings under periodic IR radiation and to demonstrate molecular signature from lowest mass on string surface possible. Nanomechanical strings were fabricated by Tushar Biswas from Prof John Davis group. The nanomechanical string work was carried out in collaboration with Dept of Physics at the University of Alberta. The same concept of low thermal mass has been extended to fabricate suspended functional material nanostructures. Though we pursued our interest in anomalous photo properties of chosen $BiFeO_3$ (BFO) functional material, efforts are underway to explore it as novel sensing platform. In summary the objectives of current thesis are

- To explore the novel design of BMC as a thermal sensor to achieve detectable molecular signature from lowest analyte possible.
- To explore the dynamic thermomechanical response of nanomechanical string res-

onators to demonstrate femtogram level molecular signature.

- To explore anomalous photo behavior of BFO nanostructures under visible light and to extend possible applications in terms of sensing and photocatalysis.

1.3 Organization of the Thesis

This thesis has been organized according to articles published in journals or manuscripts submitted to journals. The guide lines from Faculty of Graduate Studies and Research (FGSR) at the University of Alberta have been followed to prepare this thesis. This thesis consists of eight chapters.

Chapter 1 (the present chapter) serves as the introduction to the thesis and provides the central motivation and objectives of the thesis.

Chapter 2 has been introduced with the basics of microfabricated sensors. Among all, microcantilevers and nanomechanical strings are given prime focus. The existing problem of chemical selectivity has been discussed in detail. The fundamentals of photothermal spectroscopy and its advantages over conventional IR spectroscopy has been presented. Detailed theoretical knowledge has been provided to explore microcantilevers and nanomechanical strings as thermal sensors. Special focus has been given to discuss various aspects in the literature of photothermal spectroscopy using MEMS. A brief introduction to photo effects on functional nanostructures was presented.

Chapter 3 investigates the thermomechanical response of a BMC subjected to periodic heating by IR radiation. Detailed theoretical and experimental study was performed considering BMC as a thermal sensor. Experiments were conducted to find out the thermal sensitivity and power sensitivity of various designs of BMC to optimize various parameters affecting the performance of BMC. We report a minimum measurement of 60 μW of power, the energy resolution of $\approx$ 240 nJ and temperature resolution of 4 mK using BMC. The best design of BMC was chosen to demonstrate a spectroscopy application to detect a minimum of 1.15 ng of ethanol in the ethanol-water binary mixture. We estimate that we can detect molecular signature from hundreds of picograms of the sample, in the presence of liquid. This chapter demonstrates molecular identification to the highly sensitive suspended microchannel resonator (SMR) platform using photothermal spectroscopy techniques.

Chapter 4 investigates dynamic thermal properties of picoliter volumes liquids using a BMC. The thermomechanical behavior of liquid filled BMC is not only affected by the device mechanics but also on the thermal properties of the constituents. This chapter emphasizes on the versatility of the BMC platform not just for mass sensing, selectivity by photothermal techniques but also as a thermoanalytical tool to investigate thermal transport behavior in confined geometries using picoliter fluid samples. Different liquid filled BMC resulted in different thermal behavior as demonstrated due to the difference in their molar thermal diffusivity. This chapter serves as the basic demonstration to investigate nanoscale thermal transport in liquids and nanofluids.

Chapter 5 investigates the dynamic thermomechanical response of a nanomechanical string subjected to periodic heating by IR radiation. Detailed theoretical and experimental study was performed considering the string as a thermal sensor. Experiments were conducted to find out the thermal sensitivity and power sensitivity of various geometries of string to optimize various parameters affecting the performance. We report a minimum measurement of 35 picowatt of power, the energy resolution of $\approx$ 26 fJ and temperature resolution of 0.27 mK using silicon nitride nanomechanical string.

Chapter 6 demonstrates an application to detect the molecular signature from trace amounts of sample present on the surface of the nanomechanical string using photothermal techniques. Here we report, the molecular signature from a femtogram level mass of an explosive material (RDX). RDX has been physisorbed onto the string by thermal evaporation for a very little time (4 min). The thermomechanical frequency detuning of the string with RDX on it, when subjected to mid-IR has been monitored with respect to the wavelength of radiated IR. The desorption characteristics of RDX in a moderate vacuum are also investigated. Efforts are underway to improve the recognition limit by fabricating smaller cross sectional area nanomechanical strings by electron beam lithography (EBL).

Chapter 7 demonstrates the photo effects on a functional material namely BFO nanostructures. Chapter 7 has been started with an intent of extending the low thermal mass effects to fabricate a nanoscale sensor made by suspending BFO nanowire and subjected to IR radiation. In the process, we found the anomalous behavior of the nanostructures to visible light. This anomalous photo behavior has been studied extensively and demonstrated an application of enhanced photocatalytic activity from BFO nanotubes in visible light. Efforts are underway to make this suspended BFO nanowire platform as a nanoscale sensor.

Finally, Chapter 8 draws conclusions of the thesis with important observations and introduces possible directions for future work.

Chapter 2

Literature

Microfabricated microelectromechanical systems, generally referred as MEMS have played vital roles in many important areas of sensing such as transportation, communication, automated manufacturing, environmental monitoring, health care, defense systems, and a wide range of consumer products. MEMS are inherently small, thus offering attractive characteristics such as reduced size, weight, low power dissipation, improved speed and precision compared to their macroscopic counterparts. The underlying fabrication of these devices uses the well known Integrated Circuit (IC) technology such as Complimentary metal oxide (CMOS), Field-effect transistors (FET) and in addition with some new etching, bonding and assembly techniques [20]. Some of the commercially successful MEMS devices include accelerometers, gyroscopes and micromirrors in Digital light processing (DLP) technology. In general, smaller a device, more susceptible are its physical properties to perturbation by external influences. Thus miniaturized MEMS-based sensors are highly sensitive, portable, inexpensive and suitable for real time applications such as Point of Care (POC), homeland security, defense, and environment monitoring. MEMS-based sensors such as pressure sensors, inertial sensors, force sensors, proximity sensors, chemical, and biosensors have been the key elements in many areas of development. Moreover, these sensors are so versatile that they can be operated in various modes to yield different information that is very difficult to achieve by conventional methods [21]. The working device in a MEMS can be a micrometer sized cantilever, diaphragm, mictostring, microbridge, micromirror and a micropore. The rapid growth in the IC fabrication technologies offers the ability to fabricate novel, innovative designs of MEMS devices along with creative designs on the existing platforms [22]. The current thesis focuses on an innovative design of cantilever geometry and string geometry.

2.0.1 Important parameters in sensor technology

As per IUPAC definition, a chemical sensor is a device that transforms chemical information ranging from the concentration of a specific sample component to total composition analysis, into an analytically useful signal. The chemical information, mentioned above, may originate from a chemical reaction of the analyte or from a physical property of the system being investigated [23]. Some of the common terminologies in the field of sensors are as follows

- Sensitivity is the change of measured signal per unit analyte concentration. It is effectively the slope of the calibration graph.
- Selectivity is the characteristic of a sensor to respond to one particular group of analytes or even for one particular analyte in a mixture.
- Limit of detection (LOD) is the lowest concentration of analyte that can be detected by the sensor under given conditions of temperature and pressure.
- Dynamic range is the span of upper and lower limits of analyte concentration that can be detected by the sensor.
- Resolution is the lowest concentration difference that can be distinguished by the sensor.
- Response time is the time required for the sensor to respond to a step concentration change from zero to a certain value.
- Recovery time is the time required for a sensor to reach to the initial position after the change from a certain value to zero.
- Linearity is the relative deviation of an experimentally determined calibration graph to that of an ideal straight line
- Stability is the ability of a sensor to give repeatable and reproducible results for a certain period of time.
- Limit of recognition (LOR) is the maximum recognizable mixture composition range.

2.1 Microcantilever based chemical sensors

The advent of atomic force microscopy (AFM), introduced in 1986 by Binning et al. has been an important milestone in nanoscience and technology, it has also fueled a revived interest in microfabrication and plethora of applications in MEMS [24]. At the heart of an AFM is a microcantilever which acts as a transducer for its numerous imaging modes like topography, electric potential, magnetic and force imaging. From the experience of using AFM cantilevers as extremely sensitive platforms for various external influences, Thomas Thundat and co-workers at Oak Ridge National Laboratory (ORNL) started to explore the potential of the microcantilever as physical and chemical sensors in 1994 [25]. The initial work of cantilever based sensing demonstrated that a metal coated microcantilever is extremely sensitive to humidity and other vapors such as mercury [26]. The cantilever platform not only sensitive but also gives accurate information on the amount of adsorbates and their physiochemical changes by monitoring the resonance frequency of the cantilevers. There are a number of cantilever configurations (eg. with and without intrinsic stress, silicon vs polymer, diving boards vs 'V' shaped) designed for various applications (IR sensing, chemical sensing, and biosensing) [27]. Within each sensing paradigm, there are different implementation principles (eg., for chemical sensing, one can sense induced stress, weight change, reflectance change and so on). This versatility of different operating modes to extract different information makes the microcantilever geometry unique and the most appreciable device among all the MEMS devices.

2.1.1 Basic modes of operation and detection

There are two basic modes of operation for a microcantilever -based sensor, namely static mode (the physical deflection of the microcantilever) and dynamic mode (changes in resonance characteristics). In static mode, differential adsorption of molecules (molecules adsorbed on only one side) causes the microcantilever to deflect due to increase in interfacial stress. Each mode is specific for certain application and differ from each other in terms of transduction and detection. Schematic of various modes has been shown in Fig. 2.1

The static deflection mode is mainly used for measuring surface stress due to differential adsorption of molecules on one face of the cantilever. Specific molecular adsorption can be initiated by functionalizing one face of the cantilever relative to other [28]. The flexural behavior of the microcantilever due to molecular adsorption is controlled by its spring

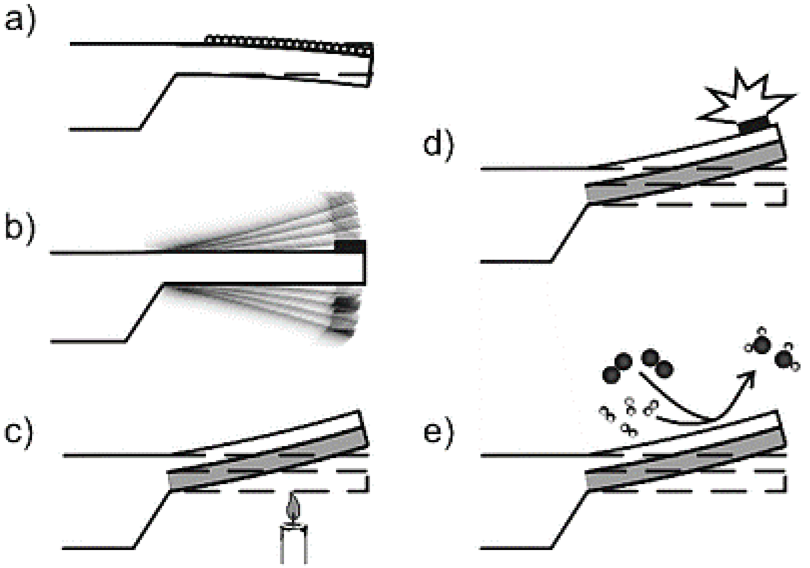

Figure 2.1: Schematic representation of various modes of operation of microcantilevers: a) Surface stress due to absorption of molecules causing static deflection. b) Dynamic resonance frequency shift mode due to change in effective mass. c) Heat sensing mode due to differential thermal expansion. d) Deflagration of explosive on the heated microcantilever surface. e) catalytic reaction on the cantilever surface [14]. Reproduced with permission from [14]. Copy right 2008 John Wiley and Sons.

constant k which in turn depends on the Young's modulus(E) and cantilever dimensions and magnitude of surface stress ($\delta\sigma$). For a rectangular cantilever of length l, width w and thickness t the spring constant is calculated as follows

$$k = \frac{Ewt^3}{4l^3} \tag{2.1}$$

Typical spring constant for silicon microcantilever of length several hundred micrometers and thickness below 1 μm fall in the range of 0.001 to 0.1 N m^{-1} [29]. Assuming uniform surface stress ($\delta\sigma$) as a cause for cantilever bending, the shape of the bent microcantilever can be approximated as a part of a circle of radius of curvature R given by Stoney's equation

$$\frac{1}{R} = \frac{6(1-\nu)}{Et^2}\delta\sigma \tag{2.2}$$

where ν is the Poisson's ratio ($\nu_{Si} = 0.24$). The above equation is only valid for thin functionalization layer (much thinner than the thickness of the microcantilever) [30].Static deflection operation is possible in various environments such as vacuum, ambient and fluid. This mode has been used to detect prostate specific antigen (PSA) [4], antibody-antigen interactions [31], DNA binding and other biosensing applications [32]. Typically surface stress changes of the order of 10^{-3} to 10^{-6} can be measured. Schematic representation of microcantilever deflecting in static mode under surface stress has been depicted in Fig. 2.2.

In dynamic mode, the cantilever is monitored for its resonance frequency characteristics such as frequency, amplitude, Q factor, and phase. The resonant frequency of a cantilever depends on its elastic properties such as effective mass and spring constant ($f_0 = \frac{1}{2\pi}\sqrt{\frac{k}{m}}$). Any small changes in the mass of the vibrating cantilever can drastically change its frequency and associated parameters [33]. Thus microcantilevers are extremely sensitive gravimetric (mass) sensors in the range of attogram (10^{-18} g) to zeptogram (10^{-21} g) range [34]. The mass change on a rectangular microcantilever at the end of the cantilever during molecular adsorption can be calculated as follows

$$\delta m = \frac{k}{4\pi^2 n} * (\frac{1}{f_0^2} - \frac{1}{f_1^2}) \tag{2.3}$$

where n is a geometric parameter 0.24 for rectangle cantilevers and f_1 is the eigenfrequency after mass adsorption. The above equation is valid assuming the molecule on the surface is in dynamic equilibrium with the molecule in the environment and no significant

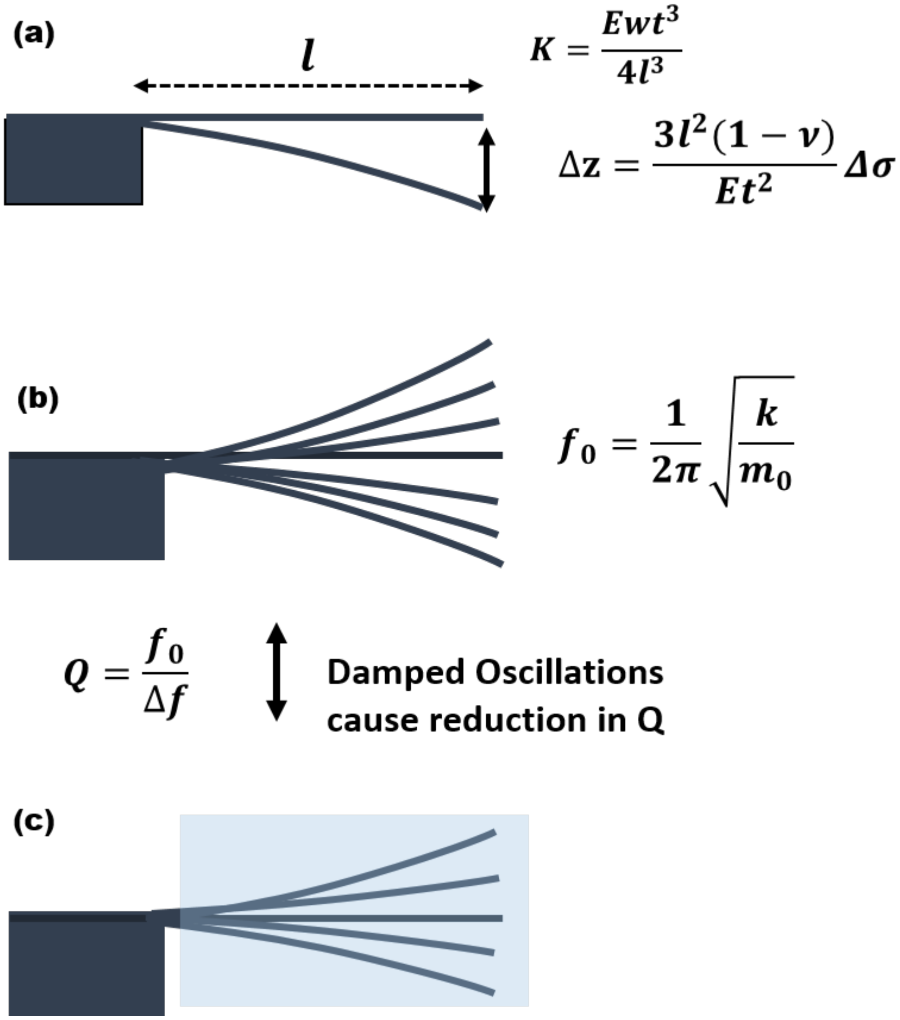

Figure 2.2: (a) Schematic representation of microcantilever deflecting in static mode under surface stress. (b) Microcantilever oscillating at fundamental frequency f_0. (c) Viscous damping for under-liquid operation along with corresponding parameters.

changes in the thickness and Young's modulus during molecular adsorption [25].

The dynamic mode works effectively in the gas environment where damping is minimized and remains constant. However, in the liquid environment for bio-applications, this approach suffers from substantial damping to the resonator oscillations due to the increase in drag forces of surrounding medium, thus reducing the quality factors down to below 30 (normally it is 100-1000 in air). Under these conditions, the frequency change resolution suffers badly affecting the sensitivity dramatically.

In order to overcome these damping issues, Burg et al. have devised an innovative design of having a microchannel inside a microcantilever [35]. The fluid that is continuously delivering the analytes to the cantilever changes the resonance frequency of the cantilever upon binding to the complementary species that are pre-functionalized in the inner microchannel surface, without compromising on the cantilever performance. A transient flow of the particle through the channel results in temporary dips in the frequency depending on mass and location of the particle in the channel. Schematic drawing of the principle of operation of a hollow cantilever and its measurement has been depicted in Fig. 2.3. Sub-femtogram mass resolution is attained by shrinking the wall and fluid layer thickness to the micrometer scale and by packaging the cantilever under high vacuum. Using this setup, weighing of a single biomolecule and nanoparticle in the fluid with a mass resolution of 300 attograms was demonstrated [18]. Despite a paradigm shift in sensing in a fluidic environment, these suspended microchannel cantilevers have to rely on surface functionalization for selectivity, thus limiting their potential.

2.2 Nanomechanical string based sensors

Microstrings are basically miniaturized bridge like doubly clamped mechanical structures under extreme tensile stress (≈>500 MPa). The dynamic behavior of the beam is considered string like because of the extreme pre-tensile stress that has been build up in the beam. The resonating behavior of the string can be approximated to that of a beam with some assumptions and boundary conditions. The equation of motion of a pre-stress beam of length L, width w and height h is given by the modified Euler-Bernoulli beam equation [36].

$$EI\frac{\partial^4 U(x,t)}{\partial x^4} - N\frac{\partial^2 U(x,t)}{\partial x^2} + \rho A\frac{\partial^2 U(x,t)}{\partial t^2} = 0 \tag{2.4}$$

Where $U(x,t)$ is the displacement of the beam as a function of position along the beam and time, E Young's modulus, I the area moment of inertia, N = σA is the tensile force, ρ

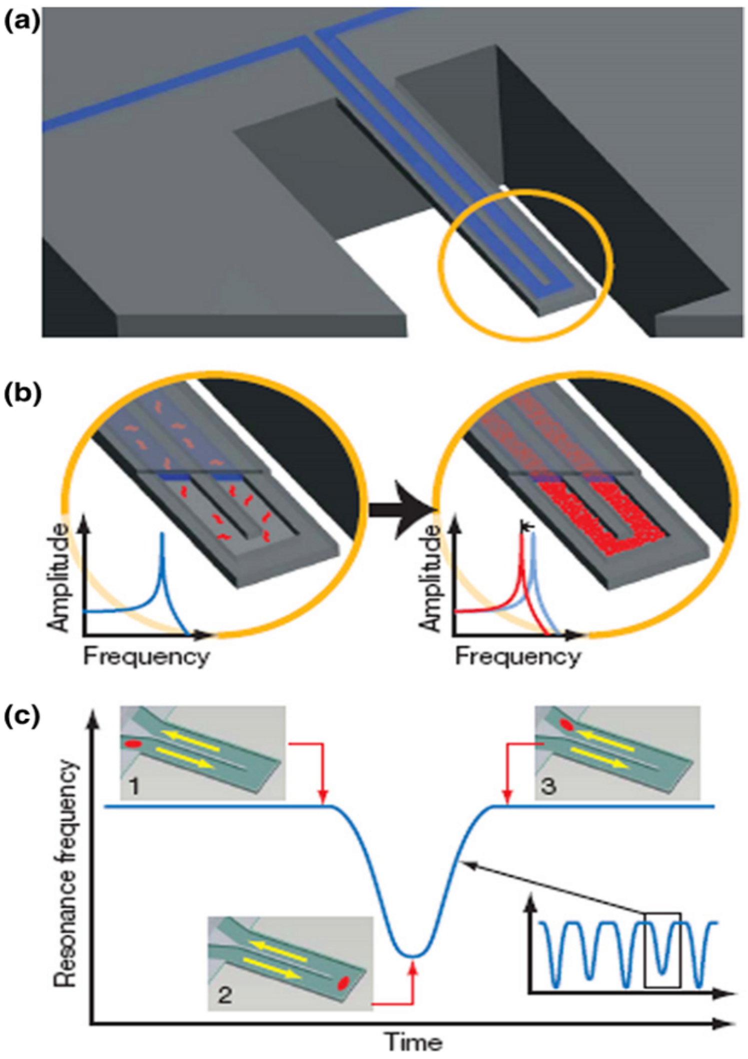

Figure 2.3: Schematic drawing of the principle of operation of a hollow cantilever. (a) A suspended microchannel translates mass changes into changes in resonance frequency. Fluid continuously flows through the channel and delivers biomolecules, cells or synthetic particles.(b) While bound and unbound molecules both increase the mass of the channel, species that bind to the channel wall accumulates inside the device, and, as a result, their number can greatly exceed the number of free molecules in solution. This enables specific detection by way of immobilized receptors. (c) In another measurement mode particles flow through the cantilever without binding to the surface, and the observed signal depends on the position of particles along the channel (insets 1 to 3). The exact mass excess of a particle can be quantified by the peak frequency shift induced at the apex [18]. Reproduced with permission from [18]. Copy right 2007 Nature Publishing Group

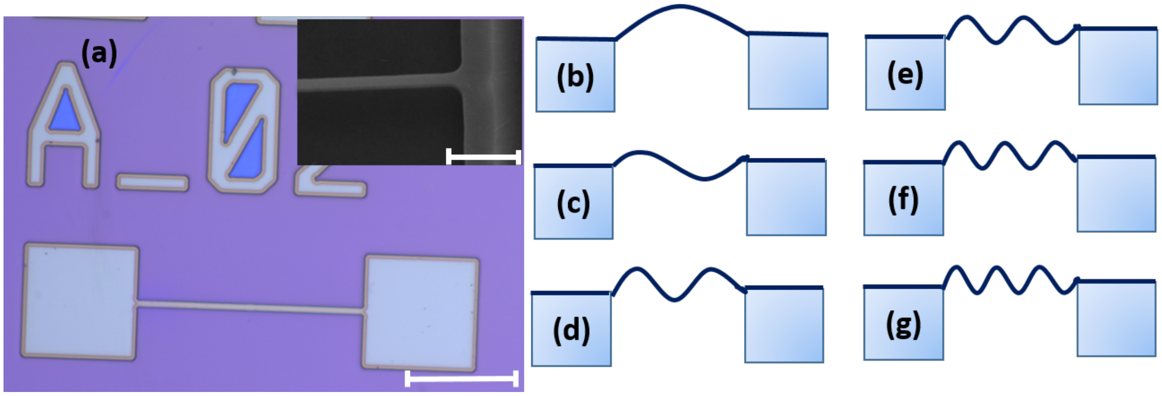

Figure 2.4: (a) Optical image of the silicon nitride string of length 100 μm long. Scale bar is 50 μm. Inset (a) shows a SEM of string at the anchor region. Scale bar 5 μm. (b)-(g) Schematics showing the mode shapes of the first six harmonics of a nanostring.

the mass density and $A =' wh'$ the cross sectional area of the beam. Neglecting rotational inertia and shear deformations for an elastic material, the solution to the above equation can be written as $U(x,t) = \phi(x) \exp -i\omega t$ where ω is the eigen frequency. Inserting this into the equation 2.4, considering the modified boundary conditions for a double pinned beam as $U(0,t) = U(L,t) = 0$, $U''(0,t) = U''(L,t) = 0$ and solving for a double pinned beam, the eigen frequency is written as [36]

$$\omega_n = \frac{(\lambda_n)^2}{2\pi L^2}\sqrt{\frac{EI}{\rho A}}\sqrt{1 + \frac{\sigma A L^2}{(\lambda_n)^2 EI}} \tag{2.5}$$

where $\lambda_n = n\pi$ are solutions to the characteristic equation. For a long and very thin beam $(L/h >> 10)$under sufficiently high tensile stress, $12\sigma L^2 >> (n\pi)^2 E h^2$ the dynamic behavior becomes string like. In this case the above equation becomes

$$\omega_n = \frac{n\pi}{L}\sqrt{\frac{\sigma}{\rho}} \tag{2.6}$$

Assuming the flexural rigidity of the beam is neglected, the dynamic behavior of the string of length l, width w and thickness h with a pre-stress of σ is followed as [37]

$$f_0 = \frac{n}{2L}\sqrt{\frac{\sigma_0}{\rho}} \tag{2.7}$$

Where n is the resonance mode, ρ is the effective mass density of the string.

Nanomechanical strings of mass tens of picograms are incredibly sensitive to added mass. Nanomechanical strings are relatively new and exciting class of gravimetric sensors with minuscule mass, high frequency, exceptional ultra-high quality factors, high tolerance in fabrication, the string like behavior and amenable to easy optical readout mechanisms. The high tensile stress inherent during the fabrication of strings has been demonstrated to be the main reason for exceptionally high-quality factors. Among various fabrication materials, silicon nitride microstrings have been attracting considerable interest due to low material damping leading to high-quality factors, relatively easy fabrication. Various theories have been proposed to discuss the damping mechanisms in thermomechanically driven silicon nitride nanostrings. The principal damping mechanism has been attributed to damping at the anchor points [19]. Biswas et al. have demonstrated an interesting observation that addition of a chemically functionalizable metal overlayer does not affect the quality factor adversely. The reason for this anomalous behavior has been attributed to bulk dissipation due to internal stresses [38].

As evident from the equation 2.7 the dynamics of the string mainly depend on the length and material density of the string and pre-stress. Relatively large displacement amplitude of the strings makes the vibrational frequency measurement easy and accurate. As a typical behavior of the string, the harmonics of the string are integral multiples of fundamental frequency. A scanning electron micrograph and different mode shapes of the first six harmonics of a nanostring are shown in Fig. 2.4. Extremely high-quality factor resonance of 207,000 at room temperature have been demonstrated by Verbridge et al. with nanostrings under high tensile ($\approx$ 1400 MPa) [39]. They have investigated the reasons for high-quality factor and postulated that pre-stress can be considered as a tunable parameter for varying quality factor [40]. Recently, nanobeam based sensors have been used as mass spectrometers detecting single bio-molecules. Nanomechanical mass spectrometers have been demonstrated successfully to calculate the mass of the molecules by building histograms of event probability versus frequency-shift amplitude [41]. Silvan et al. have demonstrated real-time particle mass spectrometry based on resonant microstrings. They have developed a method for fast and quantitative calculation of the position and mass of individual particles placed on a micro or nanostring by measuring the resonant frequency shifts of the first two bending modes. A proof of concept has been demonstrated by placing μm sized beads on the string at much faster measurement time [42]. Nanomechanical string resonators have been used in mass sensing [42], temperature sensing [43], in thermal characterization as an analytical tool [44]and opto-mechanics.

2.3 Chemical selectivity

In order to extend the highly sensitive resonator platform to other applications such as to sense chemicals, physical and biological samples, one has to make the resonators responsive to external stimuli. One way to achieve this is to coat the surface of the resonator with an external stimuli-responsive material making it a bimaterial. The surface coatings can be organic(polymer coatings, SAMs, and immobilized interfaces) or inorganic (metal, metal oxide coatings). The first of its kind Hg vapor detection was demonstrated by Thundat et al. by coating the surface of a microcantilever with gold and exposed it to mercury vapors resulting in a distinguishable frequency change [26]. Metal and metal oxide frameworks have been well explored to study and sense the behavior of various volatile organic vapors [45,46]. To enhance the functionality of resonator based sensing, numerous organic species have been applied as responsive coatings such as SAMs , biomolecules (DNA, specific antibodies [47], polypeptides, nucleotides) [48], lipid layers, homopolymers, block copolymers, plasma polymers, polymer brushes [49–52], polymer/inorganic nanocomposites, hydrogels, and sol-gel layers to detect various physical, chemical and biological stimuli [10]. The bending of the microcantilever is due to the differential stress created on the surface of the microcantilever. The bending of the microcantilever can be maximized by designing the surface stress to occur away from the neutral axis to result in maximum bending. The application of SAMs to one side of the gold-coated microcantilever to induce preferential adsorption has been demonstrated successfully in detecting metal ions, plastic explosives, nerve agents and organic vapors [53–56]. Thiol chemistry has been used to link gold coated microcantilevers to the desired organic molecules by placing the microcantilever in dilute solutions of the desired organic sample for long enough time to create a dense SAM layer. Polymer surface modification is the most commonly used technique in chemical vapor sensing. Sensor surfaces are coated with the desired polymer using various methods such as drop casting, spin coating, spray coating, capillary painting, ink jet printing and in-situ polymerization [14]. Contrasting to SAM functionalization, the major response to polymer coated sensors are the salvation and swelling characteristics of the polymer to chemical vapors. It is observed that the response of polymer coated surfaces is more than SAM-coated surfaces. Localized surface functionalization came to prominence to overcome the problems posed by keeping the entire sensor chip array in solution for long hours. This was achieved by capillary functionalization and ink-jet printing in relatively less time and convenient manner by placing micro drops of solutions on the surface of the sensor at desired locations. Localized surface modification allows functionalization of different sensor surfaces with affinity to different molecular groups paving a way for multifunctional sensor system [57, 58] .

2.3.1 Disadvantages of surface modification

Despite the advances in surface modification procedures and methods, chemically modified sensor surfaces, however, can only give partial selectivity to the molecules due to weak and unspecific nature of intermolecular interactions such as hydrogen bonding. The interference from other vapors results in an unacceptable level of false positives. However, the formation of densely packed surface functionalized layer usually takes long hours posing a threat of non-repeatability, irregularities caused by external impurities and potential damage to the sensor platform. These functionalized surfaces are difficult to be regenerated unless otherwise different approach has been considered. Moreover, the multifunctional array of sensors developed for pattern recognition is not well developed to an extent that they can work in ternary mixtures and more [59]. The recent invention of piezo droppers and associated mechanism is not only cumbersome but expensive. Quantitative analysis based on immobilized chemo-selective interfaces is difficult to the accuracy of trace levels because the response of the sensor depends on many factors such as immobilization layer thickness, the morphology of the film, packing density, coverage coefficient on the sensor surface and the quality of the immobilization. These parameters are not only difficult to control but are observed to add noise to the system. Detailed mechanisms of surface stress and molecular adsorption related effects are still in debate [60].

On the other hand, spectroscopy techniques are very well developed conventional methods based on unique molecular vibrational transitions in the mid-IR region, where many molecules display characteristic vibrational peaks representing the molecular bonds and their configurations. Hence, the mid-IR region is called, ”molecular fingerprint” regime. Generally, spectroscopy involves measuring the intensity of the transmitted light that passes through the sample, governed by Beer Lambert’s law. The decrease in the transmitted signal intensity is the indication of the absorbed energy by the sample. The absorption spectrum is primarily determined by the molecular composition and bond configuration of the sample. Radiated photons are more likely to be absorbed in frequencies that match the natural frequency of the molecular bonds present in the sample. These intensity peaks at the absorbed frequency are highly selective and free from overtones. The spectroscopic signal magnitude of a compound is linear with respect to its concentration, thus providing easy analysis for quantitative measurements. The spectroscopic signal from a mixture of molecules follows superposition principle unless there are intermolecular interactions [61]. Although, Fourier Transform Infrared (FTIR) spectroscopy offers high selectivity, it cannot detect chemical signature from trace amounts of adsorbed chemicals and weak IR absorbing materials such as liquids.

Recently, photothermal spectroscopy techniques using micro/nanomechanical resonators are under vibrant research to combine the extremely high thermal sensitivity of a resonator with the high selectivity of mid-IR spectroscopy, capable of obtaining chemical information from the trace amounts of mass adsorbed on a sensor surface without the complexity of surface modification. In this technique, the adsorbed chemicals on a sensor surface are exposed to mid-IR radiation [11]. During resonant excitation of target molecules using IR radiation, the excited molecules relax by non-radiatve decay mechanisms resulting in heat. This increase in temperature at the sensor surface effects mechanical and thermodynamic properties of the resonator. Rapid growth in MEMS/NEMS resonators realized not only minuscule structures that are extremely sensitive to external stimuli but also highly sensitive detection mechanisms. In this scenario, the resonator is considered as a thermal sensor and various methods are developed to improve the performance of the sensor.

2.4 Basics of photothermal effects

The basis of photothermal effect is a photo-induced change in the thermal state of the sample. Light energy absorbed and not lost by the subsequent emission, results in sample heating. This heating results in temperature change as well as changes in thermodynamic parameters of the sample that are related to temperature. The increased internal energy due to photon absorption is dispersed in two different modes of hydrodynamic relaxation. The temperature change in the sample or surrounding media results in a change in density or change in pressure in case of rapid heating and cooling [62]. There are three important areas to consider for obtaining a quantitative description of the photothermal signal.

1. Description of optical absorption and excited state relaxation process

2. Hydrodynamic relaxation of the sample to achieve thermal equilibrium

3. Signal detection due to change in temperature by monitoring the refractive index of the sample or surrounding media

Table 2.1: Table of different photothermal techniques [62]

Thermodynamic parameter	**Measured property**	**Detection technique**
Temperature	Temperature	Calorimetry
	Infrared emission	Photothermal radiometry
Pressure	Acoustic wave	Photoacoustic spectroscopy
Density	Refractive index	
	Photothermal interferometry	
	Photothermal deflection	Photothermal lens
	Photothermal diffraction	
	Photothermal refraction	
	Surface deformation	Surface deflection

2.4.1 Advantages of Photothermal spectroscopy to conventional methods

The photothermal spectroscopy method has a number of merits compared to the current direct measurement of optical absorption. This is one of the several indirect methods for optical absorption analysis. Indirect methods do not measure the transmission of light used to excite the sample, but rather, measure an effect that optical absorption has on the sample. Photothermal spectroscopy is a direct measure of optical absorption and its effects keeping it away from the scattering and reflection losses interfering with the signals [63]. It is highly sensitive and applicable to different types of material such as gas, liquid, liquid crystal and solid, transparent and opaque. It can be used in vacuum and in the air, and with samples of arbitrary shape. Radiation of any wavelength can be used [64]. They are often nondestructive and non-contact and can be used to probe optical and thermal properties of the sample in very small areas [65]. The dynamic range for photothermal methods is wide and extends over 14 orders of magnitude (from seconds to femtoseconds). The sensitivity of the photothermal effect is attributed to amplification of the signal by high enhancement factor that depends on thermal and optical properties of the sample, power of the light source and on optical geometry. The fundamental limitation of the conventional absorption spectroscopy, shot noise may be practically circumvented because of the superior signal to noise ratio [66]. This technique allows the measurement of thermal properties at the nanoscale with unprecedented accuracy and precision.

2.5 MEMS as thermal sensors

2.5.1 Microcantilever thermal detectors

In Photothermal cantilever deflection spectroscopy (PCDS), the high thermal sensitivity of microcantilever platform with the highly selective mid-IR spectroscopy is capable of obtaining chemical identification from trace amounts of adsorbed molecules on the sensor surface. The current section emphasizes microcantilevers as thermal detectors. Bimaterial cantilevers are extensively investigated as highly sensitive thermal sensors for various applications including calorimetry [67], spectroscopy [68], IR detectors [69–71], scanning thermal imaging probes [72] and as microscale thermal analytical tool [73]. Bimaterial cantilevers have demonstrated their ability as excellent thermal sensors detecting as small as 40 pW for power, 10 fJ for energy and a temperature resolution of 10^{-5} K [74]. The general approach for a bimaterial cantilever has been measuring the static deflection of the cantilever due to thermal stress generated by the mismatch of the thermal expansion coefficients of the constituent materials for a temperature rise. Deflection of a bimaterial microcantilever is calculated considering the heat transfer to and within the cantilever, and mechanical behavior of the cantilever to a temperature rise. The deflection of the bimaterial cantilever for a thermal stress is given by [67]

$$\frac{d^2z}{dx^2} = 6(\alpha_1 - \alpha_2)(\frac{t_1 + t_2}{{t_2}^2 K})[T(x_0) - T] \tag{2.8}$$

where

$$K = 4 + 6(\frac{t_1}{t_2}) + 4(\frac{t_1}{t_2})^2 + \frac{E_1}{E_2}(\frac{t_1}{t_2})^3 + (\frac{E_2}{E_1})(\frac{t_2}{t_1}) \tag{2.9}$$

$z(x)$ is the vertical deflection, $(T(x_0) - T)$is the temperature difference between the cantilever and ambient temperature at a location x along the length of the cantilever, α is the thermal expansion coefficient and E is the Young's modulus [75]. In this section subscript 1 indicates the metal coating material and subscript 2 indicates the substrate material

The temperature distribution in the cantilever can be solved through a heat transfer model based on the following assumptions [76].

1. The temperature gradient is assumed to vary only along the length of the cantilever. Since Biot number, based on half of the cantilever thickness is smaller than 10^{-4}, the temperature distribution along the thickness direction is neglected.

2. The convection coefficient h is assumed to be constant irrespective of the location on the cantilever and temperature.

3. The convective losses are considered for each layer of the cantilever with respect to its differential perimeter element.

4. The cantilever is assumed to be illuminated with a laser beam of the homogeneous intensity distribution.

5. The temperature at the base of the cantilever is assumed to be same as the ambient, T_0

With these assumptions, the one-dimensional energy balance equation for an element of length Δx along the length of the cantilever is

$$\frac{\partial \theta(x,t)}{\partial t} = \frac{A_{cx,1}k_1 + A_{cx,2}k_2}{\rho_1 c_1 A_{cx,1} + \rho_2 c_2 A_{cx,2}} \frac{\partial^2 \theta(x,t)}{\partial^2 x} - \frac{L_p h w}{\rho_1 c_1 A_{cx,1} + \rho_2 c_2 A_{cx,2}} \theta(x,t) + \frac{A I(t)}{\rho_1 c_1 A_{cx,1} + \rho_2 c_2 A_{cx,2}} \tag{2.10}$$

Where A is the spectral absorbance, A_{cx} is the cross section area, c is the specific heat capacity, $L_p = 2(t_1 + t_2 + w)$ is the perimeter of the differential element of the cantilever, h the convection coefficients for cantilever to air , $\theta = T - T_0$, k is the thermal conductivity and ρ is the density [77]. The shape of I(t) is assumed as a square wave with a duty cycle of 5%.

Upon solving the above equation, the deflection of the tip of a bimaterial cantilever in response to a temperature change, ΔT, is given by [67]

$$\Delta z(0) = 3(\alpha_1 - \alpha_2) l^2 (\frac{t_1 + t_2}{{t_2}^2 K})(T - T_0) \tag{2.11}$$

2.5.2 Parameters affecting the performance

Thickness of the metal: The deflection of the bimaterial cantilever for a unit rise in temperature is very much dependent on the relative thickness of metal to the substrate. Lai et al. have showed that for the system of SiNx/Au, the maximum response was obtained for the optimum metal thickness ratio of 0.25 relative to SiNx thickness. They have also demonstrated 50 % improvement in the response by optimizing the thickness ratio of two materials [78]. The thickness of the metal plays an important role in heat transfer to and from the cantilever surface, thus effecting the deflection of the cantilever.

The quality of the metal film such as the deposition method and surface quality also affects the performance but not as significant as the thickness. The general rule of 0.25 relative to the substrate material may not be applicable in all cases, hence one has to optimize the metal thickness for maximum response.

The rise in temperature due to photon absorption: The rise in temperature, when irradiated with a photon, depends on the power of the light absorbed and inversely proportional to heat loss mechanisms available. The rise in temperature is given by

$$\Delta T = \frac{\eta P_0}{G\sqrt{(1+\omega^2\tau^2)}} \tag{2.12}$$

Where η is the absorbance, P_0 is the incident power, G is the thermal conductance, ω are the IR modulation frequency and τ is the thermal time constant [79]. It is observed that the thermal conductance of the materials involved, play a vital role in conductive heat loss and convection losses to the environment. Radiation losses are negligible in cases where the temperature raised due to photon absorption is minimal. In general, the value of thermal conductance of the strucutre is the ratio of thermal conductivity of the individual material multiplied by the area of the cross section to their length. For a better temperature response, enough thermal isolation should be provided by choosing materials of low thermal conductivity and better design parameters [69]. The other way to increase the rise in temperature is to provide maximum absorbed power. The substrate materials such as SiO_2, Si_3N_4 show a better response than Si due to less thermal conductance. The power absorbed depends on power incident, relative irradiance area and absorption coefficient of the material at that wavelength of photon irradiation. The intrinsic photon absorption can be increased by a thin coating of Ti or some high photon absorbing material of choice without losing the performance. The other way to increase the photon absorption is by resonant cavity effect wherein the photon travels multiple times due resonance cavities and thus increases the effective photon absorption. It has to be noted that, to keep the detector at the best place in a cavity, heat losses due to air in the gap should be considered. Sometimes these heat losses due to air convection can be the principal heat loss mechanism than the thermal conductance of the material [71, 80].

IR modulation frequency: As noted from the previous section, the rise in temperature also depends on IR modulation frequency. At higher modulation frequencies, the detector response begins to decrease. Hence, the modulation frequency has to be optimized to give enough time for the detector to come to its original position in the absence of photon radiation. The best index of optimization is that $\omega\tau$ should be small and less than unity [81].

Thermal stress: The deflection of the cantilever to a temperature rise is because of the differential thermal stress created due to mismatch of thermal expansion coefficient of the constituents to a rise in temperature. The thermal stress created is given as $\sigma = E\Delta\alpha\Delta T$. The response of cantilever to a unit temperature rise can be maximized by choosing appropriate materials having a large difference in thermal expansion coefficient. It has been demonstrated that aluminum and polymer coating results in higher deflection than the gold coating for the same temperature rise due to the higher difference in thermal expansion coefficient [51].

Noise mechanism: In general, noise in micromechanical devices can be related to intrinsic noise and external noise such as heat exchange, adsorption-desorption, Johnson noise and noise in the read-out electronics.The dominant noise mechanisms available for a mechanical resonator are thermo-mechanical noise and background fluctuation noise (effective only in heat loss via radiation) [71]. Thermomechanical noise (TM noise) is due to the continuous energy exchange between energy accumulated in the device and the thermal energy of the environment. It has been recognized that the mechanical energy dissipation is mainly due to viscoelastic losses in the cantilever. At lower frequencies, the tip displacement due to thermo-mechanical noise is given as

$$< \delta z_{TM}^2 >^{1/2} = \sqrt{\frac{4k_B BT}{Qk\omega_0}} \tag{2.13}$$

where k_B is the Boltzmann constant, T is the absolute temperature, B is the measurement bandwidth, Q is the quality factor, k is the spring constant and ω_0 is the angular frequency of the cantilever [82]. Hence, higher spring constant cantilevers operated in vacuum conditions will have lower TM noise. The performance of all thermal detectors is limited by temperature fluctuation noise (TF noise) due to the continuous exchange of heat at the microscopic level. The spontaneous fluctuations are displacement of the cantilever caused by temperature fluctuation is given by [83]

$$< \delta z_{TF}^2 >^{1/2} = \frac{\Delta z T\sqrt{4k_B BG_T}}{P_0\eta} \tag{2.14}$$

From the above equation, it is to be noted that the main design parameter affecting the noise is the thermal conductance. Decreasing the thermal conductance to the best possible scenario may result in a slower response time of the sensor, hence one should optimize the thermal conductance as per the application requirement [83].

2.5.3 Microstrings as thermal detectors

Other than mass sensing, nanomechanical strings are used as excellent temperature sensors [43] and in thermal characterization as an analytical tool [44]. Resonating temperature sensors have been used in the past to achieve a temperature resolution of $\approx 10^{-3}$K. The underlying concept behind these sensors is the extreme sensitivity of resonating dynamics of the devices to temperature. The built-in tensile stress in the string changes as a result of thermal stress generated upon temperature change. The thermal stress could be because of mismatch in the expansion coefficients of the string material and the frame or could be due to the temperature sensitivity of the string material itself. When the string is subjected to heating, it experiences a thermal stress in accordance with coefficient of thermal expansion due to temperature rise given by

$$\sigma_T = E(\alpha_B - \alpha_S)\Delta T \tag{2.15}$$

Where σ_T is the thermal stress, E is the Young's modulus of the string material, α_B is the thermal expansion coefficient of the beam, α_S is the thermal expansion coefficient of support. The shift in frequency due to heating is dependent on whether the heat is localized or uniformly distributed. In the case of localized heating, where the ends of the string are maintained at room temperature and only the center of the string is subjected to heating, heating will lead to a reduction in pre-stress of the string due to the thermal stress. This will in turn decrease the resonance frequency of the string to [84]

$$f = \frac{n}{2L}\sqrt{\frac{\sigma}{\rho}} \tag{2.16}$$

Where $\sigma = \sigma_0 - \sigma_T$ for a temperature rise of ΔT. The temperature sensitivity of the string, when subjected to localized heating at the center of the string, can be deduced by differentiating the frequency with temperature [43]

$$S = \frac{\partial f_n}{\partial T} = \frac{-nE\alpha}{4L\sqrt{\rho(\sigma_0 - E\alpha\Delta T)}} \tag{2.17}$$

From the above expression, it is evident that the temperature sensitivity of a string can be increased by increasing the frequency mode number (n), Young's modulus of the string material and its thermal expansion coefficient and by decreasing the length of the string, pre-stress and mass density. The temperature resolution by a string is inverse of its temperature sensitivity times frequency resolution. The ultimate limits of temperature measurements are limited by frequency resolution hence frequency stability has to be considered. As the noise in dynamic measurements of strings are mentioned as allan deviation (relative frequency shift vs time), relative frequency ($\Delta f/f$) was considered to be the dependent parameter rather than simple frequency shift (Δf). Tom et al. have demonstrated the temperature sensitivity of the strings by varying the dimensions, by fabricating metallic (Ni and Al)strings and by changing the pre-stress conditions. From their observations, metallic strings demonstrate better temperature response than silicon nitride strings but with lower dynamic range and reproducibility. Micro strings made of aluminum were demonstrated have better sensitivity and temperature resolution. Though metallic strings demonstrate better temperature response their frequency resolution is very poor due to instability in frequency measurement [43]. The frequency resolution depends on the quality factor of the string, methods used to actuate and read out. The quality factor of the metallic strings has been found to be way lower than the silicon nitride strings, thus limiting the ultimate temperature resolution. Metallic strings, further possess anelastic behavior causing hysteresis in the measurements, very sensitive to power fluctuations in the readout laser causing irreproducible results, small tolerance in fabrication and not suitable for simultaneous gravimetric sensing and thermal sensing [84]. Hence, we have focused our further studies on micro strings made of silicon nitride with ultra-high quality factors enabling mass resolution up to few $\approx$ ag. These strings are fabricated by regular lithography processes and also using EBL to achieve exceptional mass resolutions and effort was made to obtain molecular signature by considering the strings as thermal sensors.

2.6 Photothermal spectroscopy using MEMS

Detection, speciation, and quantification of the extremely small concentration of analytes with very high selectivity and sensitivity have immediate applications in numerous fields of sensing. Though microfabricated sensors are exceptionally good as gravimetric sensors up to a mass resolution of single proton level, they lack intrinsic selectivity to a specific analyte, hence have to heavily rely on immobilized chemo-selective interfaces. Disadvantages posed by immobilized surfaces and advances in using MEMS as thermal sensors paved a way for an alternative route for selectivity using photothermal techniques.

The use of bimorph structures as temperature sensors can be dated back to 1735 where they were used in clock escapement to account for changes in temperature [85]. The use of micromachined bimorph structures started in 1980's and since then they haven been extensively investigated as sensitive thermal platforms. The basic principle behind these structures is the differential thermal stress created due to the mismatch in thermal expansion coefficient of constituent materials for a temperature rise, resulting in a static deflection [86]. The high sensitivity of bimaterial microcantilevers for temperature was first demonstrated by Gimzewski et al. in a micromechanical calorimetric application to study the chemical reaction of $H_2 + O_2$ to form H_2O over a Pt-coated microcantilever. They have estimated sensitivity limit of picojoule (pJ) and a temperature resolution of 10^{-5}K [87]. Later Barnes et al. have demonstrated a femtojoule calorimeter with a sensitivity of 100 pW and an energy resolution of 150 fJ [67]. On similar notes, Barnes et al. have demonstrated the first photothermal spectroscopy application to detect dye molecules present on cantilever surface [68]. Significant work was done by Majumdar's group to optimize and understand the devic mechanics to reach the sensitivity limits of 40 pW and 10 fJ [78]. Since then extensive research was carried out to optimize the performance and explore microcantilever platform for thermal sensing applications. Wig et al. have demonstrated the detection of Bacillus anthracis and Bacillus cereus using photothermal cantilever deflection spectroscopy (PCDS) [88]. Later, Krause et al. have demonstrated detection of trace amounts (ng) of explosives such as RDX using PCDS [17]. Guangming Li et al. have demonstrated the application of photothermal spectroscopy using a multilayer cantilever to detect DMMP [89]. Thundat and Datskos group from ORNL made significant contributions in identification and detection of trace amounts of various surface adsorbed analytes such as biological warfare agents [90], biological species [91,92], nerve gas stimulants, organic and polymer adsorbates [93] using microcalorimetric spectroscopy techniques [94]. Datskos et al. have investigated arrays of bimaterial cantilevers for thermal imaging applications demonstrating an noise equivalnet temperaure detection (NETD) of 5 mK [70].

Van Neste et al. have used photoacoustic methods to detect surface adsorbed chemicals on Quartz tuning forks (QTFs) sensor surface [95]. They have demonstrated a novel method for standoff detection of explosive residues using QTFs [96].

Seonghwan Kim et al. demonstrated successful speciation and quantification of picogram levels of ternary mixtures of similar explosives trinitrotoulene (TNT), Cyclotrimethylenetrinitramine (RDX) and pentaerythritol tetranitrate (PETN) with an order of magnitude higher limit of recognition (<32:1). Limit of detection has been improved by employing high power IR laser, optimizing the device mechanics, fabricating new designs of devices and by increasing the IR absorption [11]. Dongkyu et al. have fabricated nanoporous cantilevers made of an anodized aluminum oxide (AAO), titanium oxide and porous silicon to increase the thermal sensitivity by reducing the Young's modulus and increase surface area for more molecular adsorption [97]. They have demonstrated detection of tens of picograms (ppb level) of explosive molecules and sub ng (ppm level) DMMP molecules, using thermally sensitive nanoporous TiO_2 cantilevers [98]. Minhyuk et al. have studied the degradation of PMMA films on a microcantilever using PCDS techniques [99]. Bagheri et al. have investigated the detection of real life physisorbed complex hydrocarbons such as naphta using PCDS [100]. Efforts were made to discriminate DNA strands using an electrical readout piezoelectric cantilever made of PZT [101].

Though bimaterial cantilevers are demonstrated as excellent thermal sensors, they are not well suited for bio-applications because of the damping effects due to the presence of liquid around. So far, the chemical signature from tens of pg of adsorbed molecules on sensor surface have been detected using PCDS technique but in the presence of liquid one still have to rely on chemo-selective interfaces. Real-time bio applications demand high sensitivity and high selectivity in the presence of liquid. Manalis group have come up with a novel and innovative design to counter the damping effects, by placing a microchannel embedded inside a microcantilever [35]. These SMRs solve a decade-old problem of weighing analytes with mass resolutions up to single cells, virus and nanoparticles in solution up to a resolution of ag level [18]. In the scenario of using these devices for biological sensing, one has to heavily rely on chemo-selective surface immobilization procedures adding more complexity and resulting erroneous results. Recently, Faheem khan et al. have used similar kind of devices to identify 1 wt% of ampicilin sodium salt in water by employing photothermal spectroscopy techniques. They have further demonstrated that they can identify chemical signature of up to 5 wt% of ethanol in ethanol-water binary mixture [103]. In this thesis, we aim to optimize the performance of BMC as thermal sensors and demonstrated an order of magnitude improvement in the spectroscopic limit of detection. BMCs are also explored as micromechanical calorimeters to find thermal properties of liquids in the channel.

The real world applications of sensors pose challenges in detection, speciation and quantification of extremely small concentrations analytes with high sensitivity and selectivity.

Though high sensitivity has been achieved by rapid developments in miniaturization, obtaining selectivity is still a challenge for such small concentrations. Hence, other highly sensitive resonator platforms have been investigated such as nanomechanical cantilevers, bridges, and nanomechanical strings. Nanomechanical strings with minuscule mass, exceptionally high-quality factors and string like behavior due to inherent pre-stress is considered as a promising platform [19]. Among all of them, silicon nitride nanomechanical strings are relatively new and exciting class of gravimetric sensors with mass resolution up to ag [38]. The thermal stress created upon for a temperature rise results in frequency detuning of the string. Tom Larsen et al. have investigated strings as ultra sensitive temperature sensors as the dynamic characteristics such as frequency and quality factor are extremely sensitive to external temperature. They have fabricated strings of various materials and estimated a temperature resolution of $8\mu K$ using a short aluminum string [43]. The concept of nanomechanical mass spectrometry thrust the interest in adding selectivity factor to the highly sensitive string platform. Recently Anja Boisen group made significant efforts to obtain the chemical identity from the trace amounts present on the string surface. Tom Larsen et al. have investigated the photothermal analysis of individual nanoparticulate samples of different colored polystyrene beads to demonstrate the fact that different color samples induce different frequency shifts due to different photon absorption. In this case, mictrostrings are not only acting as sensitive thermal platforms but also as efficient sample collectors [104]. Shoko Yamada et al. have demonstrated the detection of tens of picograms of analytes and estimated to obtain chemical information from up to 45 fg [105]. We, in collaboration with John Davis group, experimentally detected molecular signature from extremely small amount such as 44 fg of RDX sample deposited on nanomechanical string [102]. This is the first ever reported detection of chemical information from such extremely small mass. We aim to go down the limits to single particle/molecular level by employing ultra-miniaturized nanomechanical strings fabricated by EBL and by employing high power IR laser. On the other hand, these string platforms are also explored as excellent thermoanalytical tools. Sanjukta Bose et al. have demonstrated to identify the glass transition temperature from ng amount of polymer samples [44] . Silvan Schmid et al. have investigated photothermal probing of single plasmonic gold nanostructures with heating maps up to a resolution of 350 nm [106]. Fig. 2.5 (a) shows the typical measurement schematic required for PCDS experiment. Fig. 2.5 (b) and (c) depicts the photothermal spectroscopy of trace quantities of analytes on the resonator surface namely nanomechanical string and BMC. Note that the frequency response (dynamic parameter) has been used as depending parameter in case of nanomechanical string resonator (b) whereas static deflection of BMC has been used as the dependent parameter for hollow channel cantilever.

2.7 Photo effects on functional nanostructures

The underlying concept behind high sensitivity of MEMS/NEMS structures is the extremely small mass, that makes them highly susceptible to external stimuli. The two important attributes namely, mass responsivity and frequency stability are necessary for observing a minute adsorbate induced change. The rapid progress in miniaturization results in devices with a mass of the order of fg, progressing towards GHz frequency devices. NEMS resonators have unprecedented mass sensitivities and photothermal techniques on MEMS/NEMS can address selectivity issues to some extent. As discussed before photothermal techniques rely on thermal sensitivity of the device. So far the studies have been focused on optical detection of nanomechanical motion but in reality this can be a bottleneck in miniaturization and for on-field applications. Many researchers have investigated other detection mechanisms to read minute displacements. On the other hand, recent observations on some highly temperature sensitive materials pave a way for unprecedented detectivity in uncooled thermal imaging by changing the functional property with respect to temperature. One of the classical examples of this category is pyroelectric materials in which polarization is dependent on the temperature gradient. We were interested in combining the extreme mass sensitivity of the resonator and high thermal sensitivity of the material in one device by fabricating a micromechanical resonator made of pyroelectric material. To explore in a broad context, we choose a functional material that has many functional properties at room temperature such as BFO. As BFO is not a fabrication friendly material we would like to pursue chemical synthesis methods to make a suspended BFO nanostructure.

One-dimensional nanostructures of BFO were prepared using the sol-gel synthesis of BFO constituents. Suspended BFO nanowires have been made by electrospinning BFO+ PVP polymer solution at optimized parameters for very less time (1 min) on substrates with Pt electrodes. These substrates were later annealed at an optimized heating program to get single suspended BFO nanowire between the electrodes. The electrodes are then connected to an oscilloscope to observe any real time changes. Suspended single BFO nanowire has been subjected to periodic IR pulses and the resulting changes have been monitored in Oscilloscope. There were no significant changes observed during the radiation of IR to BFO nanowires. Though we observed a small change in the impedance of BFO nanowire with and without IR radiation, the results were not repeatable with high confidence. The main reasons for this behavior might be due to the poor quality of BFO nanowire formed (too many surface defects resulting in leakage currents), lack of proper instrumentation to observe the electrical changes and insignificant influence of IR on functional properties of the nanowire. When irradiated the same set up under visible light we observe sharp changes in Oscilloscope signals. We further explored the behavior of BFO nanostructures under visible light and observed that BFO has significant visible light absorption and shows semiconducting behavior. In addition to its magnetoelectric applications, BFO has recently attracted considerable attention in optoelectronic applications because of its small band gap (2.5 eV) [107,108]. In spite of having excellent multiferroic properties, BFO has not been used in many applications in mainstream devices due to its inability to obtain single phase stoichiometric BFO and presence of leakage currents because of defects [109]. Moreover, the multiferroic and electrical properties are extremely sensitive to defects such as secondary phases, vacancies, and interstitials [109–111]. Many unusual and exciting photo properties of BFO thin films such as light-induced size changes, abnormal photovoltaic effect, persistent photoconductivity, and switchable diode effects have been explained as being a result of the presence of surface defects especially oxygen vacancies [112, 113]. We attribute this anomalous visible light behavior of BFO nanostructures to the excessive surface states present in the material.The high surface area to volume ratio in BFO nanostructures enhances the surface defects, which influence the optoelectronic properties of these structures. The properties of these surface defects may be completely different in nanostructures from those in bulk, and thus offer further opportunities for the development of applications, such as sensing, photoelectronics, and visible light photocatalysis. The effect of surface states/defects on optoelectronic properties of BFO nanostructures has been explained in detail later in chapter 7 of this thesis. After a thorough understanding of the role of surface states on its optical behavior [114, 115], Prashanthi et al. from our group pursued the detection of adsorbed molecules on the surface of a BFO nanowire by considering the electrical resonance approach. The temperature induced carrier population and depopulation of surface states are monitored by the resonance response of dissipation of the electrical resonator [116]. The dissipation with respect to IR wavenumber resembles that of FTIR spectrum. In order to take the advantage of anomalous photo properties of BFO nanostructures, we made BFO nanotubes using sol-gel template synthesis method. These nanotubes show much higher photocatalytic activity in degrading methylene blue in water under visible light compared to BFO nanoparticles. The details of photocatalytic activity of BFO nanotubes is presented later in this thesis.

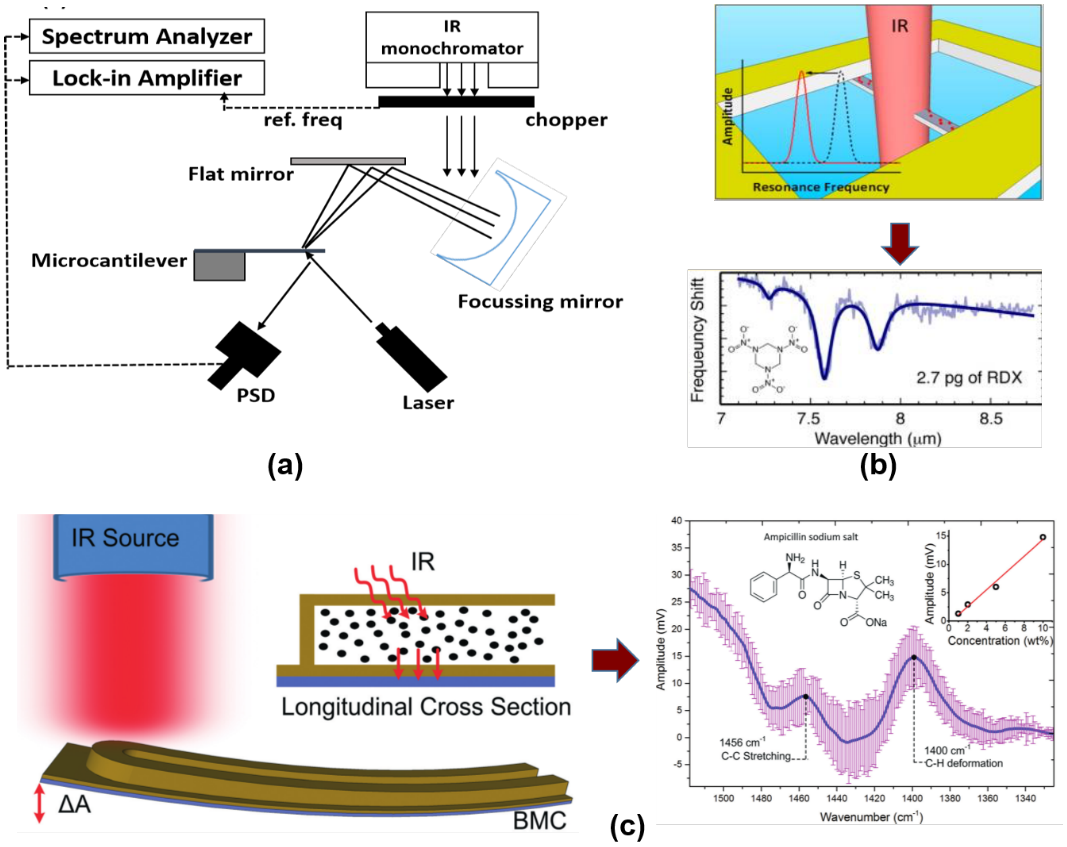

Figure 2.5: (a) Schematic drawing of the PCDS set up [17]. (b)Photothermal spectroscopy of trace quantities (2.7 pg) of explosive material RDX, using the detuning of the frequency of the string upon radiation to IR. The bottom images depict the spectroscopy of RDX [102]. (c) The nanomechanical IR spectrum of 10 wt% amplicillin sodium salt obtained using BMC. The inset shows the linear relationship as a function of ampicillin concentration [103]. Reproduced with permission from [17]. Copy right 2008 Journal of Applied Physics. Reproduced with permission from [103]. Copy right 2014 Lab on a Chip.

Chapter 3

Thermomechanical response of hollow bimaterial microchannel cantilevers

3.1 Overview

In this chapter, we report the dynamic thermomechanical response of a bimaterial microchannel cantilever (BMC) subjected to periodic heating by IR radiation. Detailed theoretical and experimental study was performed considering BMC as a thermal sensor. Experiments were conducted to find out the thermal sensitivity and power sensitivity of various designs of the BMC to optimize various parameters affecting the performance of BMC. We report a minimum measurement of 60 μW of power, the energy resolution of $\approx$ 240 nJ and temperature resolution of 4 mK using the BMC. The best design of the BMC is chosen to demonstrate a spectroscopy application to detect a minimum of 1.15 ng ethanol in the ethanol-water binary mixture. The purpose of this chapter is to extend the applications of the novel SMRs in bio-sensing to add molecular selectivity along with the ultra- sensitive mass resolution.

3.2 Introduction

Recently, there has been a growing interest in the community of nanomechanical sensing to address selectivity problems using highly optical selective photothermal spectroscopy techniques [102] [92]. Spectroscopy techniques are based on unique molecular vibrational transitions in the mid-IR "molecular fingerprint" regime, where many molecules display characteristic peaks free from overtone, thus highly selective. Bimaterial cantilevers are extensively investigated as excellent thermal sensors for various applications including calorimetry [67], IR detectors [69–71, 117], scanning thermal imaging probes [72] and as microscale thermal analytical tool [73]. Though these microcantilevers and PCDS methods are highly successful in detection of analytes in gaseous environments but have received less attention in the detection of biomolecules in the presence of fluid. This is because of the damping and viscous drag effects arising from the surrounding fluid when operated in the fluid environment, thus affecting the frequency resolution and mass sensitivity [118]. Recently, few attempts have been made to weigh particles in the presence of solution by designing an innovative resonator platform in which the fluid has been confined inside the resonator while leaving the exterior in the gaseous environment or vacuum [35, 119]. These microchannel cantilevers have been demonstrated to measure the mass of single cells, virus, and nanoparticles in solution [18], up to a mass resolution of attogram (10^{-21} kg) level [120]. The effective use of microchannel cantilevers in the detection of biomolecules heavily depends on developing chemo-selective surface immobilization interfaces inside the microchannel using functionalization protocols [121]. In reality the functionalization protocols are not only cumbersome and add complexity but also, in most instances pose a threat to damage the device [11]. Few attempts have been made in the past to characterize particles in a liquid using microcantilevers by fabricating an innovative design of cantilevers that have microchannel embedded in them [18]. The current state of the art in microchannel cantilevers can weigh single cells, virus and nanoparticles in solution up to a resolution of $\approx$ ag level [122, 123]. In a similar way, photothermal nanomechanical IR spectroscopy of 5 wt% of ampicillin in solution has been demonstrated using SMRs [103]. Photothermal techniques study the photo-induced change in the thermal state of the material, hence the resonator under study should have a good thermal sensitivity to respond to small temperature changes. In order to further extend the applications of this microchannel cantilevers as a thermal sensor, it is extremely important to understand the thermomechanical behavior of the channel embedded microcantilevers when subjected to periodic IR radiation. To the best of our knowledge, there are no reports found mentioning the thermomechanical characterization of SMRs. Other than mass sensing these devices are also used in liquid spectroscopy [103], viscosity and density measurements [124].

In this chapter, we measure the dynamic response of two different BMC designs to periodic heating by IR radiation and also measure their response to external heating. The detailed experimental analysis is presented to find out the minimum detectable photon radiation and minimum temperature that can be measured using this novel BMC design. This chapter presents methods for optimizing the sensor performance and explores the limits of sensor resolution based on fundamental noise calculations and figures of merit. Optimization of parameters has been implemented to demonstrate a PCDS spectroscopy application to in order to find out the minimum ethanol concentration that can be detected in ethanol-water binary mixtures.

3.3 Experiments

3.3.1 Materials and Methods

Microchannel embedded microcantilevers are made of low-pressure chemical vapor deposition (LPCVD) silicon rich nitride (SRN) by employing bulk micromachining techniques using polysilicon as a sacrificial material. Two different BMC design variations have been investigated to determine the best performing cantilever design and parameters. The design parameters and dimensions of the BMC are presented in table 3.2 The fundamental difference between the two designs is the microchannel dimensions and the channel volume. Complete fabrication details of the device and set up to load the liquid sample can be found elsewhere [125]. The SRN microchannel cantilever is converted to a BMC by depositing an optimized thickness of metal using a thermal evaporator (Cressington, Ted Pella, Inc). A quantum cascade laser (QCL) in the mid-IR range (6 to 13 µm)(Daylight Solutions,MIRCat) operating at 100 kHz repetition rate with 5% duty cycle was electrically burst at an optimized count using a function generator (DS345 Stanford Research (SR) Systems, USA) and directed to the BMC. The static deflection of the BMC was measured using a lock-in amplifier (SR 850, USA). Deflection amplitude of the BMC to external temperature variation was measured by a data acquisition system (NI DAQ 2120) using a temperature controller (Global lab PX9). The noise spectrum and resonance frequencies of the BMC were measured with a spectrum analyzer (SR 760, USA).

When the BMC is radiated with IR, the constituents of BMC absorbs radiated IR power depending on its IR spectral characteristics and the non-radiative decay of photons results in heating. The heat produced due to photothermal effect causes in an increase in temperature at the location of IR radiation [68]. This heat flows down the BMC to the anchor part of the BMC, which is assumed to be a perfect heat sink. We assume that the temperature varies only along the length of the BMC because the thickness of the BMC is much smaller than the thermal diffusion length [126]. Radiative heat loss

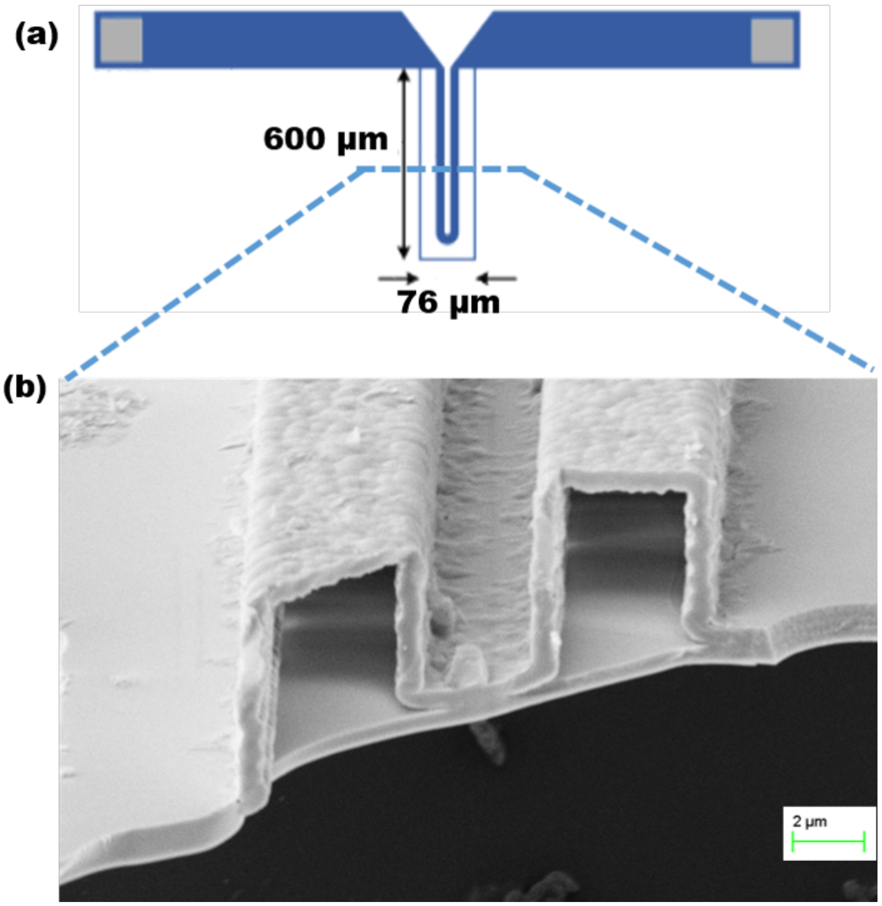

Figure 3.1: (a) Schematic showing the top view of the BMC. Dimensions labeled are for chip A (b) SEM micrograph of cross-sectional view of the BMC at the anchor in a view looking from the tip of the cantilever.

from the BMC is small compared to conduction and convection, as the temperature rise due to IR absorption is small [75]. The temperature rise results in static deflection of the cantilever because of thermal stress developed due to thermal expansion coefficient mismatch of SRN and metal layer for a temperature gradient. The bending of BMC is monitored using laser deflection method. In order to provide periodic IR pulses, we have modulated 100 kHz IR laser pulse with an optimized modulation frequency. The selection of the modulation frequency depends on three factors: 60 Hz electrical noise, 1/f Johnson noise, and the beam modulation attenuation [74].

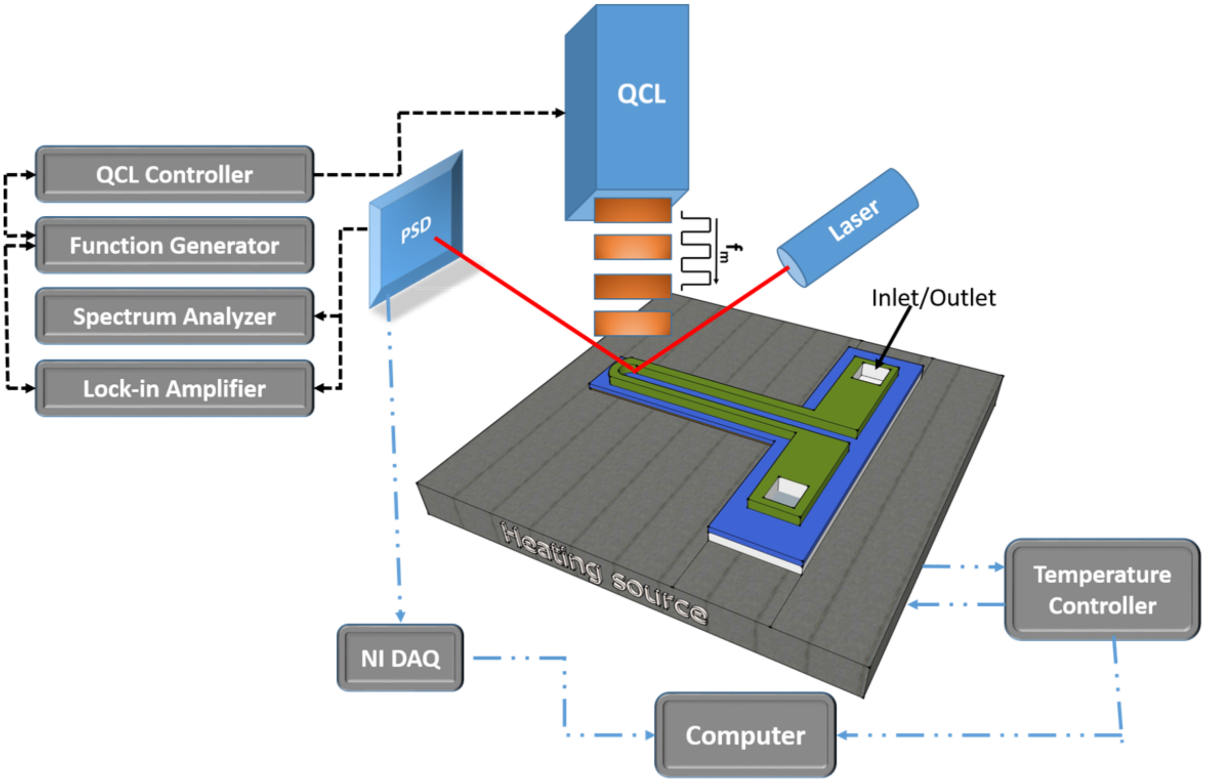

Figure 3.2: Schematic illustration of experimental setup for power sensitivity (connections in black) and thermomechanical sensitivity (connections in blue).

3.3.2 Experimental set up for measuring thermomechanical sensitivity

The top view of the BMC in chip A is shown in Fig. 3.1(a). As depicted by the micrograph of Fig. 3.1 (b), the cross-section of the BMC consists of a microchannel fabricated on the top of a microcantilever. The thermomechanical sensitivity of the BMC with respect to external temperature is measured using Nanomechanical thermal analysis (NTA) set up (connections shown in blue dotted lines) as shown in Fig. 3.2. The deflection of the BMC is measured by monitoring the position of a laser beam (635 nm) reflected off of the BMC surface onto a position-sensing detector (PSD)(SPC-PSD from SiTeck S2-0171). It is to be noted that the laser is reflected from SRN surface as gold is deposited at the back of the cantilever. The BMC is mounted on a ceramic thermal chuck that can be heated through a peltier element beneath the chuck. A K-type thermocouple is attached to the chuck near to BMC to measure the real-time temperature of the chuck. The chuck is heated from 30 ^{o}C to 50 ^{o}C at a heating rate of 2 ^{o}C/min and let it convectively cool from 50 ^{o}C to 30 ^{o}C at a cooling rate of 1.3 ^{o}C/min using a temperature PID controller for multiple cycles. The PSD signal is continuously monitored using an NI DAQ system. Electrical signals from PSD are calibrated to real-time cantilever deflection (nm) using a standard plane bimaterial cantilever (without a microchannel) deflected under uniform heating using a laser Doppler vibrometer (LDV). The thermal cycles of the entire chuck follow a temperature program that is in turn controlled by a temperature controller (GTLC PX9). The normalized deflection signals from the PSD are fed to NI DAQ system that can be recorded using an NI labview program that can in turn synchronize with temperature measurements from the temperature controller.

3.3.3 Experimental set up for measuring power sensitivity

The BMC was placed in a cantilever holder and an experimental arrangement is made to radiate the BMC with a mid-IR QCL as shown in Fig. 3.2 (connections shown in black dotted lines). The deflection amplitude signals from the PSD are diverted to a lock-in amplifier, locked at a frequency of 40 Hz. The QCL was modulated using a function generator that is in synchronization with lock-in amplifier to radiate BMC with periodic IR illumination. The peak-peak power output from the QCL operating at a particular wavenumber can be changed by providing different drive currents to the QCL. Thus, the BMC has been subjected to varying incident IR power and the deflections are monitored using a lock-in amplifier. The QCL is operating at a repetition rate of 100 kHz at a duty cycle of 5% and can provide a maximum of 380 mW peak-peak power at 1270 cm^{-1}. It is to be noted that peak power from the QCL varies with wavenumber. Similar experimental setup has been used for spectroscopy studies along with BMC holder that has liquid loading arrangement.

3.4 Theory of BMC

The bending of BMC is due to the thermal stress created by the thermal expansion mismatch of the layers induced by temperature increase. In this section, the hollow cantilever bending is calculated considering the heat transfer to and within the cantilever, and mechanical behavior of the cantilever. The temperature distribution in the cantilever can be solved through a heat transfer model based on the following assumptions.

1. The temperature gradient is assumed to vary only along the length of the cantilever. Since Biot number, based on half of the cantilever thickness is smaller than 10^{-4}, the temperature distribution along the thickness direction is neglected.

2. The convection coefficient h is assumed to be constant irrespective of the location on the cantilever and temperature.

3. The convective losses are considered for each layer of the cantilever with respect to its differential perimeter element. As ethanol inside the cantilever is receiving heat convectively from SRN walls of the cantilever, a positive energy balance is used.

4. The cantilever is assumed to be illuminated with a laser beam of the homogeneous intensity distribution.

5. The temperature at the base of the cantilever is assumed to be same as the ambient, T_0

With these assumptions we have modified the one dimensional energy balance equation in equation 2.10 for a differential element as per our cantilever geometry. We have considered the liquid in the BMC as a third layer participating in the heat transfer. In this section subscript 1 indicates the metal coating material, subscript 2 indicates the substrate material (SRN) and subscript 3 indicates the material inside the channel. We have considered the heat conduction through the walls of the channel made of SRN, through the liquid inside the channel and the gold layer beneath the cantilever. The convection losses and heat generation due to IR absorption were taken into consideration. The modified energy balance equation for a differential element along the cantilever length is as follows.

$$
\begin{aligned}
\frac{\partial\theta(x,t)}{\partial t} = {} & \frac{A_{cx,1}k_1 + A_{cx,2}k_2 + A_{cx,3}k_3}{\rho_1 c_1 A_{cx,1} + \rho_2 c_2 A_{cx,2} + \rho_3 c_3 A_{cx,3}} \frac{\partial^2\theta(x,t)}{\partial x^2} \\
& - \frac{(L_p h - L_p{}^* h^*)w}{\rho_1 c_1 A_{cx,1} + \rho_2 c_2 A_{cx,2} + \rho_3 c_3 A_{cx,3}} \theta(x,t) \\
& + \frac{AI(t)}{\rho_1 c_1 A_{cx,1} + \rho_2 c_2 A_{cx,2} + \rho_3 c_3 A_{cx,3}}
\end{aligned}
\tag{3.1}
$$

Where A is the spectral absorbance, A_{cx} is the cross section area, c is the specific heat capacity, $L_p = 2(t_1 + t_2 + w)$ is the perimeter of the differential element of the cantilever for each layer and L_p^* is the contact boundary of ethanol and SRN wall of the cantilever, $h = 1200W/m^2K$ and $h^* = 2300W/m^2K$ are the convection coefficients for SRN to air and SRN to ethanol, $\theta = T - T_0$, k is the thermal conductivity and ρ is the density. Thermal conductivity (k_3), specific heat (c_3) and density (ρ_3) of lab grade ethanol are considered as 0.171 W/m.K, 2460 J/Kg.K and 790 Kg/m^3. The material properties of the microcantilever constituents are considered from B. Kown et al [77] as shown in table 3.1. The boundary conditions are θ=0 at x=0 and $\frac{\partial\theta}{\partial x}$ =0 at x=L . The IR source illuminating the cantilever is a QCL operated at maximum current to obtain a power of 225 mW peak to peak at 1053 cm^{-1}. The beam diameter of the laser spot is ≈ 2.5 mm with a Gaussian distribution in the radial direction. The QCL is a pulsed laser of the shape of I(t) as a square wave with a duty cycle of 5%. The average output power is the product of duty cycle and peak power. The incident IR flux is calculated as P_{inc}= 2 $P_{avg}/\pi W^2$ where W is the spot diameter. The incident IR flux for our case at 1053 cm^{-1} is calculated to be 1.8 nW/μm^2.

Table 3.1: Details of material properties [77, 127]

Material	ρ(kg m^{-3})	E (GPa)	k (Wm^{-1} K^{-1})	α(10^{-6} k^{-1})	c(J kg^{-1} K^{-1}
Silicon	2329	130	80	2.6	702
LPCVD SRN	2400	180	6	0.8	691
Gold	19300	78	82	14.2	128

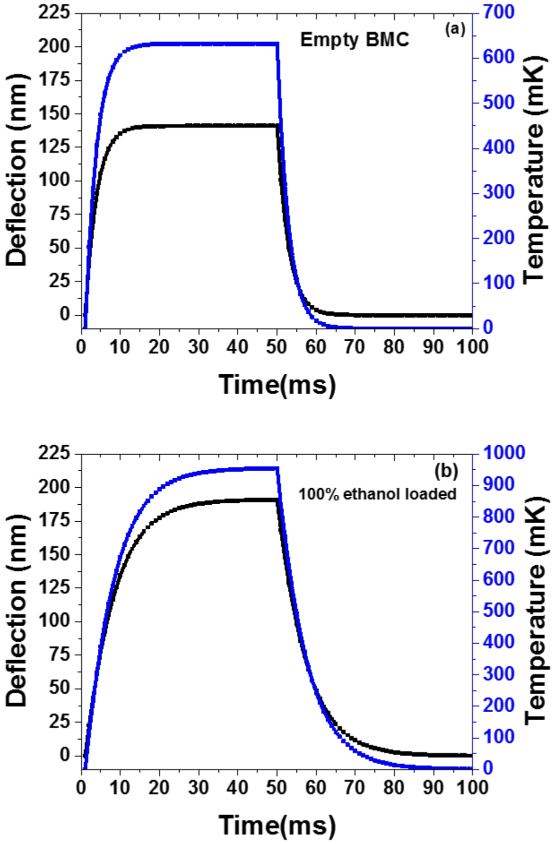

Figure 3.3: Simulated temperature rise and experimental dynamic response of the chip A at an absorbed IR power of 1.8 nW/μm^2 at 1053 cm^{-1} at 10 Hz IR modulation (a) for empty BMC (b) for absolute ethanol loaded BMC. The actual deflection of the BMC is presented as left side Y axis and predicted the temperature at the tip is presented as right side Y axis. Both the predicted and actual dynamic responses of BMC are in excellent agreement

The IR power is modulated using a function generator at various frequencies to obtain time response data. The differential equation is solved for $\theta(x,t)$ using Finite Difference Method (FD) considering δ x=5 μm and δt as one hundredth of laser heating period. The area of the fluid boundary ($A_{cx,3}$) is considered to be the cross-sectional area occupied by the fluid in the channel. Note that we have considered the convection loss (in fact gain)when the fluid inside acts as a thermal source due to IR absorption. The heat generated in the liquid thus has to travel to SRN walls and metal film beneath to reach thermal equilibrium. This has been represented as $L_p{}^*h^*$ in the equation. In the case of air filled BMC, there is no need of this term as IR is absorbed by SRN. More details about the theory can be found in the appendix.

Figure 3.3(a) shows the thermal response of BMC as a function of time when the hollow cantilever is empty i.e. filled with air at IR modulation frequency of 10 Hz at the free end of the BMC. The actual deflection response of the BMC is also presented for comparison. From the Fig. 3.3 (a), it is evident that the experimental and predicted dynamic responses are in excellent agreement. The thermal response is determined by the time the cantilever free end takes to reach thermal equilibrium upon IR illumination. The temperature rise at the free end of BMC is $\approx$ 580 mK. The thermal time constant (τ) is calculated as the time the cantilever tip takes to reach 66.7% of its maximum deflection. The time constant from predicted behavior of empty BMC is $\approx$ 3 ms. Fig. 3.3(b) shows the predicted thermal response of cantilever as a function of time when the hollow cantilever is filled with ethanol. The IR source is operated at a wavenumber where there is significant IR absorption of ethanol i.e, at 1053 cm^{-1} at IR modulation frequency of 10Hz. The predicted thermal time constant for ethanol loaded BMC is $\approx$ 12 ms and the temperature rise at the free end is $\approx$ 950 mK. The absorptance value used (A=0.25) in the model was obtained from experimental measurements. The increase in temperature rise and thermal response time in case of ethanol filled cantilevers compared to air is attributed to the way higher IR absorption of ethanol to generate more heat in the channel and added the thermal mass of the cantilever to reach thermal equilibrium. Note that the IR power used in prediction are the order of magnitude higher than the experimental IR power, hence higher deflection.

3.5 Process optimization

3.5.1 Optimization of IR modulation frequency

The real-time dynamic response of BMC at a wavenumber of 1045 cm^{-1} at maximum IR power has been recorded by an Oscilloscope as presented in the Fig. 3.4.

The thermal time constant has been calculated by drawing a perpendicular line at an amplitude where the BMC reaches 66.7% of maximum amplitude. The cut-off frequency is usually considered to be $f_m = \frac{1}{2\pi T}$. From the Fig. 3.4 it is evident that the loaded BMC has a higher amplitude and takes more time to reach thermal equilibrium. The higher amplitude of loaded BMC can be attributed to increased IR absorption by the liquid present in the BMC at the radiated IR wavenumber. As loaded BMC has high thermal mass, it takes more time to reach to thermal equilibrium. The thermal time constant for the presented chip B device is 3.9 ms for empty BMC and 9.8 ms for loaded BMC. Thus, the modulation frequency of the IR laser is optimized in such a way to give enough time

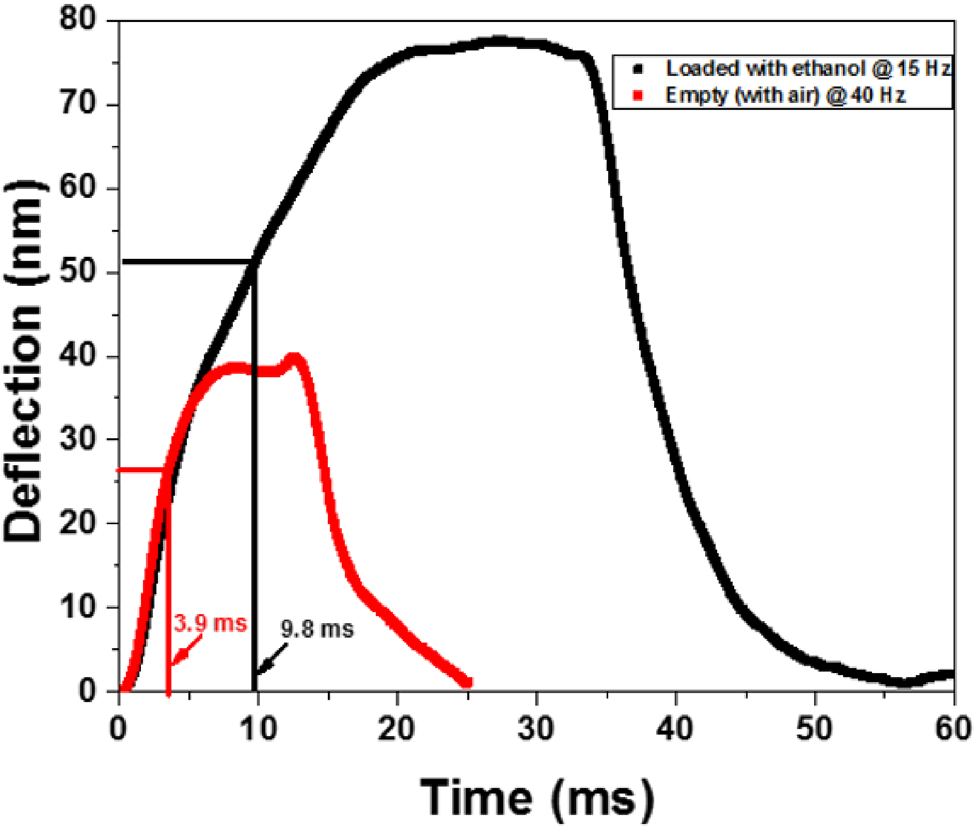

Figure 3.4: The dynamic response of the BMC when radiated with IR at 1045 cm^{-1} at 40 Hz IR modulation for empty BMC (red in color), at 15 Hz modulation frequency for ethanol filled BMC (black in color). The thermal time constant is shown as 9.8 ms in case of ethanol filled BMC and 3.9 ms in case of empty BMC.

for the cantilever to respond to thermal pulses completely. An optimum frequency of 40 Hz has been chosen as IR modulation frequency for an empty BMC, modulated using a function generator. In the case of a fluid filled BMC, the thermomechanical response is slower as compared to empty BMC due to more weight and heat transport characteristics. Hence, an optimum of 15 Hz has been chosen as IR modulation frequency for fluid filled BMC.

3.5.2 Optimization of metal layer thickness

The static deflection of the BMC to a temperature rise is dependent on the thermal expansion coefficient mismatch and the thickness of the metal layer. The thickness of the metal film is a critical parameter in sensitivity of BMC as it controls the deflection of the cantilever to the absorbed radiative power. Lai et al have showed that for the system of SiNx/Au, the maximum response was obtained for the optimum metal thickness ratio of 0.25 relative to SiNx thickness. They have also demonstrated 50% improvement in the response by optimizing the thickness ratio of two materials [74, 78]. Since, our device has a hollow channel made of SRN on top of the cantilever, the general optimum thickness ratio did not give maximum performance.

In order to optimize the best thickness of the metal layer, we have coated thin films of gold at various thickness on the same microchannel cantilever using a thermal evaporator. After making the cantilever a bimaterial cantilever, we have recorded the deflection of BMC when radiated at a particular IR wavenumber of 1053 cm^{-1} at maximum IR power at an IR modulation of 40 Hz. Each data point on the curve is an average of 15000 data points. The error bar represents the standard deviation in the measurement. From the Fig. 3.5it is evident that the deflection of the BMC increases with metal layer thickness up to a certain thickness and then decreases. The thickness at which maximum deflection occurred was considered for further analysis. Every time the device is tested for new metal layer thickness, the previous coating was etched completely and coated with a new thickness in the thermal evaporator. We have used 10 nm of Cr as an adhesion layer for all gold coatings. Fig. 3.5 shows the metal layer optimization for various designs chip A and chip B. Each chip has three cantilevers, hence each graph has 3 curves. From the Fig. 3.5, it is evident that chip A reached to its best sensitivity at 500 nm of Au and chip B at a thickness of 600 nm of gold.

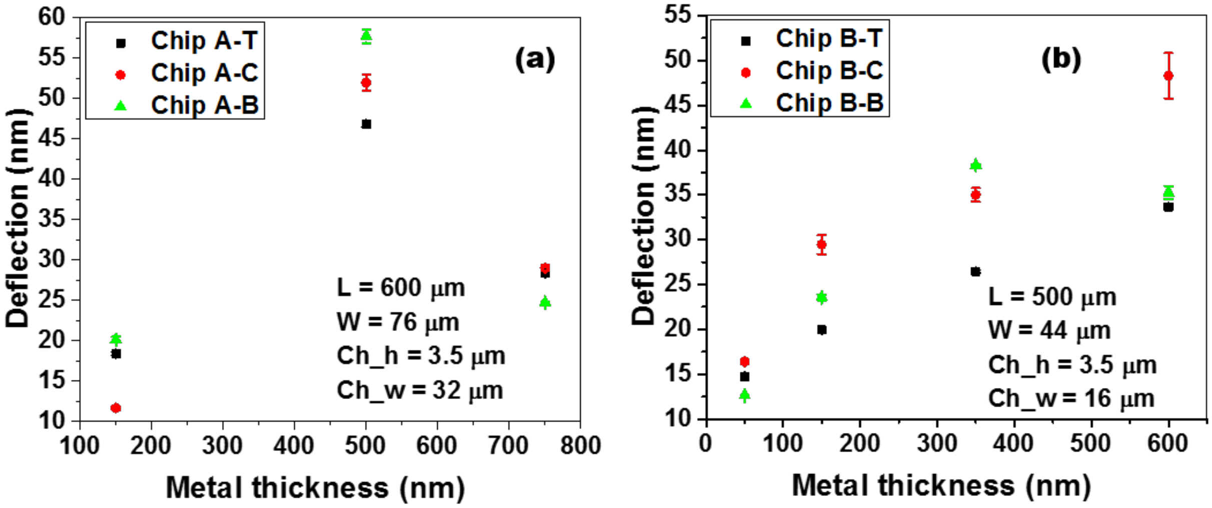

Figure 3.5: Deflection of BMC subjected to IR radiation at 1053 cm^{-1} at a modulation of 40 Hz, with respect to metal thickness for the devices a) Chip A, b) Chip B. Each chip has three cantilevers top (T), center (C) and bottom (B). Note that all cantilevers in a chip show similar behavior. The error bars have represented standard deviation in the deflection. The devices of maximum deflection were considered for further analysis.

3.5.3 Optimization of design parameters

BMC's of two design parameters have been tested for their thermal sensitivity and ability to detect lowest concentration of analyte using photothermal methods. We have fabricated BMC's of various dimensions and designs but here, in this section, only one dimensional parameter is emphasized that is the effective channel volume. Each chip contain 3 BMCs of same dimensions as mentioned in the table 3.2. We have fabricated BMCs of different volume by changing the length and width of the cantilever by keeping the channel height same.

3.5.4 Deflection sensitivity of PSD

We have used the same PSD for all the measurements. The deflection sensitivity of PSD, to convert voltage signals of PSD to actual cantilever deflection (nm) was performed by doing heating experiments on a gold-coated Si cantilever. NTA set up has been used to monitor the deflection of the cantilever while heating and cooling. The resulting amplitude from deflection of the BMC is plotted in Fig. 3.6. The exact same experiment is performed under a laser doppler vibrometer (LDV) in topographic measurement system

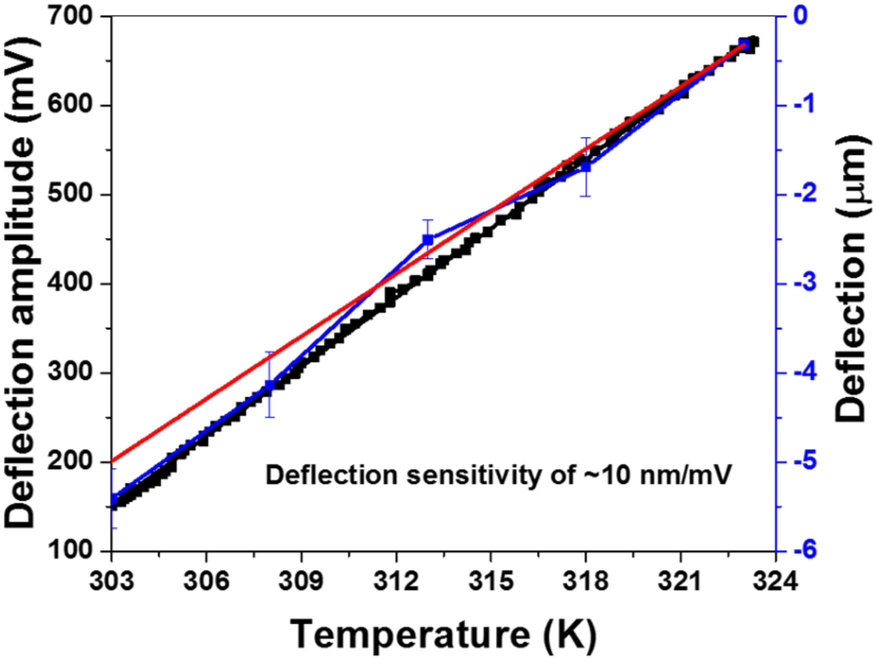

Figure 3.6: Deflection sensitivity of the PSD calibrated using LDV. The actual deflection of the gold coated microcantilever, subjected to external heating was measured using LDV as shown in right hand side Y-axis. The error in the measurement is shown in error bars (blue curve). Similar data was recorded using laser deflection method as shown in left hand side Y-axis. The deflection sensitivity of PSD was found to be 10 nm/mV.

Table 3.2: Details of different designs of BMC

Cantilever	**Chip A**	**Chip B**
Cantilever length (μm)	600	500
Cantilever width (μm)	76	44
Cantilever thickness (μm)	1	1
Metal coating material	Au	Au
Metal thickness (nm)	500	650
Channel height (μm)	3	3
Channel width (μm)	32	16
Channel volume (pL)	115.2	48

mode to observe the actual deflection of the cantilever with respect to temperature. The LDV signals are recorded three times while heating and cooling (shown in error bars) to obtain the best average deflection. The LDV data is indicated as right side Y axis in Fig. 3.6. The obtained values are verified by other methods of calibration such as calculation of thermomechanical noise amplitude using a spectrum analyzer. We have obtained a deflection sensitivity of 10 nm/mV for the considered SPC-PSD from SiTeck numbered S2-0171. The obtained deflection sensitivity is in agreement with the literature.

3.5.5 Noise measurement

Limit of detection using photothermal spectroscopy is limited by the noise in the measurement. There are various noise sources present in the system such as electrical noise, 1/f Johnson noise, noise due to laser beam attenuation, noise due to temperature controller, room temperature drift, convection and mechanical vibrations. As PCDS depends on the deflection of the cantilever to temperature changes induced by IR absorption, the thermomechanical noise of the device sets the fundamental limit. By careful design, the noise from the other sources can be minimized to the point where the thermomechanical noise dominates. In our analysis, we have considered the cumulative noise arising from all the sources to represent a real system. While measuring the thermomechanical sensitivity of the BMC, we have kept the BMC at constant temperature and recorded the deflection of the cantilever over a period of time. The standard deviation in the deflection signals represents the cumulative noise in the system. As shown in Fig. 3.7(a) the BMC in chip A is placed on the heater chuck at 303 K and recorded the deflection for 10 min. A noise of 15 nm is observed in the measurement as shown in Fig. 3.7 (a). This noise is arising

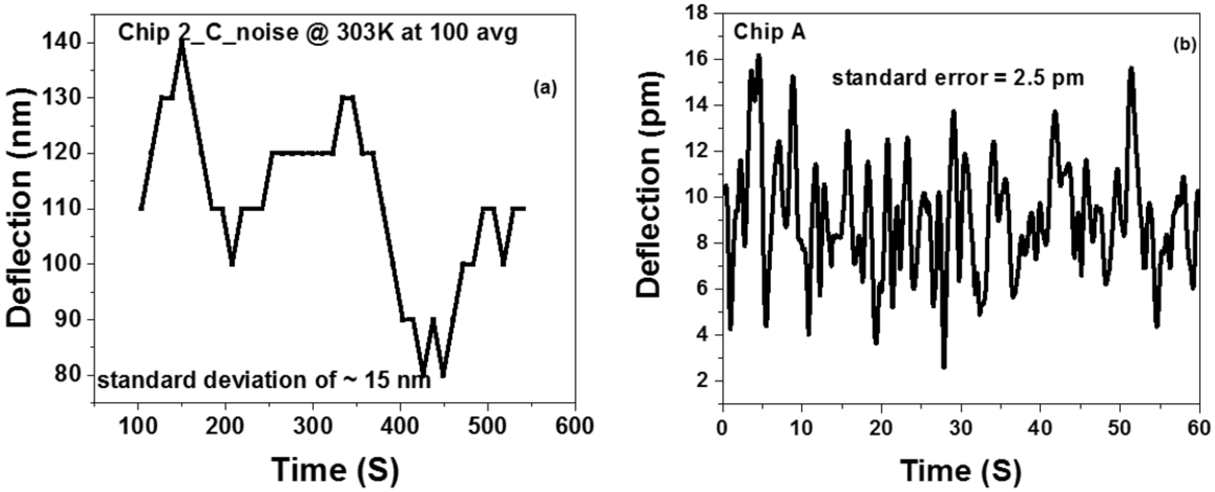

Figure 3.7: Noise measurement in finding the ultimate limits of thermomechanical sensitivity (a) Thermomechanical noise in chip A (chip 2) when the BMC is kept at 303 K for 10 min. (b) Thermomechanical amplitude of BMC in chip A measured using a lock-in amplifier locked to its resonance frequency at room temperature

mainly from the temperature fluctuations due to the temperature controller to keep the temperature at 303 K. In order to overcome temperature fluctuations by the heater we have recorded the data at room temperature under identical experimental conditions and found that noise value is ≈ 6 nm. As the data acquisition system is slow, it records one point in the deflection data after an average of 100 measurements hence contributing to the noise. As both the previous measurements do not represent the actual noise in the system, we have considered the noise in the thermomechanical amplitude of the BMC at its resonance frequency as the representative noise as shown in Fig. 3.7 (b). The variations in the peak amplitude of the thermomechanical frequency of the BMC were monitored using a loc-in amplifier locked at the resonance frequency of the BMC. The thermomechanical noise of the BMC was found to be 2.5 pm. Power sensitivity and photothermal spectroscopy measurements are performed by subjecting the BMC to periodic IR pulses. Noise measurements have been carried out by subjecting the empty BMC to IR pulses at maximum power. The deflection data has been recorded using a lock-in amplifier locked at IR modulation frequency. The standard deviation in the deflection signals when BMC is subjected to maximum IR power for chip A and chip B are shown in Fig. 3.8(a)and 3.8(b). It is evident that longer cantilevers such as in chip A have more noise relative to chip B. From the Fig. 3.7 and 3.8, it is to be noted that the noise is much higher in the measurement when the BMC is irradiated with IR at maximum power.

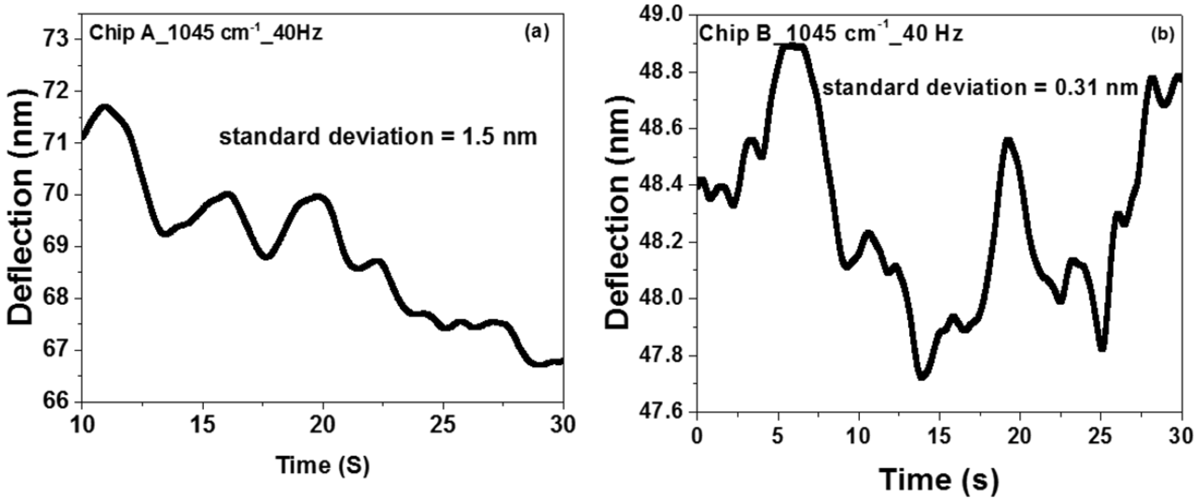

Figure 3.8: Noise measurement in finding the ultimate limits of power sensitivity (a) Noise in chip A when subjected to maximum IR power at 1045 cm^{-1}. (b) Noise in chip B under pulsed IR radiation at 1045 cm^{-1}.

3.6 Results and Discussions

3.6.1 Measuring thermomechanical sensitivity

Figure 3.9 shows the variation of BMC deflection with respect to external temperature. As the temperature of the chuck is increased the BMC shows a linear increase in the PSD signal indicating the upward bending of the cantilever and a reverse effect is observed while cooling. We assume that throughout the experiment the elastic properties of the materials does not change. The two curves in the Figure 3.9 correspond to BMC deflection data obtained while, heating and cooling thermal cycles. The heating program is optimized to provide enough time for thermal equilibrium at the end points of the cycle. The slope of the curve gives the thermomechanical sensitivity of the BMC to external temperature. In this configuration, the BMC is assumed to be in a uniform temperature bath where ΔT along the length of BMC is constant. In this configuration the BMC is essentially considered as a thermometer, thus one can estimate the temperature rise by looking at the deflection of BMC [83]. These experiments are performed on both the BMC designs to evaluate the effect of design parameters. From Fig. 3.9, it is evident that the designs of chip A and B have identical thermal sensitivities of 0.2 µm/K. Chip A has slightly better sensitivity compared to chip B because of higher length and low stiffness. These studies confirm the fact that the thermomechanical sensitivity has a higher dependency on length than

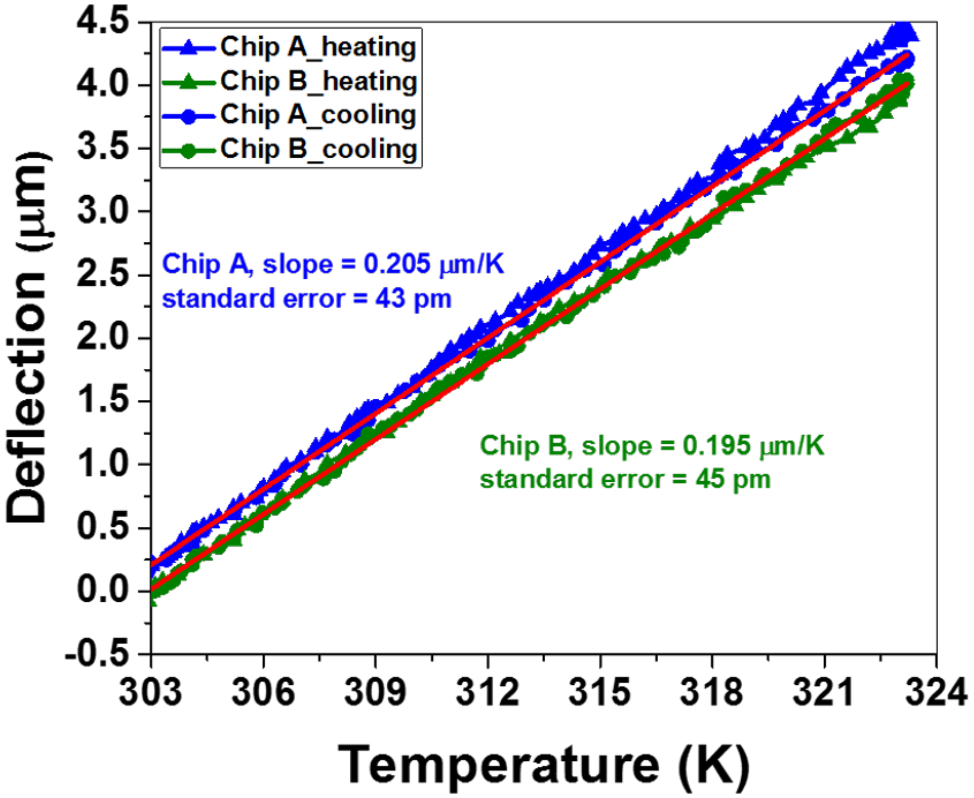

Figure 3.9: The deflection of BMC with respect to the change in external temperature while heating and cooling. The red line indicates the linear fitting in all devices. The standard error mentioned is the error in fitting a straight line to the data. It can be seen that chip A and chip B have an almost similar thermal sensitivity of 200 nm/K.

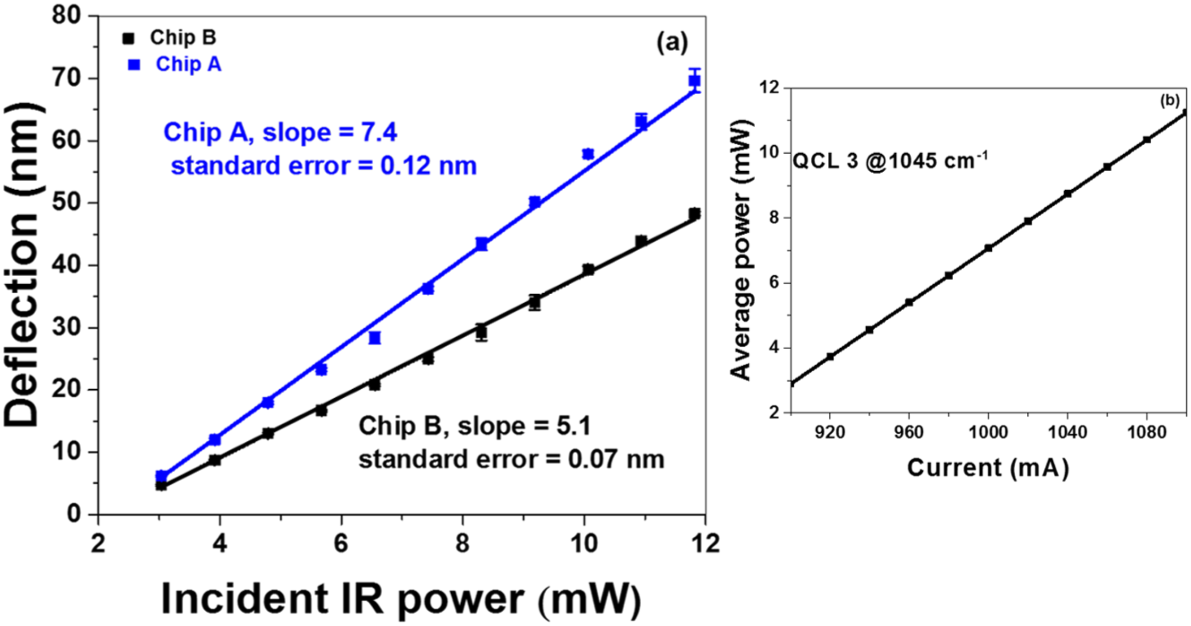

Figure 3.10: Deflection of BMC due to varying incident power of IR. The incident power of IR can be varied by changing the drive current to QCL. Each data point is an average of 15000 data points recorded when BMC is subjected to IR radiation at 1045 cm^{-1} at a modulation of 40 Hz. The noise in the measurement is depicted as error bars in the curve.

width. The temperature resolution depends on the thermal characteristics of the BMC and the noise in the measurement setup. The dominant noise sources in our experimental set up are room temperature thermal drift, electrical noise and thermomechanical noise of the BMC itself. The dominant thermomechanical noise of chip A is found to be $\approx$ 2.5 pm from Fig. 3.7. Considering a signal to noise ratio (SNR) of 3, the minimum temperature that can be measured using chip A is $\approx$ 4 mK. Note that better temperature resolutions have been reported in the literature up to $\approx 10^{-5}$ K but most of the reported values for temperature resolution are theoretically predicted and associated with triangular shaped cantilevers [87]. The poor thermal sensitivity of the BMC is attributed to design specifications and almost 4 µm thick cantilever system and higher noise associated with BMC. The minimum temperature that can be measured using the BMC gives an insight for the investigation of exothermic or endothermic bio-chemical reactions in confined volume.

3.6.2 Measuring power sensitivity

The measured deflection of the BMC due to varying incident IR power at 1045 cm^{-1} wavenumber is shown in Fig. 3.10 (a). The IR radiation is modulated at a frequency of 40 Hz and the deflection signal is locked in a lock-in amplifier to record the data. Each data point on the curve represents the average deflection signal of 15000 data points. The solid line in the curve is the least square fit to the data. The slope of the line indicates the response of the BMC to various incident IR powers. The incident power output of the QCL can be changed by providing different drive currents to the QCL as shown in 3.10 (b). From Fig. 3.10 (a), it is evident that chip A has higher power sensitivity than chip B. The higher sensitivity of the chip A is attributed to the lower stiffness of the cantilever and longer length as inferred from equation 2.11. Note that the noise reported (Fig. 3.8) is higher than thermomechanical noise (Fig. 3.7) mentioned before. This rise in noise when radiating the BMC with modulated IR is due to the photothermal activation and thermal drift in the cantilever system. From the experimentally observed standard deviation of 1.5 nm (Fig. 3.8), considering an SNR of 1 and the responsivity of 7.4 nm/mW, the minimum detectable power for chip A was found to be 202 μW. Since the time constant of chip A was found to be 4 ms, the estimated energy resolution was found to be $\approx$ 808 nJ. Chip B can detect as low as 60 μW, even though it has lower sensitivity. This is due to large noise associated with longer cantilever design. This indicates that though long cantilevers are more sensitive they do not always have the best resolution as the noise is also dominant. All the figures of merit associated with both BMC designs are mentioned in Table 3.3

The average power of IR at 1045 cm^{-1} at 1100 mA current that is reaching the BMC surface is 11.25 mW, neglecting the optical losses. The absorbed power (Q_{abs}) is calculated by the relation [74]

$$Q_{abs} = Q_{inc}\alpha\frac{A_{cant}}{A_{spot}} \tag{3.2}$$

where α is the absorptance of SRN at a thickness of 2 μm, A_{cant} is the area of the cantilever A_{spot} is the area of the radiated IR spot with a diameter of 2.5 mm and Q_{inc} incident power reaching the cantilever. The IR characteristics of BMC are very much dependent on cantilever dimensions, the thickness of constituent materials, absorptance of the BMC at radiated IR wavenumber. Though there are not many published reports available on the IR spectral characteristics of cantilevers, the absorptance of SRN cantilevers in most publications was found to be 0.15 [75, 77, 81]. For the same input laser flux, chip A shows larger response than chip B but the sensitivity of chip B is better than chip A for a normalized absorbed power calculated using equation 3.2. This is attributed to the smaller geometries of chip B to show better sensitivity to absorbed IR power. Chip A has a lower incident flux sensitivity to chip B because of larger dimensions and larger channel volume affecting the heat transport characteristics.

As a typical example, in the case of chip B, for an area of 500X44 μm^2, with an absorption coefficient of 0.15 for SRN/Au system, the absorbed power producing a temperature change can be calculated as 11.81 μW. Assuming 80% of photon energy is converted to heat due to non-radiative photon decay, the BMC produces a deflection of $\approx$ 50 nm. The thermal sensitivity of the BMC under similar experimental conditions was 200 nm/K as mentioned before in section 3.6.1. From these calculations, we can find that the temperature rise due to IR radiation at 1045 cm^{-1} can be approximately 250 mK. In the case of chip B, with a responsivity of 4.9 nm/μW (the slope of deflection vs absorbed power) and noise level of 0.31 nm, we can measure a power resolution of $\approx$ 63 nW and $\approx$ 240 pJ energy resolution. This is because of the low thermal mass of the BMC system that can produce large deflection responses with very small external stimuli. Hence, micromechanical photon detectors have to be made of low density, low specific heat materials covering large areas [71].

3.7 Figures of merit calculations

Table 3.3 summarizes the figures of merit of both designs of BMC measured under periodic IR radiation. The definition and formula for each figure of merit have been mentioned in the Table 3.3 [77]. From the table 3.3 it is evident that the responsivity of chip A outperformed chip B for the obvious reasons of low compliance, larger length and higher channel volume causing high IR absorption. The incident flux sensitivity (SIF) is more for chip B as it has lower cantilever area. Though the responsivity of chip A is best but it acquired higher noise equivalent power (NEP) due to more noise associated with long and slender cantilevers. Chip B possesses better NEP and noise equivalent flux (NEF) due to extremely low noise (0.31 nm) associated with moderate response to IR. The desired figures of merit in each category were represented in bold numbers for a better IR thermal sensor.

Table 3.3: Table of figures of merit for different designs of BMC

Figure of merit	**Definition**	**Formula**	**Chip A**	**Chip B**
Responsivity R (nm/mW)	Quasi-static tip displacement per incident radiative power	$\frac{1}{P_\lambda}\frac{dz}{dx}$	**7.4**	5.1
Incident flux sensitivity SIF, (10^{-5} nm.μm^2/mW))	Tip displacement per incident radiative power, per illuminated cantilever area	$\frac{R}{A_{cant}}$	16.22	**23.18**
Noise equivalent power NEP, (μW)	The limit on incident power that can be measured by the cantilever	$\frac{\sigma(\Delta Z)}{R}$	202	**60**
Noise equivalent flux NEF, (10^{-3} μW/μm^2)	The incident radiative flux that produces a signal to noise ratio of one	$\frac{NEP}{A_{cant}}$	4.42	**2.72**
Detectivity (μm/μW)		$\frac{\sqrt{A_{cant}}}{NEP}$	1.05	**2.47**

3.8 Photothermal Spectroscopy of liquids

3.8.1 Photothermal IR spectroscopy of ethanol in the presence of water

PCDS techniques add molecular selectivity to the innovative, highly sensitive platform of BMC considering it as a thermal sensor. To investigate the effect of design and parameter optimization on the limit of spectroscopy detection, we performed spectroscopy of ethanol in water-ethanol binary mixtures using BMC. Ethanol has been taken as an example for its simplicity in loading and preparing different concentrations. Ethanol-water binary mixtures are prepared in different concentrations of ethanol in water ranging from 20 wt% to 1 wt%. The BMC is loaded with a specific concentration of ethanol-water binary mixture and subjected to pulsed IR wavenumber scan from 1204 cm^{-1} to 960 cm^{-1}. In the case of loaded BMC, the IR modulation frequency is optimized to be 15 Hz due to the heavy thermal mass of the BMC and thermal transport characteristics after loading. The thermal time constant of the loaded BMC is in the order of 9.8 ms depending on

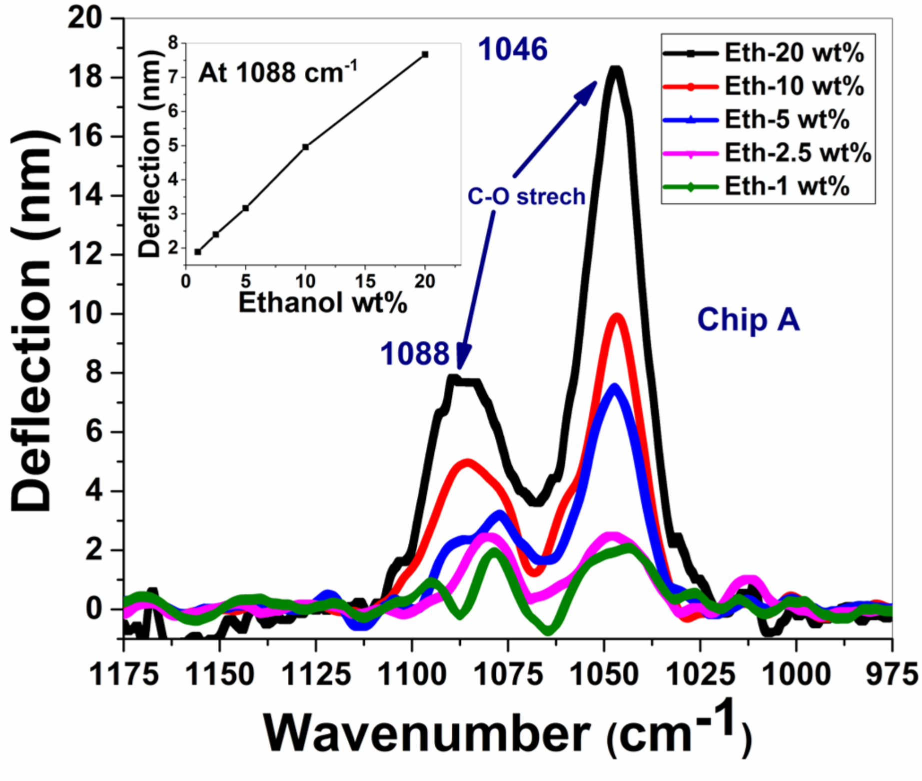

Figure 3.11: Photothermal IR spectra of ethanol at various ethanol concentrations, in the ethanol-water binary mixture obtained by monitoring the static deflection of BMC to IR wavenumber scan, modulated at 15 Hz using Chip A. Two signature IR peaks of ethanol due to C-O bond stretching can be observed as shown. The inset in Chip A shows the linear relationship of deflection amplitude with respect to ethanol concentration at 1088 cm^{-1}.

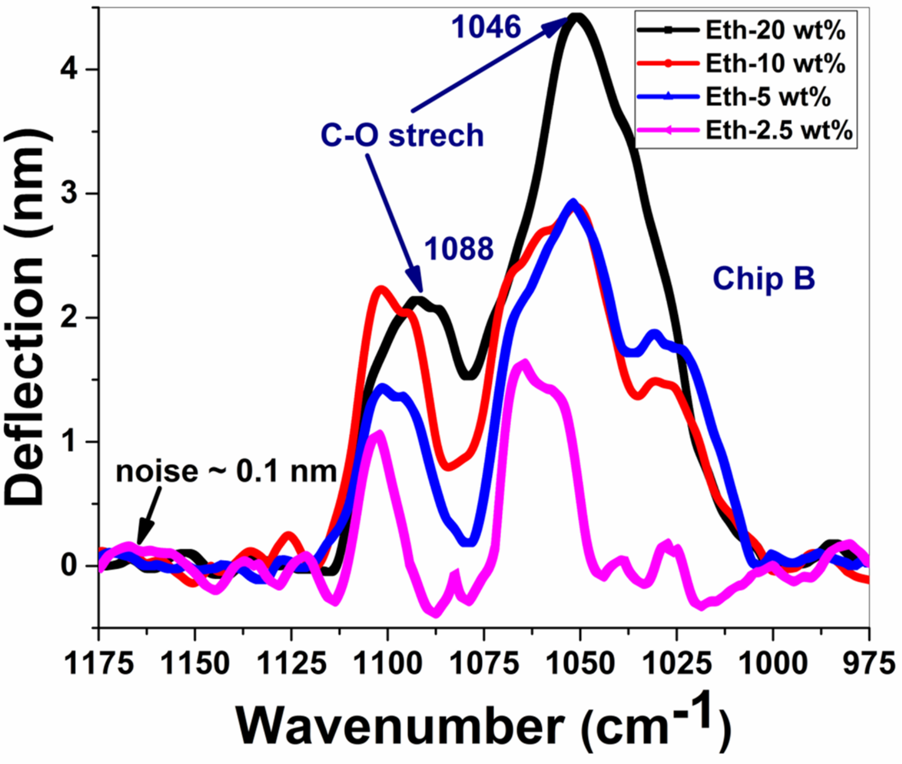

.

Figure 3.12: Photothermal IR spectra of ethanol at various ethanol concentrations, in the ethanol-water binary mixture obtained by monitoring the static deflection of BMC to IR wavenumber scan, modulated at 15 Hz using Chip B. Two signature IR peaks of ethanol due to C-O bond stretching can be observed as shown. Noise in the differential measurement is as indicated.

the sample loaded. Ethanol has two significant IR absorption peaks due to C-O stretch at 1046 cm^{-1} and 1088 cm^{-1} [128]. The scan rate is adjusted to 5 cm^{-1}/s to emphasize the fast measurement throughput of the current BMC system. The deflection of the BMC is continuously monitored using above-mentioned laser deflection method. The entire experiment right from sample loading to recording the scan data takes place within $\approx$ 2 minutes (50 sec for scanning). Along with spectroscopy information, the BMC platform has the ability to measure viscosity and mass density by observing the frequency related dynamics. BMC loaded with water was taken as the baseline for every new sample of the ethanol-water binary mixture. Fig. 3.11 depicts the deflection of BMC in chip A with respect to IR wavenumber. From the Fig. 3.11, it is evident that the deflection of BMC is higher at the wavenumbers where the constituents in the channel absorb IR and eventually result in temperature rise. The molecules in the BMC constituents undergo molecular resonance with the incoming IR radiation causing the molecule to absorb IR at that particular wavenumber that is specific to the molecular bond configuration. A continuous decrease in the characteristic peaks of ethanol can be observed with respect to decrease in the concentration of ethanol. The inset in the Fig. 3.11 indicates the decrease in peak amplitude of 1088 cm^{-1} with respect to decrease in the ethanol concentration showing the linear behavior of spectroscopy. Fig. 3.12 indicates the photothermal IR spectrum of ethanol loaded in chip B. It is to be noted that photothermal IR spectrum of ethanol has been presented only up to a concentration of 2.5 wt%. After this concentration, the characteristic IR peaks of ethanol are indistinguishable indicating the minimum concentration that can be detected using chip B. In the case of chip A, characteristic IR peaks of ethanol are distinguishable up to a concentration of 1 wt%. The lower limit of detection in case of chip A is attributed to higher sensitivity, higher channel volume, higher IR absorption and lower stiffness of chip A relative to chip B. This indicates that the current chip A design can detect $\approx$ 1.15 ng (1 wt%) of ethanol in 113.85 ng of water background. In our previous publication [103], a wavenumber step scan has been used to detect as low as 5 wt% ethanol in ethanol-water binary mixture with much higher IR laser power, whereas here we report the detection of 1 wt% (1.15 ng) of ethanol at low IR power and at much faster measurement time. This is an order of magnitude improvement from the previous publication with better throughput measurement. The spectroscopy data presented in Fig. 3.11 and 3.12 are the deflection of the BMC after substraction of water baseline. The noise in the differential measurement is $\approx$ 0.1 nm as indicated in Fig. 3.12. For a SNR of 1, the limit of detection in photothermal spectroscopy using chip A can be as low as $\approx$ 100 pg.

3.9 Summary

In summary, we have optimized the most influential parameters of a BMC when used as a thermal sensor and demonstrated the limit of detection of the spectroscopy signal from the analyte for an optimized BMC design. The experimental results demonstrated are in excellent agreement with the theory discussed. Highest sensitivity was obtained for a BMC of longer length, low compliance, and higher channel volume. For the same incident IR power, higher area BMC absorbs more IR power and deflects more. However, it is important to consider that long and slender geometry also increases the noise that has adverse effects on power resolution and mass resolution. Miniaturized BMC designs might have better thermal sensitivity in dynamic mode than static mode. Efforts to improve the IR absorption by fabricating a device with grating structures can be of great aid in lowering the resolution. From the above discussions, it is evident that large area and longer cantilevers have better responsivity but their large dimensions pose limitations to the miniaturization. Hence, one should aim to achieve a balance between mass sensitivity and thermal sensitivity in order to obtain quantitative and qualitative information.

3.10 Conclusion

Photothermal techniques can be a great aid in imparting chemical selectivity to the new class of SMRs targeted for bio-sensing applications. Immobilized chemo-selective interfaces can only provide partial selectivity and adds complexity to the process due to weak intermolecular interactions. Here in this chapter, we provide a detailed analysis of factors affecting the performance of a BMC when used as a thermal sensor. Several figures of merit were measured such as responsivity, incident flux, NEP, NEF, detectivity and thermal sensitivity. We have demonstrated the parameter optimization to detect molecular signature from as low as 1.15 ng of the analyte with the current design. The analysis provided in this chapter demonstrates a minimum measurement of 60 μW of power, the energy resolution of $\approx$240 nJ and temperature resolution of $\approx$ 4 mK. Efforts are underway to improve the resolution by minimizing the noise in the measurement and improving the response of BMC to periodic IR. The BMC can hold small volumes (pL) of confined liquid samples and possess the ability to give simultaneous information on density, viscosity, and molecular signature using spectroscopy and insight of thermal properties within few minutes. In the advent of using NEMS resonators, not just for mass sensing rather as analytical tools, we emphasize this kind of detailed analysis is essential to extend the applications of BMC in a biosensing and fundamental understanding of biochemical reactions.

Chapter 4

Investigation of Dynamic thermal properties of liquids using microchannel cantilevers

4.1 Overview

Bimaterial microchannel cantilevers (BMC) when investigated as a thermal sensor possess the capability to measure picojoule energy resolutions accurately. In the advent of using microcantilevers not just for mass sensing but also as analytical tools an immediate need exists for a technique, which is compatible with Lab-on-a-Chip platforms to perform thermophysical characterization of extremely small volumes of liquids. BMC if well explored can become a potential platform for cost-effective and rapid on-line measurement of dynamic thermal properties of liquids. We have used BMCs to estimate dynamic thermophysical properties of the constituents and density of picoliter volumes of various liquid reagents such as ethanol, acetone, water, methanol, n-heptane, n-butanol and toluene. The dynamic behavior of the BMC under periodic IR radiation is highly dependent on the heat transfer within and outside the BMC, thus by careful examination of BMC behavior we can estimate the dynamic thermal properties such as heat capacity, thermal diffusivity and thermal conductivity. The density of the liquid is calculated from changes in the resonance frequency of the BMC due to the loading of the liquid. This chapter emphasizes on the versatility of BMC platform to extend its applications to analytical tools.

4.2 Motivation/problem definition

Rapid growth in the nanotechnology made significant strides in the industry in terms of use of nanoparticles and colloidal suspensions made of nanoparticles. It has been reported that nanofluids have the amazing capability to transfer heat [129, 130]. Colloidal solutions of nanoparticles are not only used in thermal management in the microelectronic industry but also in cancer therapy. In these applications, it is extremely important to characterize dynamic thermo-physical properties of suspensions or colloidal solutions or even liquids for that matter. Characterizing extremely small volumes of liquids have been of great interest for researchers because of their potential applications in industry [131, 132]. A versatile tool that can rapidly measure physical and thermal properties of suspensions with easy integration are in high demand. Recent advances in Lab on a Chip platforms allow manipulation of liquids in microliters and smaller volumes. However, many challenges exist in developing compatible, online and inexpensive techniques which can be used for rapid characterization of small volumes of liquids. Precise knowledge of the thermophysical properties of liquids at a nanoscale level is required in applications such as calorimetry, micro total analysis systems (microTAS), micro heat sinks and microreactors. To characterize a liquid sample in temperature domain, thermal diffusivity is considered representative since it combines two important thermal properties; heat capacity and heat conductivity. Knowledge of thermal diffusivity of a sample also assists in determining the propagation rate of transient heat through a sample. Density, particularly, provides information about the behavior of a liquid reagent at different temperature and pressure. The thermal transport phenomena in nanofluids are not well understood and many of the theories in this regard have been controversial [133]. We hope that BMC platform can be used to investigate the thermal transport phenomena in nanofluids by monitoring the dynamics of BMC.

4.3 Introduction

4.3.1 Conventional Large Scale Techniques

Conventionally, transient hot-wire technique is used to measure the dynamic thermal properties where a micron scale wire is used as a heating element [134, 135]. The change in resistance of the wire is monitored to reflect thermo physical properties of the sample. This technique gives satisfactory results in solids and liquids [136, 137] but requires high sample volume/quantity. The accuracy of this method is dependent on the ability to measure absolute temperature accurately. This becomes more challenging in conducting liquids, especially at microfluidic scale [138]. On the other hand, photoacoustic (PA) spectroscopy has been proposed as a sensitive technique to measure multiple thermal and physical properties of thin films and liquids using acoustic dynamics of photo-induced thermal state of the sample. Many researchers have employed this technique to characterize polymers [139], hydrocarbons [140]and alcohol [141]. In this method, heat is produced by light absorption (by a sample) and heat propagation is measured in the form of a photoacoustic signal. The acoustic signal is measured by an external microphone. The signal is a function of the absorption coefficient and thermal diffusivity of a liquid sample. The amplitude and phase of the PA signal are monitored to estimate the thermo physical properties of the whole assembly of structures under investigation. Unfortunately, this method is not very sensitive as it is dependent on the sensitivity of a microphone. Additionally it has limited ability to perform measurements using small sample volumes. The bigger size of PA apparatus, such as an open-photoacoustic cell, also lacks the ability to be well integrated with microTAS systems [141, 142].

4.3.2 Modern Miniature Sensors

To handle small volumes of liquids, Y. Cheng et al. reported a microscale CMOS sensor which may be considered a variant of transient hot wire [136] or transient hot stripe [143]. Unlike these conventional techniques, the CMOS sensor has a separate thermal heater and a temperature sensor which eliminates some uncertainties, present in the conventional methods, mainly introduced by single wire heater and sensor. As the sensor needs a droplet to make a measurement and it's response time is few seconds, it cannot effectively be integrated with a Lab-on-Chip setup, where a sample may also be flowing. R. Beigelbeck et al. demonstrated a set of microbridges [144] which are improved version of the sensor presented by J. Kuntner et al. [145]. The microbridges incorporate a heater and two thermistors and have the ability to simultaneously measure thermal diffusivity and thermal conductivity. Thermal properties of liquids are measured by applying an ac signal at the heater to measure (by using thermistors) frequency response of heat produced and using an analytical model to extract thermal properties of liquids. Although the microbridges are small in size but to take a measurement, they have to be immersed in a liquid container. This makes them ineffective for an on-line measurement of thermal properties for microfluidic applications. Since many researchers are exploring the physics of nanofluids [146,147], it is important to have a tool which can deliver the thermal properties of liquids at picoliter volumes. There is an immediate need for miniature tools which offer rapid and cost effective measurements [148]. In this article, we introduce a BMC platform to estimate heat capacity, thermal diffusivity and density. Unlike current sensors, the BMC offers the advantages of being a quick, convenient and inexpensive method to thermally characterize a liquid reagent. It uses picolitres of a liquid and provides a closed container for its online thermal characterization with or without a flow. Unlike electrical heating, the liquid is heated with a precise wavelength and power of light and its properties are detected by sensitive mechanical changes in the cantilever. The BMC incorporates a sealed microfluidic channel and is capable of detecting minute amounts of localized heat changes. Using a specific wavelength of light provides much better control over heat absorption than using a thermally heated liquid.

4.4 Methodology

Microchannel cantilevers have been used in optical spectroscopy [103], mass sensing [149] and viscosity measurements [150]. Since then, BMC has proven to be an effective platform for suspensions and liquid analysis [103], there is also a possibility that it could be used to estimate the thermophysical properties of low volumes of liquids. Unlike mass sensing, the static deflection of a microchannel cantilever is employed in the thermal characterization of liquids. In this study, we have investigated the thermomechanical behavior of a BMC (filled with different liquid samples) and utilized that behavior to get an insight of thermal transport properties of the liquid. A thin coating of aluminum (Al) is sputtered on the back side of the silicon rich nitride (SRN) BMC in order to convert the platform into a bimaterial system. As the BMC is irradiated with a specific wavelength of light, the liquid inside absorbs the light. Due to non-radiative decay, this results in the generation of localized heat. The heat generated inside the liquid travels towards the microchannel walls and reaches the metal layer underneath the BMC. Ultimately, this causes the mechanical structure of the BMC to bend. This bending is a result of the thermal stress created by the thermal expansion mismatch of the structural layers (SRN, Al).

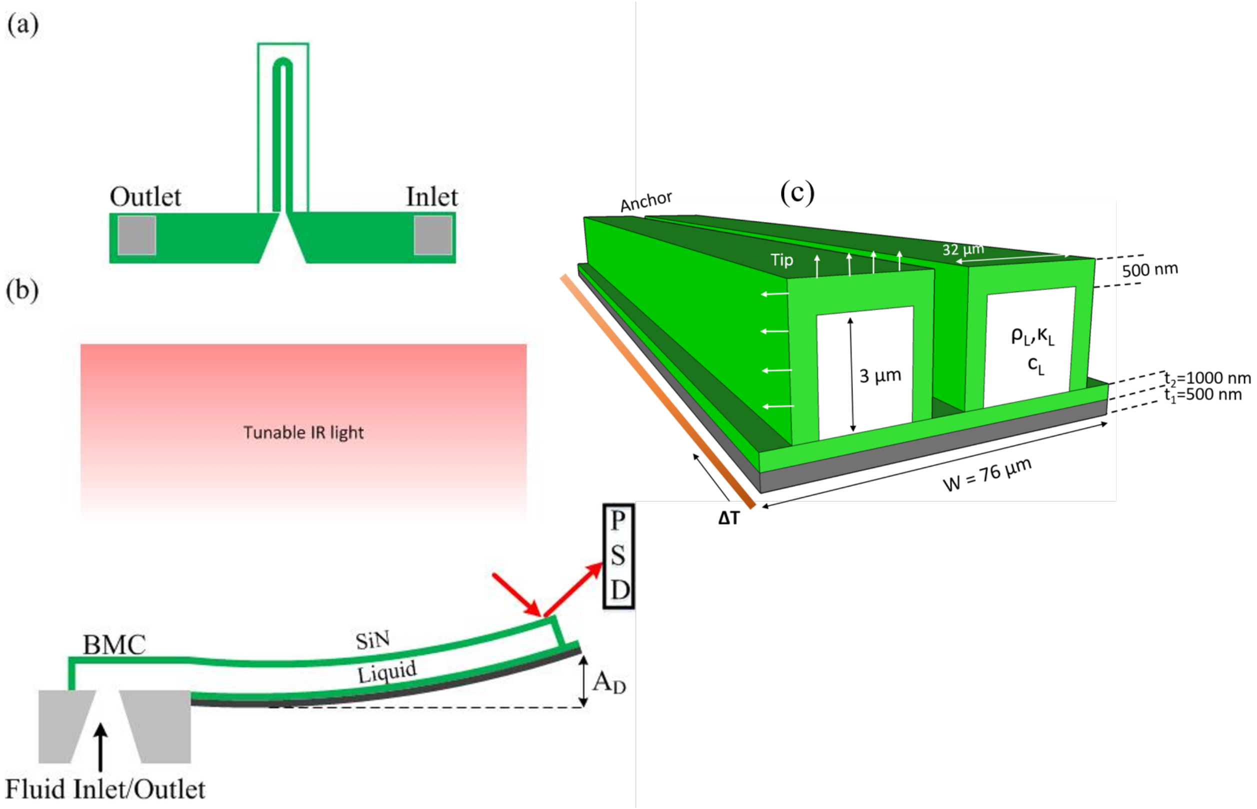

Figure 4.1: (a) Schematic showing the top view of the BMC. (b) Schematic showing the experimental setup where the BMC is subjected to modulated IR radiation and a PSD is used to measure the deflection of a BMC. Liquid is injected from the bottom of the substrate with a specially designed BMC holder. (c)Cross section of the BMC with a thickness of Al and SRN layers. Note that the image is not drawn as per the scale.

4.5 Experimental set up

The BMC is 76 μm wide, 600 μm long and operates under a spring constant of about 0.03 N/m. On its top, a 3 μm high and 32 μm wide microfluidic channel is fabricated (as shown in Fig. 4.1(a,b)). It can accommodate a liquid with a volume of 115 pL. The cantilever is turned into a bimetallic structure by depositing a 500 nm thick layer of aluminum at its bottom. The fabrication details of the BMC are available elsewhere [103, 125]. The BMC is illuminated with pulsed IR light produced by a tunable QCL called MIRcat (Day Light Solution, USA) which provides a peak to peak power of over $\approx$ 220 mW at 1053 cm^{-1}. The beam diameter of the laser spot is $\approx$ 2.5 mm in the radial direction. The QCL is operated in a pulsed mode as a square wave with a switching frequency of 100 kHz and a duty cycle of 5%. The incident IR flux on the cantilever is calculated to be 1.8 nW/μm^2.

The BMC deflection is proportional to the thermomechanical sensitivity of the device, incident IR power, irradiation time, the IR spectral characteristics of the liquid (inside the microchannel), the heat transfer ability of the liquid and the difference of the thermal expansion coefficient of the BMC materials. To acquire maximum deflection, it is very important to irradiate a reagent inside the BMC for an optimal length of time. When the liquid inside the microchannel absorbs IR light at a specific wavelength, the BMC bends out of the plane. In order to relax the BMC, it is important to switch the IR light off, before tuning the IR source to another wavelength. In this way, it is available to respond to the next pulse at the same or different wavelengths. Therefore, the 100 kHz frequency of IR light needs to be further modulated by an appropriate modulation frequency (f_m). Previously, researchers used mechanical choppers [96]to pulse IR light while we used a lock-in amplifier (SR850, Stanford Systems) to drive a function generator (at f_m) which further drives the IR source at a switching frequency (f_s) of 100 kHz [92]. The deflection of the BMC is recorded by reflecting a visible laser to a position sensitive diode (PSD). In order to record the time constant (τ), resonance frequency (f_r) and deflection amplitude (AD) of the BMC, the vertical signal of the PSD is fed to an oscilloscope, spectrum analyzer (SR760, Stanford Systems) and lock-in-amplifier, respectively.

4.6 Results and Discussions

Fig. 4.2(a) presents thermomechanical deflection of the BMC while it is filled with air and ethanol. It is irradiated with IR at 1060 cm^{-1} for 100 ms (f_m =10 Hz). During an ON cycle of 50 ms, SRN in the BMC absorbs IR and localized heat is produced in the BMC structure. Due to a large difference of $22.8X10^{-6}$ K^{-1} in thermal expansion coefficient of SNR and aluminum, the BMC deflects upwards in a short span of time. Note that the data presented is actual values of the PSD signal without normalization. The BMC deflects in 21 ms and remains in saturation for 29 ms. After a steady deflection, because of availability of limited heat, the BMC goes into saturation. This is due to a continuous conductive heat loss through 500 nm thick layer of Al as well as SNR. Additionally as the experiment is performed at room temperature in open air, there is also a convective heat loss through SNR and Al layers. Once the IR light is turned OFF, the BMC settles back to its equilibrium position. The settling time is also dependent upon the rate of conductive and convective heat loss through the anchor and the suspended body of the BMC, respectively. To calculate the respective time constant, BMC's response is fit with exponential decay function, as shown in the bottom inset in Fig. 4.2(a). The thermal response is determined by the time the cantilever's free end attains thermal equilibrium upon IR illumination. From the exponential fit, the time constant (τ_{air}) for ON cycle is calculated as 3.85 ms. The calculation is performed at 63.2% of the total amplitude of each cycle. The time constant for the BMC (filled with air) is comparable to the one reported by B. Kwon et al. for a cantilever with similar length but without a microchannel [77]. The time constant is mainly dependent upon heat capacity, heat conductivity and density of the material inside the microchannel. As the response time of the BMC is shorter than 83 ms, reported by R. Beigelbeck et al. [144], it is very much suitable for continuous characterization of reagents flowing through its microchannel.

Next, the BMC is filled with 99.9% ethanol and irradiated with IR for 50 ms (f_m=10 Hz) at 1060 cm^{-1}. Depending upon its heat capacity, the 3 μm thick layer of ethanol stores some amount of heat while surplus heat is transferred to Al layer underneath the cantilever. As compared to the BMC filled with air, in this case, it takes longer time for the cantilever to reach to saturation in 29 ms but its deflection amplitude is approximately 35% higher than the case when the BMC is filled with air. As shown in the insets, with the help of exponential fit, the τ ethanol for ON cycle of IR light are calculated as 7.59 ms which is almost double than the air filled BMC. As compared to air filled BMC, such a big difference in time constant and deflection amplitude (of the ethanol filled BMC) can be attributed to; larger thermal mass, larger heat capacity and higher IR absorption at 1060 cm^{-1}, which makes the BMC take longer to reach thermal equilibrium. As ethanol has higher thermal conductivity, it may also cause a faster heat loss through the anchors of the BMC. As shown in Fig. 4.2(a), with air inside the microchannel, the BMC exhibits the higher deflection. This is mainly because SRN absorbs IR which results into heat inside the structure. From Fig. 4.2(a) two important facts are observed. The first one is a significant decrease in the magnitude of deflection amplitude of the BMC and second is the time response under identical experimental conditions without and with liquid inside. From the previous knowledge of the thermomechanical behavior of BMC, the deflection amplitude of BMC is dominated by the IR absorbed power and time response is dominated by the thermal mass of the BMC with liquid inside. The slower thermal response of the loaded BMC can be attributed to the heavy thermal mass of the BMC, but the decrease in deflection amplitude presents more interesting observation.

Fig. 4.2(b) further explains the thermomechanical nature of the BMC using different time periods of IR radiation. The BMC is irradiated for different time periods defined by a series of modulation frequency; f_m = 15, 40, 50 and 80 Hz. For f_m = 15 Hz, the cantilever

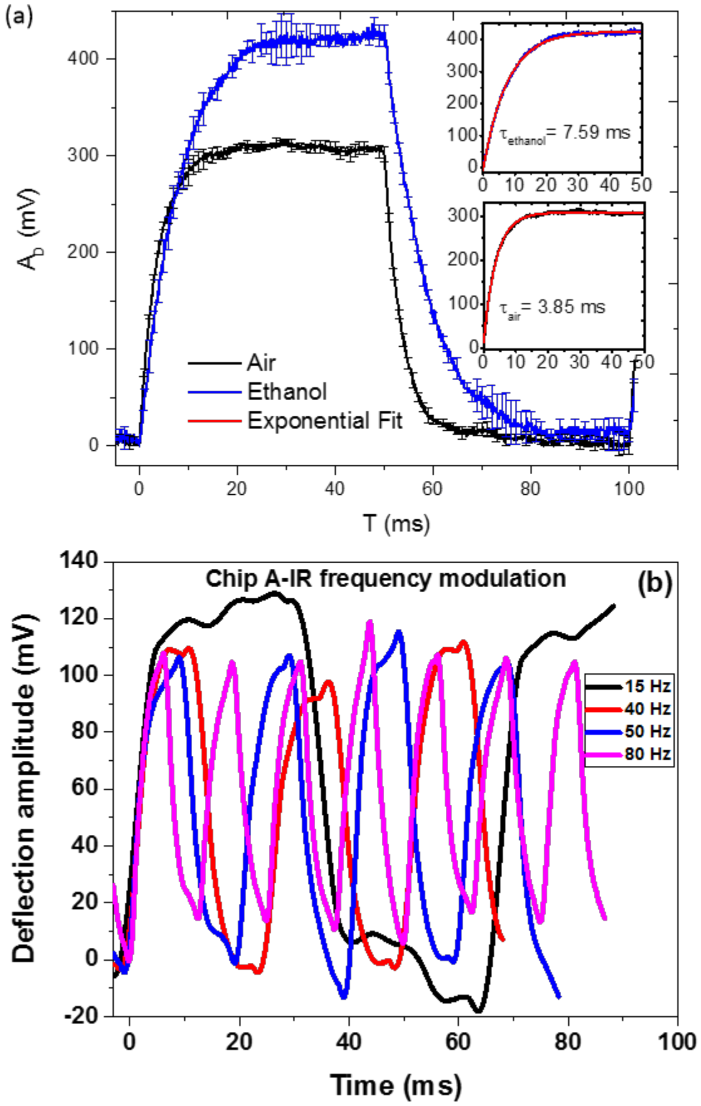

Figure 4.2: The dynamic behavior of the BMC to periodic IR radiation at (1060 cm^{-1}) operated at a repetition rate of 100 kHz and modulated at different frequencies (f$_m$). (a) The thermomechanical response of the air filled BMC and ethanol loaded BMC under IR radiation. (b) The dynamic behavior of air filled BMC at different IR modulation frequencies. Note that at higher IR modulation frequency, the signal is poor because the BMC is not getting enough time to experience the thermal stress.

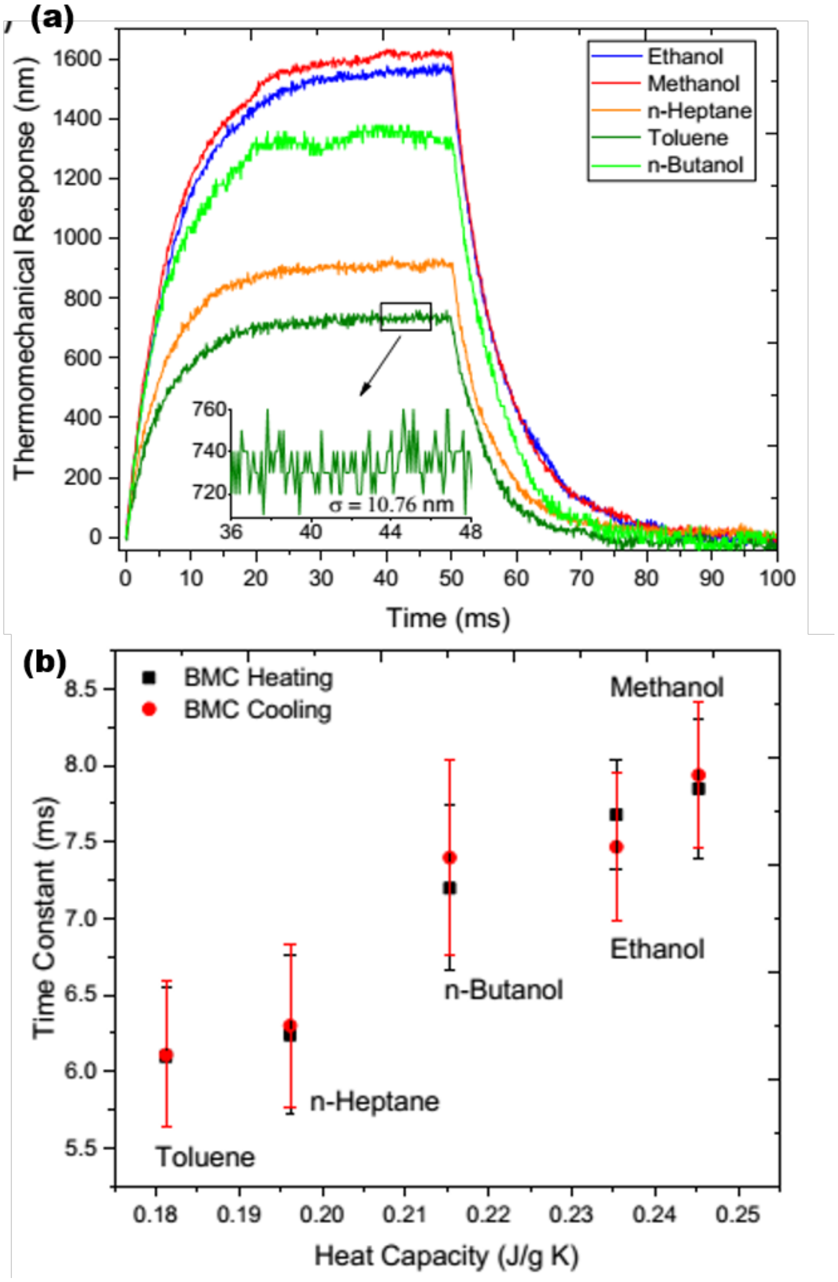

Figure 4.3: (a) Thermomechanical response of BMC filled with five different solutions of same concentration and radiated with IR light at 985 cm^{-1}. Note that only silicon nitride has significant IR absorption at that wave number. The liquids are just participating in heat transfer generated by the cantilever casing. The thermomechanical response of the BMC depends on the thermal properties of the BMC constituents. (b) The time constant of each liquid is plotted against mass weighted average heat capacity.

has lot of time to fully saturate to its maximum deflection amplitude and return back to its original position of approximately 0 V. At f$_m$ = 40 Hz, the BMC has just enough time to respond to heat completely. Thus the optimized IR modulation frequency for air filled BMC is 40 Hz. For f$_m$ = 50 Hz, the BMC starts from a resting position. As it gains optical energy it starts deflecting, however, before it reaches its equilibrium position, the IR light is turned off. This causes the BMC to lose all heat and begin returning to its original position. Before all the heat is lost, the IR light is again turned on. As a result due to the short time period, it starts a new cycle with some heat retained from the previous cycle. This causes the BMC to deflect at a higher amplitude in its second cycle. This effect is more prominent for both f$_m$ = 50 Hz and f$_m$ = 80 Hz. At f$_m$ = 80 Hz specifically, the BMC takes three cycles to reach to a constant level of amplitude for all the following cycles. Until the BMC reaches to equilibrium, the conductive and convective heat losses are dominant, however, after a time period of 33 ms, the BMC attains equilibrium.

To measure thermal transport of different liquids, the BMC is loaded with a series of five different liquid solutions; ethanol, methanol, n-heptane, n-butanol and toluene. Here it is important to irradiate the BMC with a wavelength of IR so that liquids does not absorb IR thus contributes no heat generation. Here the liquid is only transferring the heat generated by the solid SRN IR absorption to the anchor part of the BMC. Though the heat conduction through the SRN walls is much faster than convective heat transfer, we found that different liquids in the channel behave differently in transporting the heat to the anchor. This provides optimum conditions to test thermal properties of the liquid samples. Thus, the BMC is irradiated with IR of 985 cm^{-1}. Although, at this wavelength, none of the fluids have significant absorption of IR light but SRN absorbs a considerable amount of IR light [151]. The time response of different BMC systems loaded with different liquids is different as shown in Fig. 4.3(a). Note that the concentrations of all liquids used in this experiment are same. From Fig. 4.3(a) different liquids in the microchannel contribute to different heat losses in the system. The rate of heat loss defines the time constant of the BMC. The time constant of BMC is directly related to thermal conductivity (k_L), molar heat capacity (c_L) and density (ρ_L) of BMC constituents. All these properties are collectively represented by thermal diffusivity ($k_L/(c_L\rho_L)$) which is the prime indicator of heat transfer efficiency in materials. Therefore, it can be stated that the time constant of the BMC is a function of the thermal diffusivity of a liquid, present inside its microchannel. Note that the thermal time constant of the BMC is the effective heat transport characteristic of the whole BMC, not just the fluid in but on a relative scale, dynamic thermal properties of liquid dominate. As shown in Fig. 4.3(a), once the

BMC reaches to saturated deflection, the noise is quite profound which also introduces slight variations in the time constant with every cycle. Therefore, it is very important to record BMC deflection over multiple cycles and take an average value for a time constant. For ethanol, the average time constant is measured as 7.58 ms.

After ethanol, the BMC is emptied and dried with dry air. In order to confirm the BMC is clean, the resonance frequency f_r is recorded to be 16.188 kHz. Later, the BMC is loaded with n-Heptane, water, methanol and toluene. The deflection amplitude and time constant of the BMC with every liquid is recorded. After every solution, the BMC is dried and the resonance frequency is measured to ensure cleanliness.

Most influential parameter in affecting the thermal diffusivity is the thermal capacity of the constituents. Hence we focused to measure heat capacity of the BMC constituents. In order to measure the heat capacity , the BMC is loaded with five different liquid solutions, methanol, ethanol, n-heptane, toluene and n-butanol. Fig. 4.3(a) presents thermomechanical response of the BMC filled with the five different solutions. It is evident that the BMC exhibits different responses (time constant and deflection amplitude) with different solutions due to their different thermal mass and heat transfer characteristics. Since the thermal time constant, $\tau_{th} = \mathrm{R}_{th}\mathrm{C}_{th} = (L/kA)(\rho C_p V)$, mainly depends on collective thermal conductivity (k), heat capacity (C_p) and density (ρ) of the sample filled BMC since the length (L), cross-sectional area (A), and volume (V) are fixed for a given BMC. The effect of thermal properties of each material can be calculated by mass-weighted average value, where liquid sample, SiN and Al constitute ≈8.53-10.6%, ≈81.21-84.76% and ≈6.43-6.71% mass of the BMC, respectively. With these proportions, the thermal conductivity and density of all tested liquids are smaller than those of SiN and Al by two orders of magnitude. Therefore, the time constant of the sample filled BMC is not sensitive to these two parameters of the liquids. However, heat capacity of the liquids is comparable to that of SiN and higher than that of Al by two orders of magnitude. Therefore, the heat capacity of a liquid present in the BMC plays a dominant role in determining the temporal thermomechanical responses of the BMC. For example when BMC is filled with methanol, the average time constant (heating and cooling) is measured to be 7.85 ± 0.45 ms which corresponds to the mass-weighted average of heat capacity (C_{pm}) of methanol, SiN and Al as 0.24, 0.58, and 0.06 J/g K, respectively. In Fig. 4.3(a), inset shows a zoom-in view of the steady state deflection of the BMC, filled with toluene where the steady state noise level of the quasi-static deflection is measured to be 10.76 nm. For all tested liquid samples, the noise and signal-to-noise ratio (SNR) range from 10.76 nm to 21.6 nm and from 68:1 to 78:1, respectively. In order to calculate mass-weighted

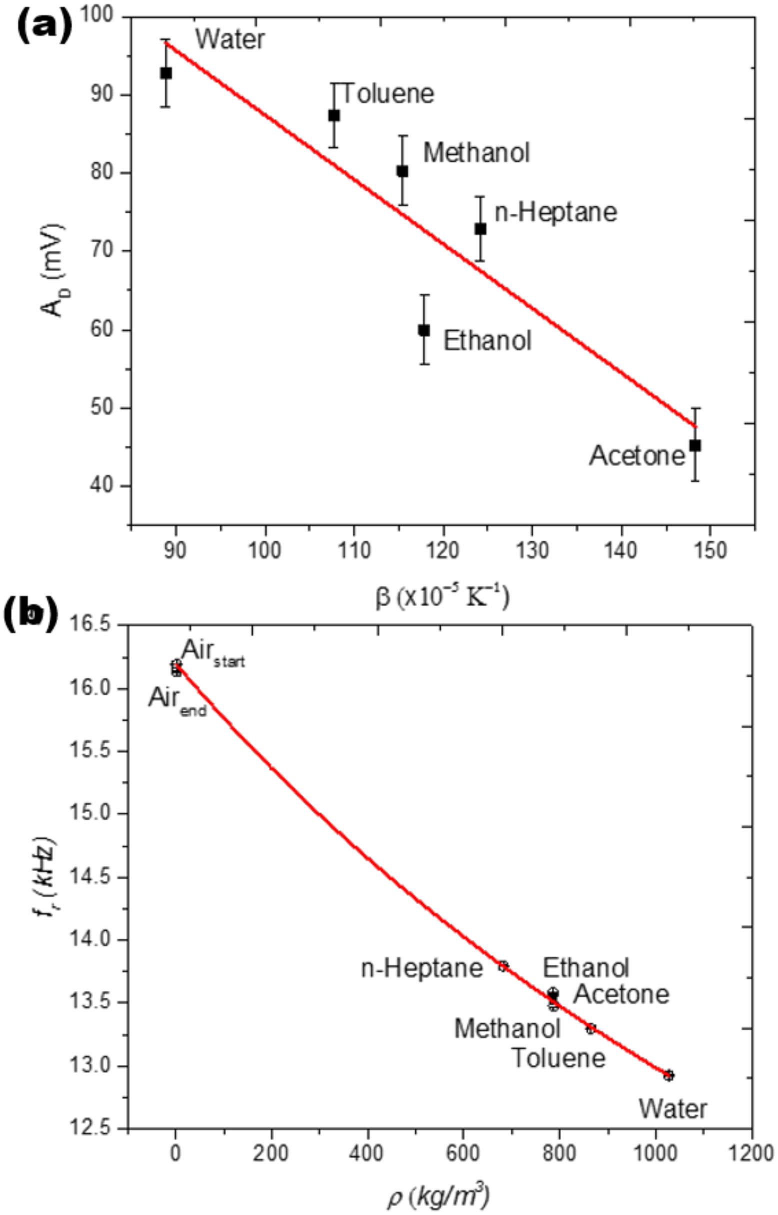

Figure 4.4: (a) Deflection amplitude of the BMC is plotted as a function of the coefficient of volumetric expansion of the individual chemicals. It is to be noted that the liquids that have less volumetric expansion produce less heat loss resulting in maximum deflection amplitude (b) Frequency of the loaded BMC as a function of density of BMC constituents.

average of heat capacity of the solutions, their mass is calculated from a known volume (V) of the microchannel and density (ρ_l) of each solution. Due to fabrication tolerances, the microchannel volume can differ by 6% among different BMCs from the same batch. As the BMC operates in a quasi-static mode, its resonance frequency (fr) is also measured while measuring static deflection. With an air filled BMC, fr is recorded as 16.692±0.02 kHz from twenty measurements. The standard deviation of the resonance frequency (SD fr) of the liquid filled BMC is calculated to be 18 Hz from twenty measurements. The density of the solutions is extracted from the frequency shifts. With mass ratio (mR) ranging from 8.53% (n-heptane) to 10.6% (toluene), the weighted average heat capacity for methanol, ethanol, n-heptane, toluene, and n-butanol are calculated to be 0.24, 0.23, 0.21, 0.18, and 0.2 J/g K, respectively. The average of weighted heat capacity of SiN and Al are calculated to be 0.57 and 0.06 J/g K, respectively. Fig. 4.3(b) shows the relationship between mass-weighted average heat capacity (C_{pm}) of the liquid samples and time constant of the BMC. From the slope, the average sensitivity ($S_C=\tau/C_{pm}$) is calculated to be 30.5 ms g K/J. From the error bars (in time constant) and the slope, average resolution in heat capacity is calculated as 23 mJ/g K.

Fig. 4.4(a) shows a linear trend between the average value of BMC deflection (at saturation) and the volumetric thermal expansion of the liquids. This indicates that there is a high chance exist that liquid is participating in heat intake thus contributing to the heat losses and reduction in total deflection of the cantilever. Fig. 4.4(b) provides an orthogonal measurement of mass density (of the six liquid solutions), which is simultaneously measured with thermal diffusivity. The entire experiment including liquid loading to data acquisition is very fast and takes few minutes ($\approx$ 2 min). As the BMC resonates in the quasi static state, the resonance frequency (f_r) of the cantilever is measured as 16.19 kHz. The density is measured using a shift in resonance frequency (f_r) with the loading of every liquid sample at room temperature in open air using an SR 760 Spectrum analyzer. Before loading ethanol, f_r is recorded as 16.19 kHz. The data is averaged over twenty measurements. Once ethanol is loaded, the f_r drops to 13.56 kHz. After a measurement of each liquid sample, the f_r is measured again to match with original f_r of 16.19 kHz. With n-Heptane inside the BMC, the f_r increases to 13.796 kHz. A shift in f_r is a function of mass density, therefore, can be formulated and plotted to predict the density of an unknown solution. The measurements fit well with a function

$$f_r = 1/2\pi\sqrt{\frac{k}{V_B\rho_B + V_L\rho_L}} \tag{4.1}$$

where k, V_B and ρ_B are spring constant, volume and density of the BMC, respectively while V_L and ρ_L are volume and density if an individual liquid sample inside the BMC, respectively [124]. In the plot, the data on the density of the liquid samples is taken from literature [152]. The data is fit with the aforementioned function which also helps in calculating the sensitivity ($S_\rho = f_r/\rho$) of the BMC as 3.2 kHz/(kg m^{-3}). The frequency resolution can be amplified by reducing the damping conditions and by reducing the noise in the measurement.

In summary, we explore BMC as a platform for not just gravimetric sensing in the presence of liquid but also for many other applications such as spectroscopy of pL volume liquid, thermal transport in liquids and colloidal suspensions, viscosity measurements and density measurements. The advantage of using BMC lies in the low thermal mass of the system that is extremely sensitive to external stimuli such as mass, temperature and energy. This chapter emphasizes the versatility of BMC to provide an on-line and rapid measurement of thermophysical properties of the constituents in the BMC.

4.7 Conclusion

BMC has been systematically tested to integrate with current Lab-on-Chip platforms to provide online, rapid, simultaneous, and inexpensive measurements of density, spectroscopy, and thermo-physical properties of pico liter volume solutions. In the case of photothermal spectroscopy, the localized heat generated is the resultant of IR absorption by the constituents of the BMC. In a similar way piezoresistive heating lines can be fabricated so that the entire system can be used as a microscale calorimeter. The dynamic behavior of BMC under periodic heat pulses gives information regarding the heat generated, heat flow in and out of the BMC through its amplitude and time constant. The time constant is more for heavy BMC systems as more heat capacity takes longer time to reach thermal equilibrium. The BMC with an average sensitivity of 30.5 ms g K/J and a resolution of 23 mJ/g K, the BMC can estimate heat capacity of a sample in a few milliseconds which is three orders of magnitude faster than the earlier reported values in the literature [153]. The BMC also measures density of the liquid with a sensitivity and resolution of 2.8 Hz/kg m^{-3} and 6.4 kg m^{-3} respectively. This chapter emphasizes the versatility of BMC to not just for mass sensing in liquid but also for various other applications as thermo-analytical tool. A proper understanding of the thermomechanics of the BMC system can enable to characterize different polymers [154].

Chapter 5

Dynamic thermomechanical response of nanomechanical string resonator subjected to periodic heating

5.1 Overview

Nanomechanical string resonators gained a great deal of excitement in nanomechanics community due to their exceptionally high Q factors and simplicity in fabrication. In order to impart chemical selectivity to these highly sensitive gravimetric sensors by photothermal methods, one has to explore the thermal behavior of nanomechanical strings. In this chapter, we report the dynamic thermomechanical response of a nanomechanical string subjected to periodic heating by IR radiation. Thermal sensitivity of the strings was studied in detail. An effort was made to develop an analytical model to explain the behavior of strings under periodic IR radiation. The most influential parameters affecting the thermal sensitivity were found. This chapter is in contrast to the previous chapters on BMC in which BMC was studied in static mode (deflection of the cantilever to heat), here changes in the resonance frequency of the string were monitored.

5.2 Introduction

Among all gravimetric sensors, silicon nitride nanostrings are an exciting class of nanomechanical resonators with minuscule mass, high frequency, exceptional for their ultra-high quality factors, easy fabrication process, a string like behavior and amenable to optical readout mechanism [38]. Strings are basically bridge like doubly clamped mechanical structures under extreme tensile stress (in our case 800 MPa). Recently these strings have been reported to have mass sensitivities of the order of zeptogram mass level [34]. In order to identify the molecular nature of the analyte present on the surface of the sensor without adapting surface functionalization methods, we have approached photothermal spectroscopy as an alternative. As photothermal spectroscopy investigates the photo-induced change in the thermal state of the material, the nanomechanical strings here are considered as thermal sensors and explored their thermomechanical behavior. In the advent of using nanomechanical strings, not just for mass sensing but also as thermo-analytical tools [106] for various applications, it is vital to study the device characteristics under external heating and periodic heating. Among all resonators metal coated cantilevers are extensively investigated as excellent thermal sensors but thermal sensitivity in using bimorph behavior of cantilevers limit the miniaturization process and measurements based on static cantilever deflection are prone to thermomechanical noise and external vibrations, thus limiting the sensitivity. On the other hand, the novel design of silicon nitride strings is relatively new and promising to be used as thermal sensors because of high susceptibility of dynamic characteristics of strings to external temperature.

In this chapter, we measure the dynamic thermomechanical response of nanomechanical string resonators to periodic heating by infrared radiation and also measure their response to external heating. The detailed experimental analysis is presented to find out the minimum detectable photon radiation and minimum temperature that can be measured using this new class of thermal sensing platform.

5.3 Methodology

5.3.1 Fabrication of silicon nitride nanomechanical strings

The nanomechanical string work was carried out in collaboration with Dept of Physics, U of A. I hereby acknowledge their support and encouragement throughout the work. Silicon nitride strings are fabricated from stoichiometric silicon nitride deposited onto silicon dioxide on a silicon handle using LPCVD. Typical fabrication includes surface micromachining techniques and optical lithography to fabricate nanostrings of various designs. These wafers are commercially available as a 100 mm wafer (Rogue Valley Microdevices). We perform standard optical lithography on silicon nitride, etch silicon nitride using reactive ion etching, followed by buffered oxide etch of 2 μm thick silicon dioxide layer.

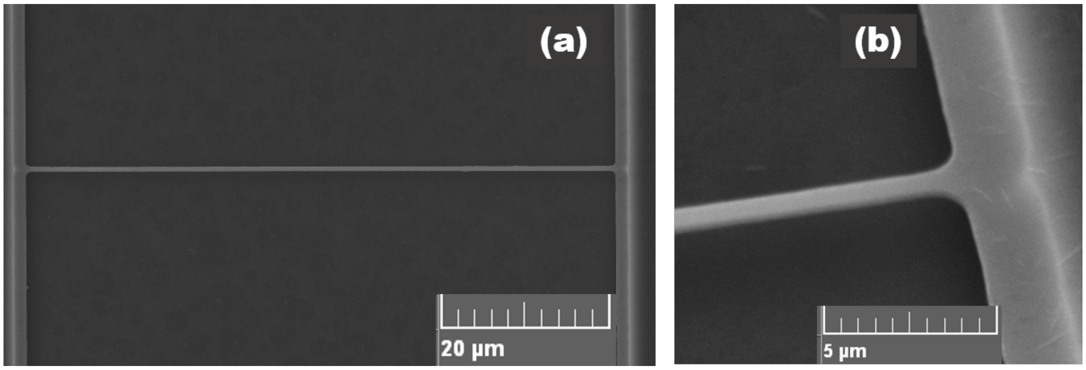

Figure 5.1: (a) Scanning electron micrograph of 50 μm long silicon nitride nanostring. (b) Scanning electron micrograph of silicon nitride at oblique view. The anchor region clearly shows that the nanostring is released perfectly from the substrate.

Detailed fabrication details can be found elsewhere [38].

5.3.2 Measurement set up

The resonance characteristics of fabricated nanomechanical strings are measured using optical interferometry technique using a 632 nm red laser. The fabricated devices are placed on a piezoelectric buzzer to provide mechanical actuation, inside a vacuum chamber with ZnSe optical window to radiate with IR. The vacuum chamber is pumped to a vacuum of $\approx$ 2 X 10^{-7} torr to eliminate any viscous damping. It is verified that the optical power of the red laser does not result in frequency shift due to heating, a consequence of no absorption of silicon nitride in the visible region. Nanostring motion has been measured from the interference of light passing through the nanostring and reflecting from the underlying silicon substrate, and light reflecting off the silicon nitride surface resulting in a voltage signal upon reaching the photodetector. The voltage signals are amplified 25 fold and monitored using a multipurpose HF2LI Zurich instruments lock-in amplifier. The amplified voltage signal reaching the lock-in amplifier can be converted to an absolute displacement via equipartition theorem by a conversion factor. Fitting the power spectral density function to the square of the voltage divided by the measurement bandwidth, we can extract the resonance characteristics such as resonance frequency, Q factor, and the noise floor.

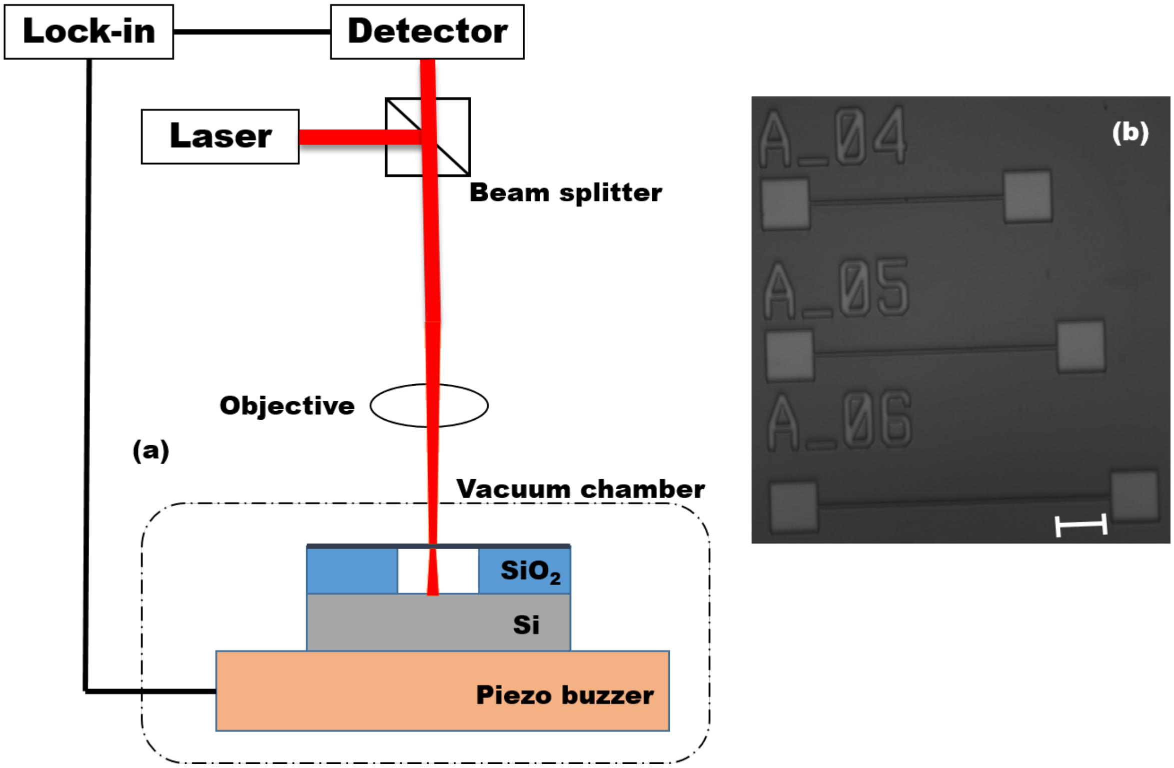

Figure 5.2: (a) Schematic of the optical interference measurement set up. (b) Optical images of a typical chip consisting of many nanostrings. Scale bar is 50 μm.

5.4 Theory

Analytical model for thermal sensitivity of a nanostring

The basic dynamics of string and their temperature dependence have been discussed in sections 2.2 and 2.5.3 respectively. Here we derive an analytical model considering the energy balance equation on an element along the length of the string.

Let's consider a quasi one-dimensional situation, where the string is getting heated because of IR absorption by an incident power P_{inc} distributed evenly across the IR beam diameter (2.5 mm dia), focused at position x_0, while the ends are maintained at ambient temperature $T(0) = T(L) = 298$K. The temporal and spatial evolution of temperature T(x,t), is governed by heat continuity equation across a differential element along the length of the string. Considering a typical heat balance equation

(rate of heat in)+(rate of heat generation)=(rate of heat out)+(rate of heat accumulation)

Assuming the heat transfer is only by conduction (due to vacuum) and the unsteady state heat balance equation in only x direction on the element of control volume with cross-sectional area A and width Δx

$$q_{x/x} + q^{\cdot}(\Delta x.A) = q_{x/x+\Delta x} + \rho c_p \frac{\partial T}{\partial t}(\Delta x.A) \tag{5.1}$$

where $q^{\cdot}$ is the rate of heat generated per unit volume. Considering a case of unsteady state heat conduction equation and rearranging the terms we get

$$\frac{\partial T}{\partial t} = \frac{k}{\rho c_p}\frac{\partial^2 T}{\partial x^2} + \frac{q^{\cdot}}{\rho c_p} \tag{5.2}$$

where k is thermal conductivity, ρ is density, c_p is specific heat and $q^{\cdot}$ is power per unit volume. The IR source we have used is a QCL that has a spot diameter (W) of 2.5 mm. As heat generated in this case is because of IR absorption the absorbed power by the string at a position x_0

$$q_{abs} = q_{inc}\alpha\frac{4A_{str}}{\pi W^2} \tag{5.3}$$

where q_{inc} is the incident power, q_{abs} is the absorbed power over an area of the string A_{str} and α is the IR absorption at radiated IR wavenumber.

Considering the boundary conditions such as the anchor region is kept at room temperature and upon solving the equation 5.4 at the midpoint of the string, the maximum change in temperature occurs at the midpoint of the string where maximum power is dissipated, given as [106]

$$\Delta T = \frac{Lq_{abs}}{8kA} \tag{5.4}$$

Where q_{abs} is the IR power absorbed, L is the length of the string, k is the thermal conductivity of the string material and A is the area of cross section. Note that heat is generated by IR absorption of the string material only.

When the string is subjected to external heating, the string experiences a thermal stress in accordance with coefficient of thermal expansion due to temperature rise and results in a frequency change as [43]

$$f = \frac{n}{2L}\sqrt{\frac{\sigma - E(\alpha_B - \alpha_S)\Delta T}{\rho}} \tag{5.5}$$

Where n is the vibration mode number, σ is the pre stress, E is the Young's modulus of the string material, α_B is the thermal expansion coefficient of the beam (string) material, α_S is the thermal expansion coefficient of the substrate material (Silicon) and ΔT is the temperature rise. The shift in frequency due to heating is dependent on whether the heat is localized or uniformly distributed depending on the relative difference in thermal expansion coefficient of string and support. In case of uniformly heated scenario, the frequency shift can be positive depending on the relative difference in thermal expansion coefficient of string and support. If the support expands more than the string material, it adds additional stress in the string thus increasing the frequency. The relative change in frequency

$$\frac{\Delta f}{f_0} = \frac{f - f_0}{f_0} = -\frac{1}{2}\frac{\Delta\alpha E\Delta T}{\sigma_0} \tag{5.6}$$

Where $\Delta\alpha = \alpha_B - \alpha_S$. Upon substituting equation 5.4 in the above equation, the relative frequency shift for a change in temperature is given by [102]

$$\frac{\Delta f}{f_0} = -\frac{1}{16}\frac{\Delta\alpha EPL}{\sigma_0 kA} \tag{5.7}$$

From the equation 5.7, it is evident that the change in relative frequency is directly proportional to the power of the IR, length of the string and inversely proportional to the area of the string and pre-stress in the string. That means longer strings that are narrower and thinner with less pre-stress are better suited for temperature sensing using

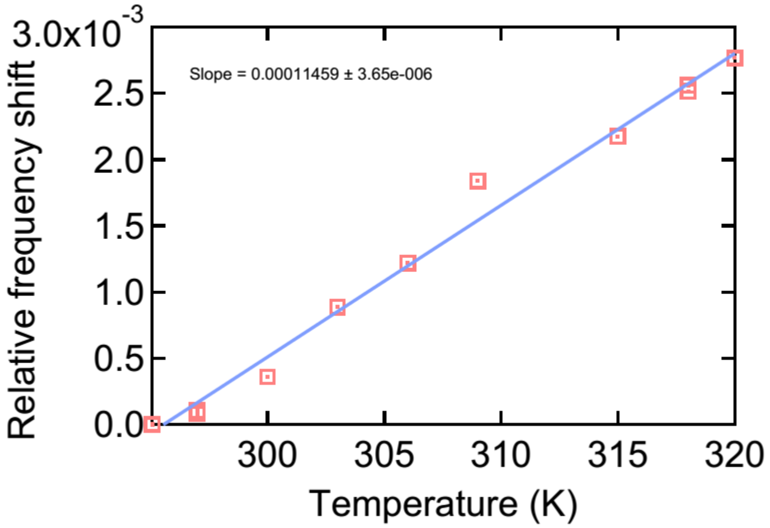

Figure 5.3: Relative frequency shift in the resonance frequency of the string with respect to external temperature. In this configuration, the string is considered to be in a heat bath.

nanomechanical strings. Hence from here on, we consider a relative change in the frequency as a dependent parameter with respect to heat and power. Thus, the thermomechanical sensitivity and power sensitivity of the strings were found.

5.5 Experiments

Measuring thermomechanical sensitivity

The thermal sensitivity of the nanomechanical string was found by subjecting the string to external temperature by placing the whole device on a Peltier element with a heating controller. In this configuration, the string is assumed to be in a heat bath, held in thermal equilibrium at a uniform temperature. The frequency shift upon an increase in temperature depends on the effective thermal stress experienced by the string. For our device, the frequency of the string shifts upwards upon heating, since the substrate expands more than the string material due to high thermal expansion coefficient of the substrate.

Measuring power sensitivity

The power sensitivity of the string was found by subjecting the string resonator to various incident IR powers radiated at the center of the string. We have measured the power sensitivity of the strings at a chosen IR wavenumber of 1220 cm^{-1} where silicon nitride has significant IR absorption. The IR laser from QCL has a repetition rate of 100 kHz at a duty cycle of 5% at maximum drive current. The duty cycle of the laser controls the pulse width at the repetition rate of 100 kHz, deciding the average power output of the laser. Thus, we have recorded the dynamic characteristics of the string resonator at 1220 cm^{-1} IR radiation with respect to different duty cycles. It has been observed that the magnitude of frequency shift depends on the position of the IR laser spot on the string, hence we always maintained the IR spot to be at the center of the string to produce maximum frequency shift. The strings were mechanically actuated by giving very small ($\approx 500\ \mu$V) excitation voltage to the piezo buzzer to determine accurate frequency and phase. The frequency of the string has been monitored using a positive phase lock loop (PLL), locked at the phase of initial frequency. The frequency shifts have been measured at different duty cycles of the IR radiation for a sufficient time till we get equilibrium frequency value under IR radiation. The relative change in frequency of the string is plotted with respect to IR incident power to obtain power sensitivity of the string.

5.5.1 Thermal time constant

Characteristic thermal time constant refers to the time required for the device to respond to change in heat pulses. As the relative change in frequency (Δf/f) of the string is considered as a dependent parameter upon IR irradiation, the time taken by the device to respond to IR in ON and OFF position at an IR wavenumber of maximum power is considered as the thermal time constant of the string. The sampling rate of the frequency tracking using PLL is 7.6 kHz which is not fast enough to keep track of rapid frequency changes in the string upon IR radiation or IR power change. As seen from the Fig. 5.4 every frequency change in the string upon a change in IR power is associated with time for thermal equilibrium. The thermal time constant of a string which is well isolated from the bottom can be calculated as the ratio between thermal capacitance (C) and thermal conductance (G) as [67].

$$\tau = \frac{C}{G} = \frac{A_c l \rho c}{k A_c / l} = \frac{l^2 \rho c}{k} \tag{5.8}$$

where A_c is the cross section area (wh), ρ is the density (ρ_{SiN}= 3050 kg/m^3), c is the specific heat (c_{SiN}= 700 J/Kg.K), l is the length of the string and k is the thermal conductivity (k_{SiN}= 30 W/m.K). For a string of length 300 μm the thermal time constant is $\approx$ 6.4 ms.

5.6 Results and Discussions

5.6.1 Measuring thermal sensitivity

The slope of the curve in Fig. 5.3 indicates the thermal sensitivity of the string. Our experimental system has excellent frequency stability and the frequency variation measured over 15 min lead us to calculate an Allan deviation of 1 X 10^{-8} [155]. For an SNR of 3, with an experimentally measured thermal sensitivity of 1.1 X 10^{-4}K^{-1} (114 ppm/K), we predict to measure a minimum of 0.27 mK. The provided temperature resolution is of the same order as micro temperature sensors [156].

5.6.2 Measuring power sensitivity

The peak power output of the QCL laser at 1220 cm^{-1} at a repetition rate of 100 KHz and a duty cycle of 5% is 350 mW (more details in appendix). The IR laser is focused at the center of the string so that it gives maximum change in frequency. The power of the laser has been continuously changed while PLL keeps tracking the resonance frequency of the string. Initially the IR was in OFF position, then IR was turned ON at its maximum power and the data has been recorded for some time ($\approx$1 min) then IR was turned OFF again and then IR was ON with new output power by changing the duty cycle. The change in frequency upon IR radiation at different average power output (average power = Duty cycle X peak power)was recorded as shown in Fig. 5.4. The average power incident has been mentioned on the top of the frequency data in Fig. 5.4 . The shape of the curve is highly repeatable. At every ON/OFF cycle of IR, the change in frequency comes to thermal equilibrium after some time. Fig. 5.4 (a) shows the change in frequency at different IR power for a string length of 50 μm and Fig. 5.4 (b) for a string length of 300 μm. Fig. 5.4 (a) shows a positive change in frequency of 415 Hz upon IR radiation of incident power 17.5 mW on a 50 μm length string. The inset in the Fig. 5.4 (a) shows the time response of the string to come in thermal equilibrium. Whereas a negative frequency shift of 360 Hz has been observed in a string of length 300 μm for the same incident IR

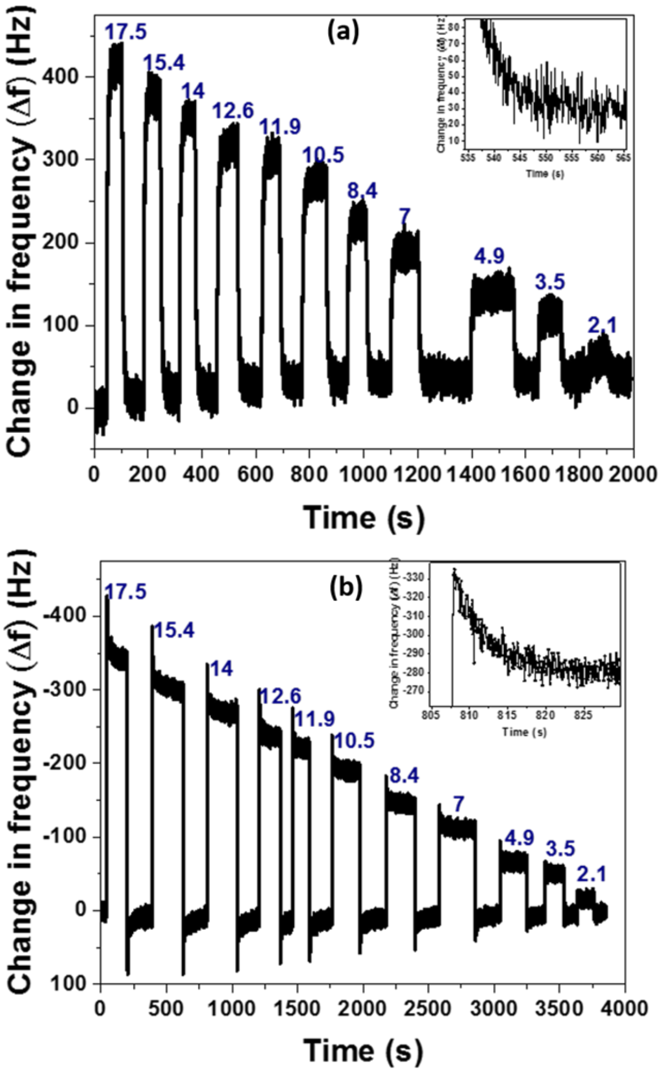

Figure 5.4: Dynamics of change in frequency of the string at different IR incident powers. The PLL is continuously tracking the frequency of the string when subjected to different IR powers. (a) 50 μm long string (b) 300 μm long string. Inset of each figure shows time response for input heat flux. Note that 300 μm long string has negative frequency shift while 50 μm long string has positive frequency.

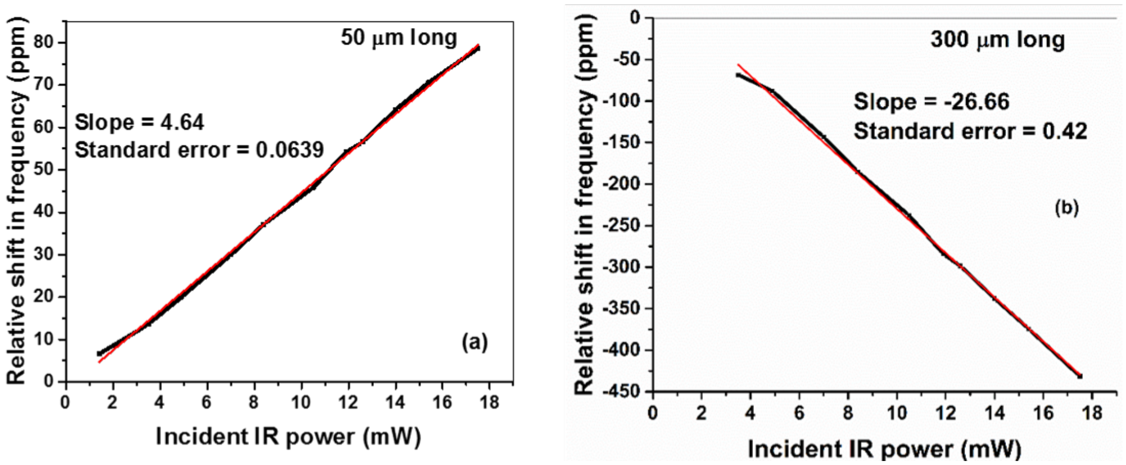

Figure 5.5: Relative shift in frequency as a function of incident IR power (a) 50 μm long string (b) 300 μm long string. Note that the marginal increase in the magnitude of relative frequency shift of 300 μm long string is because of the lower resonance frequency of the string

power as shown in Fig. 5.4 (b). The positive or negative shift in the frequency upon IR radiation is dependent on the proximity of the heat source to the anchor point, thermal stress and device configuration with respect to IR spot or a complex combination of all. It has been observed in our experiments that longer strings always give negative frequency shift as thermal expansion of the string is dominating, to reduce the pre-stress in the string Whereas positive frequency shift is observed in shorter strings in the configuration of string in heat bath or because the underlying silicon is expanding more thus increasing the pre-stress in the string. Note that the 300 μm length string takes more time to come into thermal equilibrium in comparison to 50 μm length string as shown in the insets of Fig. 5.4 which is evident from the equation 5.8.

The relative frequency shift of string is plotted as a function of the incident power of IR as shown in Fig. 5.5. Fig. 5.5 it is evident that the relative frequency shift is linear with IR incident power. The slope of the curve reflects the power sensitivity of the string. It is clear from Fig. 5.5 that longer string has higher power sensitivity than shorter string, even though the change in frequency upon IR radiation of both the strings is of same order. This high variation in relative frequency shift is due to the low resonance frequency of the longer string. Similar experiments were conducted on strings of different lengths and the response of the string is explained using equation 5.7. However, the IR alignment with respect to string geometry causes a complex thermal response from the string resulting in positive and negative frequency shifts. In some cases, we have observed both ways shift in frequency upon IR radiation.

In order to evaluate the performance of the strings to photothermal effects, lets consider an example of 300 μm long string of width 1 μm and thickness 250 nm for calculations. From Fig. 5.5 (b) the relative frequency shift of 300 μm long string was 430 ppm at an incident IR power of 17.5 mW. Considering an IR absorbance of 0.15 for silicon nitride at thickness of 250 nm at 1220 cm^{-1}, the absorbed power by the string can be calculated using equation 3.2. Though the incident power of IR is 17.5 mW, due to poor IR absorbance and small area, the absorbed IR power is only 160 nW. Considering an order of magnitude higher frequency instability during IR radiation due to photoactivation, the Allan deviation is found be of the order of 10^{-7}. For an SNR of 3 and power sensitivity of 26.7 ppm/mW, we predict to measure a minimum of 3.7 μW of incident IR power. Considering the fact that 160 nW of IR power absorbed is producing a relative frequency shift of 430 ppm, with a sensitivity of 3 ppm/nW and an SNR of 3, we can measure a minimum of 35 pW absorbed power. We have previously reported the capability of our experimental set up to measure a minimum mass resolution of $\approx$ attogram (10^{-21} kg). This chapter is emphasized to understand the behavior of nanomechanical strings subjected to heat pulses.

5.7 Conclusion

In summary, a minimum detectable power of $\approx$ 35 pW and an energy resolution of 26 fJ can be easily possible with the capability of attogram mass resolution using nanomechanical strings. By careful modification of the string geometry (longer and narrower strings), it is possible to study the behavior of a single biological entity involving an energy exchange in the order of aJ. This chapter is mainly focused on establishing nanomechanical string resonators as excellent thermal sensors. The low thermal mass, excellent thermal isolation, integration with NEMS and relatively easy fabrication makes nanomechanical strings potential candidates for more versatile applications and as analytical tools to study nanoscale phenomena.

Chapter 6

Photothermal spectroscopy of trace quantities of explosive molecules using nanomechanical strings

6.1 Overview

In this chapter, we demonstrate the molecular identification from trace quantities of analytes on the string surface using photothermal spectroscopy techniques. We have considered 1,3,5-trinitroperhydro-1,3,5-triazine (RDX) as a typical example for this study. As photothermal spectroscopy involves the photo-induced thermal state of the sample, nanomechanical strings are explored as thermal sensors. We have observed thermomechanical frequency detuning at the IR wavelengths where the analyte has maximum IR absorption. This is due to the molecular resonance of the sample which is specific to that molecular configuration (fingerprint of the molecule). The excellent mass sensitivity of nanomechanical strings has been used in RDX sublimation information along with spectroscopy information. As photothermal spectroscopy on silicon nitride strings offers excellent mass sensitivity along with high optical selectivity, this platform has potential for rapid, inexpensive and label-free analysis in real-time applications.

6.2 Introduction

Nanomechanical resonators are used as excellent gravimetric sensors due to their sensitivity in resonance dynamics for very small external perturbations. Rapid advances in the microfabrication technology enable devices that do not only possess minuscule mass but also excellent Q factor and frequency stability. The underlying concept behind these excellent mass sensitivities is the minuscule mass and nanodevices attaining very high resonance quality factors. The two attributes respectively, high mass responsivity and high-frequency stability are the characteristics of miniaturization. Recently extremely high-quality factors have been reported in silicon nitride nanomechanical strings, generating a great deal of interest in nanomechanics community.

Despite these advances, just the mass information of the analyte cannot provide complete information, and, therefore, must be coupled with a complementary technique that gives chemical information such as using a functionalized surface, [157] gas chromatography [158], or photothermal spectroscopy [17, 68, 88, 91]. Achieving chemical signature using functionalized chemo-selective interfaces can only provide partial selectivity due to unspecific and weak nature of chemical bonding and moreover the procedures of functionalization can be cumbersome and may damage the performance of the device [11]. In contrast, photothermal methods are nondestructive and based on the heat produced by the non-radiative decay of the absorbed photons [159]. Every molecule absorbs photons of frequency similar to their molecular vibrations that are specific to a particular configuration providing highly specific chemical identity. For most of the molecules, these molecular vibrations occur in the mid-IR (6 to 10 μm)region. A significant portion of the photon absorption results in a change in the thermal state of the absorbent due to nonradiative decay. Thermal effects associated with the IR absorption by resonant molecular vibrations can provide a signature of the adsorbed molecule. If the molecule is physisorbed on a nanomechanical device, the heat generated due to IR absorption can affect the resonance characteristics of the resonator [104]. In this configuration, the nanomechanical device functions as a thermal sensor. Silicon nitride nanomechanical strings are recently explored for temperature measurement [43] and optomechanics [106].

In order to achieve this feat, one need to have a nanomechanical resonator that has excellent mass sensitivity and thermal sensitivity. Miniaturization can provide low mass resonators, but they suffer from poor Q factors and frequency instabilities. In such scenario, silicon nitride nano-strings have amused everybody in the nanomechanical community with low mass and extremely high Q factors. Nanostrings are miniaturized doubly clamped beams with high internal tensile stress [160]. Alon with a string like behavior, the pre-stress (here $\sigma = 0.8$ GPa) in the beam results in excellent frequency stability and exceptionally high Q factors [160, 161]. Along with inexpensive fabrication, the high Q factors allow easy observation of thermomechanical motion without complex actuation and electronic locking schemes. The thermal sensitivity of the string material, mismatch between the silicon nitride strings and the silicon substrate for a temperature gradient and a complex behavior of all provides the basis for thermal stress in the string [105].

6.3 Objective

The objective of this chapter is to explore nanomechanical string as a thermal sensor and demonstrate chemical identification using photothermal methods. Currently, nanomechanical strings are at their best interest as excellent mass sensors but possess huge potential for thermal and energy sensing due to the built-in tensile stress. This chapter emphasizes not just on chemical identification but on optimization of parameters to find the chemical identity from the minimum physisorbed mass. Here we demonstrate the chemical identification of femtogram level ($\approx$ 42 fg) physisorbed mass using photothermal methods. RDX has been used as a prototypical molecule for the detection. RDX has been physisorbed onto the nanomechanical string using indigenously made thermal evaporation.

6.4 Experiments

6.4.1 Fabrication of SiN nanomechanical strings

Nanomechanical strings were fabricated by Tushar Biswas from Prof John Davis group. The nanomechanical string work was carried out in collaboration with Dept of Physics, U of A. I hereby acknowledge their support and encouragement throughout the work. Silicon nitride strings are fabricated from stoichiometric silicon nitride deposited on to silicon dioxide on a silicon handle using LPCVD. We employed inexpensive and simple fabrication procedure such as surface micromachining and optical lithography to fabricate nanstrings of various designs. These wafers are commercially available for \$50 for a 100 mm wafer (Rogue Valley Microdevices). We perform standard optical lithography on silicon nitride, etch silicon nitride using reactive ion etching, followed by buffered oxide etch of 2 μm thick silicon dioxide layer. Detailed fabrication details can be found elsewhere [38].

6.4.2 RDX evaporation

Controlled amount of RDX was deposited on the strings using a home-made thermal evaporation set up. RDX explosive samples were purchased from AccuStandard, Inc. (New

Haven, CA) and used without further purification. As indicated by the manufacturer, the standard concentration of each explosive is 1 mg/ml. The experimental setup consists of a small aluminum vessel surrounded by a programmable heating tape, with two inlets one for the gas flow and another slot for temperature measurement. As a first step, the aluminum chamber was cleaned with ethanol and a small amount of glass wool was kept so that the RDX is spread out and evaporate easily. The entire assembly is wrapped in a heating tape and heated at 50 ^{o}C for 5 min to evaporate any moisture. A sample of 100 μl RDX of concentration 1 mg/ml was taken and dropped onto the previously heated glass wool. The entire assembly is heated to 50 ^{o}C for 3 min and ramped to the target temperature(T_g). Once the thermocouple reading reached the target temperature another 100 μl of RDX sample was dropped and waited till it reach a stable temperature (around 3 min). After reaching to an appropriate temperature, a certain sccm (200 sccm) of N_2 flow has been purged as a carrier gas to take RDX vapors along and get deposited on the sample that is arranged just above the aluminum chamber in its closest proximity as shown in Fig. 6.1. The deposition is continued for desired time at ambient pressure and the substrate is taken off after the time of deposition. In the case of preferential deposition at a particular location, we have used shadow masks made of aluminum with a minimum opening of 2μm × 2μm. This technique mimics in-the-field thermal vaporization of a swab containing trace explosive residue.

The morphology and distribution of RDX deposition mainly depends on the temperature, time and gas flow at the time of deposition. We have optimized all these parameters to have controlled RDX deposition at desired locations. Thorough optimization revealed that the evaporated RDX condenses on the substrate in the form of microcrystallites. We have also observed that oxide and nitride surfaces favor the formation of RDX rods than microcrystallites whereas deposition under similar conditions on gold surface forms microcrystallites. Care should be taken so that the RDX is not deposited beneath the string thus pinning its motion and also to the fact that string should not be overloaded with too much RDX. Keeping all the constraints in consideration, we have optimized the parameters for decent RDX physical adsorption to be 100 ^{o}C as the target temperature, aided by 200 sccm of N_2 flow on SiN surface for 3 to 6 minutes.

6.4.3 Measurement using Interference

After the deposition and characterization of the physisorbed RDX on the string, the sample is loaded into a vacuum chamber having a ZnSe window for IR transparency. The

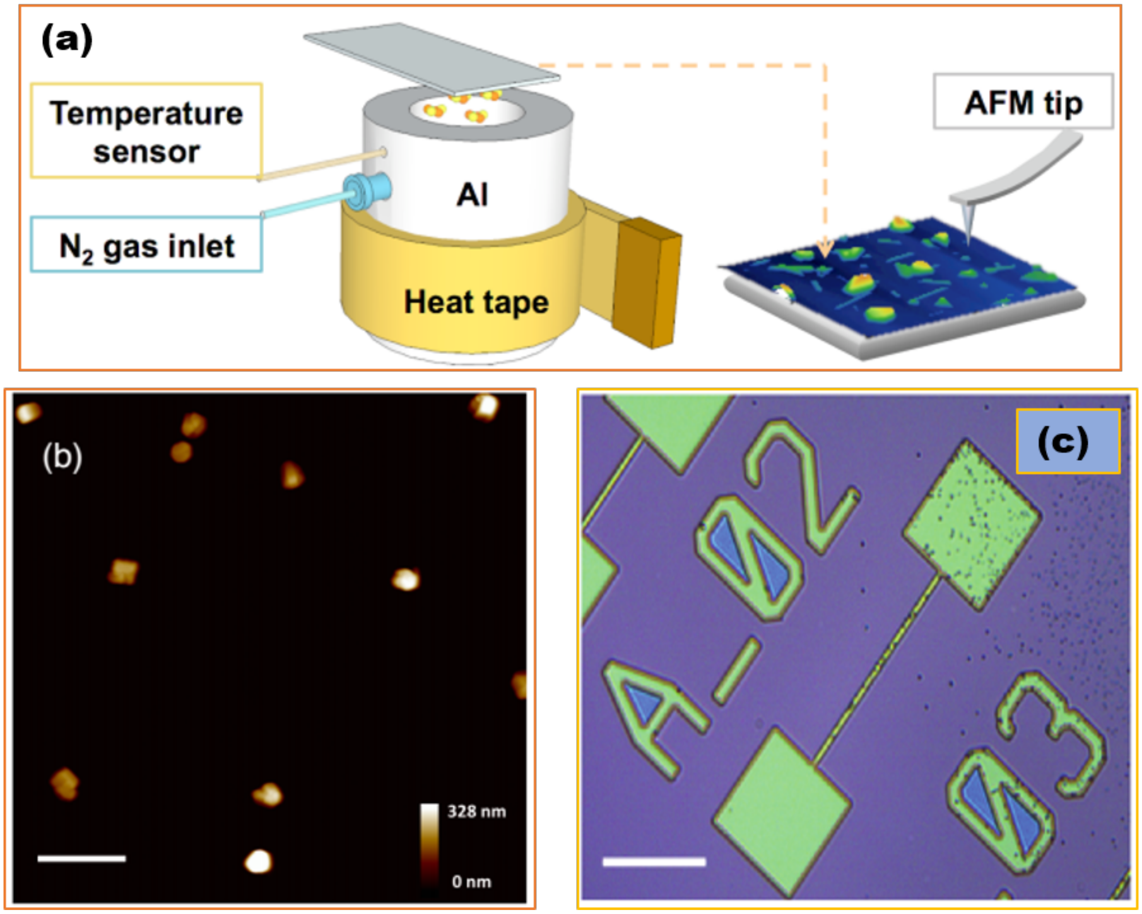

Figure 6.1: (a) Schematic representation of indigenous RDX deposition set up. (b) AFM topography of RDX crystallites on bare silicon nitride surface at optimized parameters. Scale bar is 1.5μm. [102](c)Optical image of a 100μm long silicon nitride nanostring with RDX on the surface [102]. Note that RDX crystallites have high affinity to deposit on silicon nitride surface (green) as compared with the underlying silicon surface (purple). Scale bar is 50μm.

resonance characteristics of the string were measured by optical interference. Optical interferometry caused by a 632 nm red laser reflecting off the nanostring and light passing through the nanostring and reflecting off the silicon substrate [19]. We have observed a decrease in the intensity of the red laser reflecting off of the silicon surface because of ZnSe window, but nevertheless the resonance characteristics are stable and reproducible. A tunable pulsed quantum cascade laser [162] from Daylight Solutions (pulsed Über) operated at a repetition rate is 100 kHz and pulse width of 500 ns has been chosen as IR source. Note that the IR power incident on the string varies with respect to IR wavenumber. To eliminate the viscous damping [160] and to make the RDX stay on the surface of the string [98], the chamber is pumped to a moderate vacuum ($\sim 10^{-4}$ torr). It has been verified that the power of the probing laser has no significant effect on the resonance characteristics of the nanostring. The interferometric signal is amplified 25 fold and analyzed using a high-frequency lock-in amplifier (Zurich instruments HF2LI). The amplified voltage signal reaching the lock-in amplifier can be converted to an absolute displacement via equipartition theorem by a conversion factor. Fitting the power spectral density function to the square of the voltage divided by the measurement bandwidth, we can extract the resonance characteristics such as resonance frequency, Q factor, and the noise floor.

The thermomechanical time-domain data has been captured for one second at each IR wavenumber stepped through its range at 1 cm^{-1} intervals. The obtained signals are then Fourier transformed automated peak fitting was done to obtain power spectral density and resonance characteristics. This method has been used to track the frequency of the string while IR radiation and while background data acquisition without IR. The frequency detuning of nanostring is plotted against the IR wavelength as shown in Fig. 6.2. It is evident from the Fig. 6.2 that the frequency shift is dominant where the sample absorbs IR radiation. The heat produced by the non-radiative decay detunes the frequency of the nanostring in order to reduce the tension in the string. The sudden drops in the frequency shift as shown in Fig. 6.2 (c) are a typical representation of IR absorption due to the molecular resonance of the adsorbates.

Before RDX deposition, the background spectrum of the silicon nitride substrate was taken as shown in Figure 6.2 (b), similar data can also be acquired after the entire RDX has been pumped off. The bare silicon nitride spectrum shows a broad peak after 1220 cm^{-1} due to IR absorption from the defects and Si-N bond vibrations [105]. It is to be noted that the power of IR laser also varies with wave number. Fig. 6.2 (a) shows the frequency response of RDX deposited nanostring with respect to IR wavelength. Two striking features can be observed from Fig. 6.2 (a), such as background slope and frequency

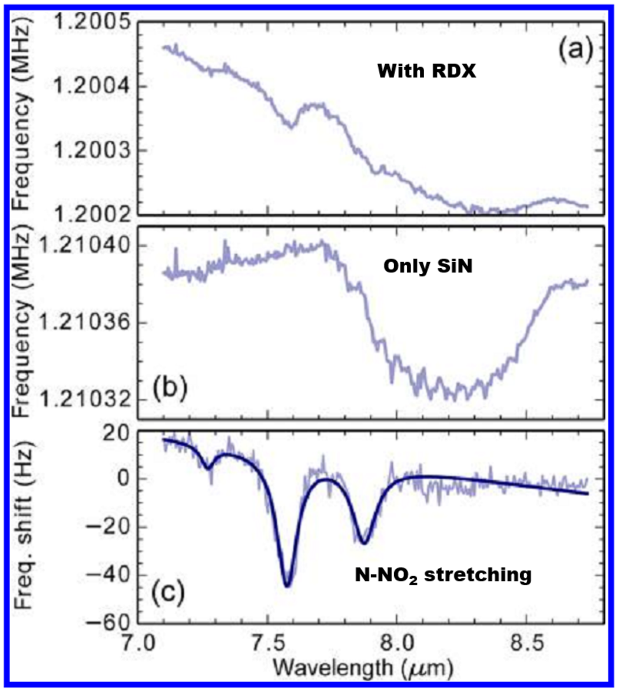

Figure 6.2: Frequency shift of silicon nitride string as a function of incident IR wavelength. a) For the first mode with ≈ 2.72 pg RDX on the string. (b) The frequency detuning of bare silicon nitride (background) as a function of IR wavelength. (c) Nanomechanical photothermal IR spectrum (light blue in color) of RDX after background subtraction. Multipeak Lorentzian fit to the data has been represented as the dark blue curve. Note that the data presented is for silicon nitride string of length 215 μm. [102]

drop at 1220 cm^{-1} and 1320 cm^{-1} wavenumbers. The background slope in Fig. 6.2 (a) is an indication that the mass of the RDX on the string is continuously changing. This desorption of RDX might be due to vacuuming process. To eliminate this effect we have taken background data (without IR) after every IR scan data and subtracted the background from the sample data. The frequency change due to the mass desorption allows us to calculate the mass of RDX on the string using the following formula.

$$\delta m_{\text{eff}} = 2m_{\text{eff}}(\delta f/f) \tag{6.1}$$

whereas m_{eff} is the effective mass of the mechanical resonator, which depends on the mode shape [9]. It is to be noted that in the case of string the effective mass is simply one-half the geometric mass [9]. The mass calculated is the average mass in the data set to incorporate mass variation during sublimation of RDX.

Initially, the frequency shift with IR ON was taken from the RDX deposited string. Next the IR was set to OFF to take the mass desorption data of RDX from the string. Finally (can be taken before RDX deposition) the bare silicon nitride background data has been taken. After subtraction of the continuous desorption signals and silicon nitride background data from data with RDX and IR on data, the frequency shift as a function of IR wavelength reveals molecular signature from the adsorbed RDX sample as shown in 6.2(c). Three principal RDX peaks are seen in 6.2(c) representing the molecular confirmations of N-NO$_2$ bonds in RDX [163]. As photothermal spectroscopy is the photo-induced thermal state of the sample, the string is subjected to localized heating at the RDX locations. The temperature dependency to lower the built-in stress in the string makes them extremely sensitive to heat [105]. We have considered Lorentzian fitting to extract the molecular resonance peaks of the adsorbed RDX shown as the smooth dark blue curve in Fig. 6.2 (c). We have smoothed the data in order to get the best fitting. Hence, as described above we could measure mass desorption as well as spectroscopy signals simultaneously.

6.5 Results and Discussions

The entire data acquisition for one complete IR scan takes only 16 minutes eight for the wavelength scan and eight for the background control scan. Note that there is a slight mass desorption of RDX due to the continuous vacuum process involved. Since the sublimation of the RDX is a slow process, we can still perform the measurements of frequency shift, taking background data after every IR wavelength scan data. Fig. 6.3 shows a series of

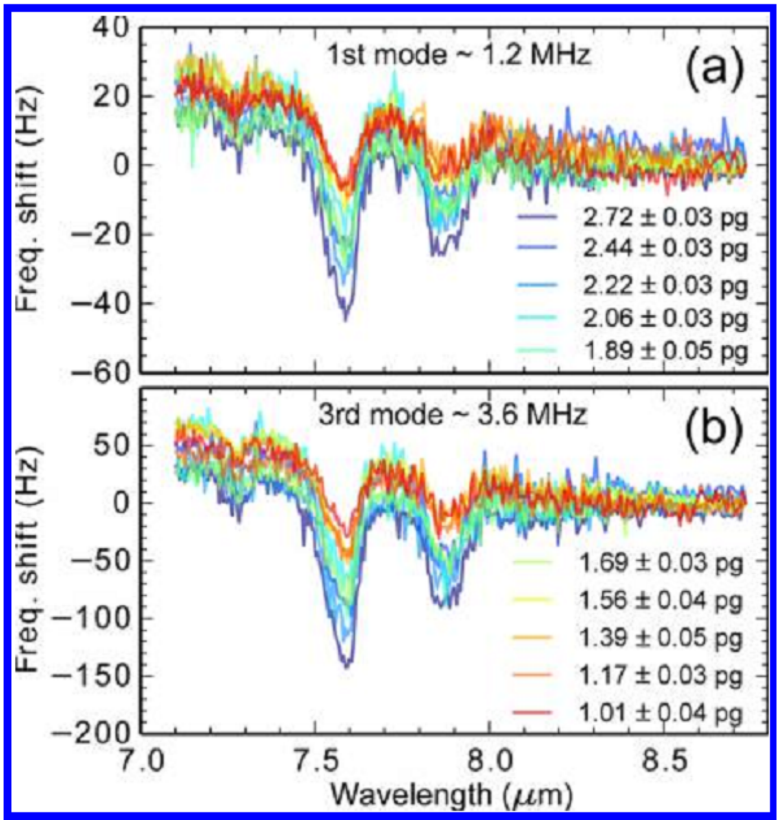

Figure 6.3: Frequency shift as a function of IR wavelength scan from the physisorbed RDX on the string (a) for the first mode and (b) for the thrid mode. The data presented in the figure is obtained from the 215 μm long string. [102]

these photothermal spectroscopy scans as a function of RDX on the nanostring. For every IR scan data presented in the Fig. 6.3, a background data has been subtracted to obtain the IR spectrum. As evident from the Fig. 6.3, the intensity of molecular vibrational peaks are decreasing gradually as RDX has been sublimating. The least molecular identification is from 1.05 pg of RDX in the presented Fig. 6.3.

The photothermal spectroscopy was performed on strings of various lengths and we found that the relative frequency shift is a function of string length and IR power. However, the magnitude of the photothermal frequency shift does not depend on nanostring length, since the power adsorbed by a vibrational mode is [105]

$$P = \delta f \frac{32\kappa A\sqrt{\sigma\rho}}{n\alpha E}. \tag{6.2}$$

Here ρ is the density, σ is the tensile stress, E is the Young's modulus, α is the thermal expansion coefficient, and κ is the thermal conductivity - all of silicon nitride - using previously reported values [38]. δf is the observed frequency shift, A is the cross-sectional area of the nanostring, and n is the mode number. As seen from Fig. 6.3, a higher magnitude in the frequency shift is observed in the third mode relative to the first mode. As the heat developed due to IR absorption solely depends on the mass of the adsorbed RDX, our photothermal signal to noise ratio does not depend on mode number.

In order to explore the ultimate limits of photothermal spectroscopy using silicon nitride nanostrings, we performed a similar set of experiments with controlled RDX mass adsorption. This time, we have started with very small deposition times such as 100 °C for 4 minutes only using a shadow mask. As can be seen in Fig. 6.4 (a), we have started with an initial mass of RDX of 224±4 fg deposited on 175 μm long nanostring. Note that the three clear spectroscopy peaks can be observed even with this small amount of RDX on the string using an automatic multi Lorentzian fitting. As the RDX mass is continuously sublimating, we successively lost each molecular conformational vibrations such as at 125 ±4 fg on the nanostring, we have lost most of the signal at 7.2 μm from and at the lowest masses of 76±3 and 42±2 fg, we are only able to clearly resolve one peak - that is the peak at 7.55 μm which is the strong peak for nitro functional groups of β-phase RDX [163]. The measurements of Allan deviation with the current set enable a minimum of 1.8 ag mass resolution [155].

The absorbed power that is causing the frequency detuning of the string can be calculated using the equation 6.2. Fig. 6.5 shows the power absorbed as a function of the mass of RDX on the string. As seen from the Fig. 6.5, a linear trend can be observed indicating the fact that higher mass of RDX absorbs higher IR energy. Similar data has been presented for strings of varying length reflecting not a great dependency of power absorbed on the length of the string. The differences in the IR power absorbed are attributed to the difference in the cross-sectional area of the strings. It can be deduced from the equation that better frequency shifts are obtained by optimizing the cross-sectional area of the string. This can be accomplished by using thinner silicon nitride (here we use 250 nm thick silicon nitride [19]) and smaller width of the string using EBL. The width and thickness should be optimized in such a way to measure the frequency using optical interference and have a decent frequency stability. The other readout mechanisms can be possible to integrate such as electrical [52, 164, 165] or opto-mechanical [166–170]readout, to measure such nanostrings

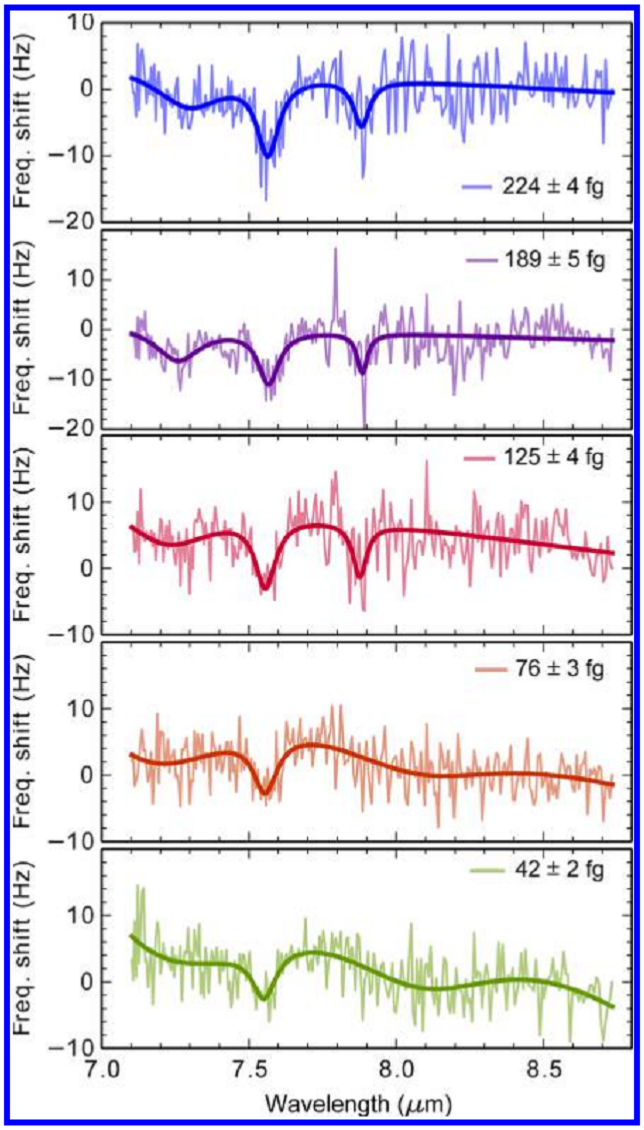

Figure 6.4: Frequency shift as a function of IR wavelength from a 175 μm long string after RDX deposition. An automatic multipeak Lorentzian fit has been performed to reveal molecular identification from adsorbed RDX. As can be seen from the figure the peak intensity decreases with respect to the mass of RDX on the string. Only the main peak of 7.55 μm can still be seen at the lowest RDX levels of 76±3 and 42±2 fg. [102]

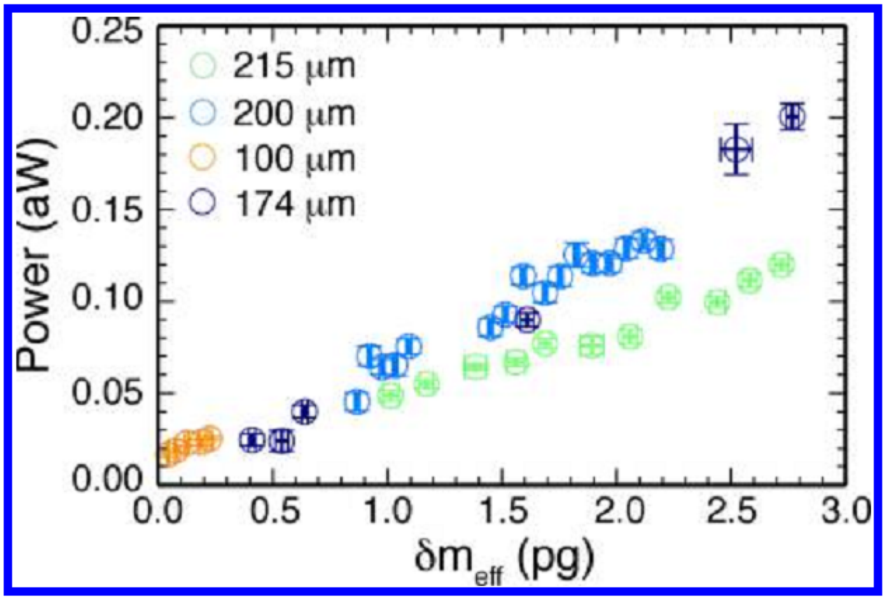

Figure 6.5: Absorbed power as a function of RDX mass on the string at 7.55 μm. Different lengths of the string are presented in the figure with different initial amounts of RDX deposited. A linear trend is observed indicating that higher mass of RDX absorbs higher IR power. Small differences observed might be due to vary cross-sectional areas of the strings. Lorentzian fit has been performed in calculating the error bars in power, and error bars in mass are the standard deviation in data acquisition [102].

6.6 Conclusions

In conclusion, we have demonstrated the molecular identification from ≈ 42 femtogram (120×10^6 molecules) RDX that is physisorbed on the resonator surface. The detection mechanism presented is performed by tracking the thermomechanical motion of the nanomechanical string with and without IR irradiation. IR irradiation provides the molecular spectrum of the molecule via frequency detuning. This chapter emphasizes the underlying concept that nanostrings are extremely sensitive to temperature changes and can be used as an analytical tool in understanding the thermomechanical properties at femtogram level mass. As photothermal techniques are highly selective in the molecular vibrations differentiation is possible even in complex mixtures without overtones [11]. The demonstrated work clearly indicates how to obtain chemical selectivity from the highly sensitive gravimetric sensors such as nanomechanical strings.

Chapter 7

Photo effects on bismuth ferrite nanostructures

7.1 Overview

The motivation to study the photo effects on bismuth ferrite, $BiFeO_3$ (BFO) nanostructures actually arises from the fact that we would like to combine the mass sensitivity of low thermal mass structures (NEMS resonators) and thermally active nature of BFO material (for photothermal selectivity). In the process, we found the very interesting behavior of BFO nanostructures under visible light. This chapter is focused on investigating the properties and behavior of BFO under visible light. Along with multiferroic properties, BFO has anomalous and interesting photo properties due to its narrow band gap and semiconducting nature. The anomalous photo behavior and enhanced visible light absorption are attributed to the presence of surface states. The effect of surface states is more pronounced in high surface area structures such as nanotubes (NTs) and nanowires (NWs). Effect of surface states especially due to oxygen vacancies is studied in detail and enhanced visible light absorption is put into use to demonstrate excellent photocatalytic activity of BFO NTs than BFO nanoparticles (NPs).

7.2 Introduction

BFO is a well known multiferroic material of the perovskite family that exhibits room temperature ferroelectric and magnetic properties [171–174]. In addition to the magnetoelectric properties, recently BFO has attracted considerable attention in optoelectronic applications due to its small band gap ≈ 2.5 eV and semiconducting nature [107, 108]. Many exciting and anomalous optical properties are observed in bulk and thin films of BFO such as light-induced size changes [175], abnormal photovoltaic effect [176], persistent photoconductivity [112] and switchable diode effects [113], paving the way for a plethora of optoelectronic applications. It has been reported that the multiferroic and electrical properties of BFO are extremely sensitive to defects such as secondary phases, vacancies, and interstitials [109,110]. Though, these defects are insignificant and detrimental in bulk, they have profound importance in altering the properties at the nanoscale because of the large surface area [111, 172, 177]. However with the development of various procedures to synthesize BFO nanostructures in various forms such as NPs, NTs, nanocubes (NCs), nanofibers (NFs)and NWs, there has been a resurging interest in exploring properties of BFO at the nanoscale because of the high surface-to-volume ratio and size effects [178,179]. Though one-dimensional (1D) nanostructures of BFO such NTs, NWs, and NFs have been demonstrated to show excellent multiferroic [180,181] and optical [182,183] properties due to their high surface-to-volume ratio, not many researchers have investigated the role of defects on optical properties. It has been also reported that defects such as oxygen vacancies are the main reasons for anomalous optoelectronic properties in oxide nanostructures [184].

On the other hand, an exciting research is in progress to develop non-titania based photocatalyst due to UV limited photoactivity of TiO_2 and poor photostability of doped TiO_2 [185]. In this scenario, semiconducting nature of BFO resurged the interest as a potential photocatalyst candidate due to significant visible light absorption, strong photostability and easy magnetic separation [108,178]. Recent reports suggest BFO nanostructures as a promising material for visible light photocatalyst for water splitting and degradation of organic contaminants [186]. Gao et al have reported visible light photoabsorption in BFO NWs suggesting BFO as a potential photocatalyst [108]. Recent studies on BFO NPs such as photocatalyst for solar hydrogen generation from water [187], degradation of organic pollutants, use as a reusable Fenton-like catalyst [188] and core-shell BFO/TiO_2 nanocomposites for photocatalysis [189] have been reported. Y Huo et al have reported enhanced visible light photocatalysis in mesoporous hollow BFO spheres due to enhanced surface area and increased light absorption [190]. S Li et al have reported better photocatalytic activity in sub microcubes of BFO than microspheres and microcubes [178]. Remarkably enhanced photocatalytic activity has been observed recently, using gold decorated BFO NWs, as gold can act as electron trapping thereby enhancing charge transfer efficiency [183]. Photoexcited carrier transport is a limiting factor in any photocatalytic process, which is strongly influenced by the continuity of the individual nanoarchitecture without scattering. Thus one-dimensional (1-D) materials are widely investigated for higher photo-efficiency [191]. Among all 1-D nanostructures, hollow NTs offer other advantages such as high interface area and quantum size effects arising from ultra-thin wall structure that facilitates superior carrier diffusion and transport. Though BFO NTs have been reported to have high photoabsorption [192], to the best of our knowledge, visible light photocatalytic activity in BFO NTs have not been reported yet.

In this chapter, we emphasize on the role of surface states especially due to oxygen vacancies on anomalous photoluminescence (PL) and photoabsorption. After the detailed analysis of the effect of surface states, we continued to demonstrate the application of enhanced visible light photocatalytic activity of ultra-thin wall BFO NTs.

7.3 Experiments

7.3.1 Synthesis and Characterization of BFO nanotubes (BFO NTs)

Sol-gel template method has been used conventionally to synthesize nanostructures of metal, metal oxides [193], semiconducting oxides [194], dielectric nanostructures [195] and core-shell [196] type of nanostructures. Here, BFO NTs were prepared using a simple sol-gel template method. Porous anodized aluminum oxide (AAO) (Whatman Anodisc^R) with regular and straight pores of diameter 200 nm was selected as the template. BFO solution (sol) was prepared by mixing bismuth nitrate (Bi $(NO_3)_3.5H_2O$) and ferric nitrate ($Fe(NO_3)_3.9H_2O$) in a molar ratio of 1.05:1 in 2-methoxyethanol. The resulting mixture was stirred at 80^{o}C for 1 hr to evaporate the solvent, after which a reddish sol was recovered. The pre-cleaned AAO template was soaked in the BFO sol solution for 30 min. The sol particles cover the inner wall of the porous nanotube template thus forming a thin wall at the pore interface. The resultant sol covered AAO templates were heated at 100^{0}C for 1 hr in vacuum followed by heating in a furnace at 450^{0}C for an hour to remove any organic matter left. The same template was later annealed at 600 oC for an hour in air. The process of annealing converts the sol particles at the inner wall of the porous nanotube into a gel and further annealing process forms BFO. Thus formed BFO NTs were released by etching the template in 6M NaOH for 5 hrs. The highly basic nature of NaOH dissolves the framework of AAO leaving the BFO NTs aside [192,197,198]. The resultant solution was washed many times and centrifuged to separate BFO NTs. Care should be taken while centrifuging so that the nanotubes are not broken. The precipitate consisting of BFO NTs wass dried and examined for material characterization. The density of the nanotubes formed depends on the efficiency of sol particles filling the pore space of the template. Hence various methods exist to fill the nanopores with sol particles such as vacuum assisted sol filling [199], time-dependent template soaking in sol solution [200], concentration-dependent template filling [194, 201] etc.

7.3.2 Characterization

X-Ray Diffraction (XRD)

The phase purity and crystallinity of the samples were characterized by X-ray diffraction on a Rigaku X-ray diffractometer using Cu Kα radiation (λ=1.546A^0). Fig. 7.1 shows the XRD spectrum of BFO NTs. All the diffracted peaks are indexed according to JCPDS file number 01-071-2494, indicating that the BFO NTs obtained are of distorted rhombohedral perovskite structure belonging to the space group of R$_3$C and are polycrystalline in nature. Some unavoidable impurity peaks could be present (a minor impurity peak can be observed represented as the star in Fig. 7.1)and the obtained BFO NTs are single phase polycrystalline in nature. Secondary phases such as Bi_2O_3 may appear sometimes, that can be leached away using nitric acid.

Electron Microscopy Imaging

The morphology of the NTs was investigated using scanning electron microscopy (SEM) and transmission electron microscopy (TEM). A small sample of dilute aqueous solution containing BFO NTs was drop cast on to a clean silicon wafer. This wafer was used for further SEM imaging. Fig.7.2(a) shows SEM images of the BFO NTs revealing that the NTs are hollow in nature with an outer diameter in the range of 230 nm and lengths vary between 5 to 20 μm. SEM images were taken in secondary electron detector mode. 5 μl of extremely dilute BFO NTs aqueous solution was drop cast on to a carbon TEM grid and subjected to TEM imaging. Fig.7.2(b) illustrates TEM images of the surface smooth NTs with wall thicknesses of 20 nm. The diameters shown are consistent with measurements from the SEM data. Selected area electron diffraction (SAED) data in the inset indicates the continuous ring pattern, which suggests the polycrystallinity of the BFO NTs.

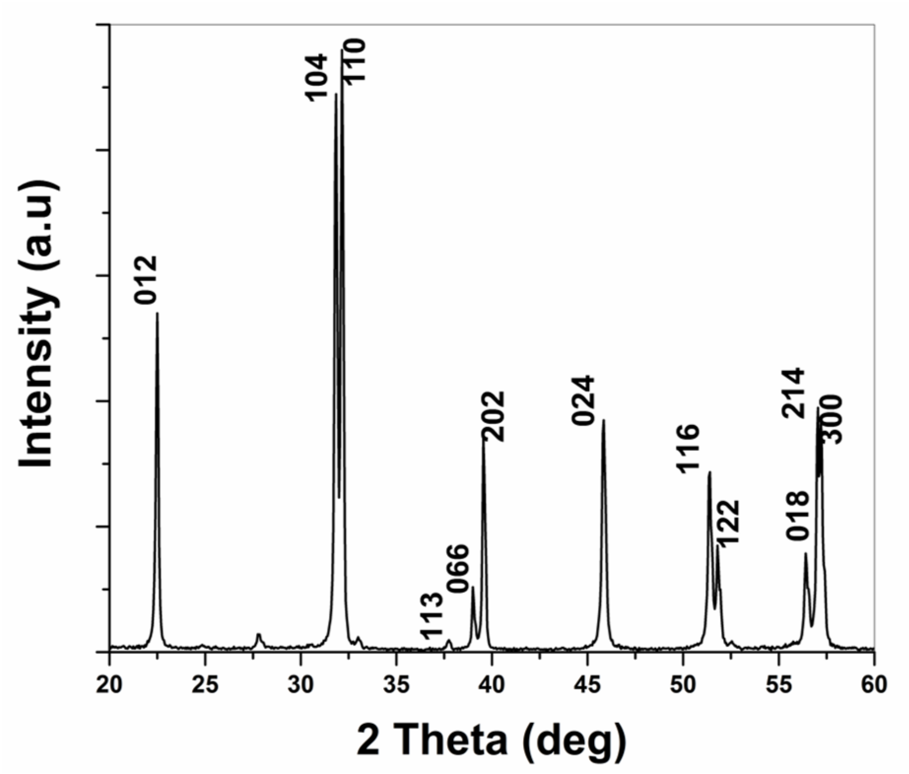

Figure 7.1: XRD spectra of polycrystalline BFO NTs

Energy-dispersive X-ray spectroscopy(EDS)

Identification of elements and their relative proportions was investigated using EDS in the as-synthesized BFO NTs. Figure 7.3 show expected signals from Bi, Fe and O arising from NTs. We do observe some Al counts due to residue from the template and Si, Au signals as the nanotubes were dispersed on a gold sputtered Si wafer. The EDS analysis confirms that the chemical composition of as-synthesized BFO NTs and the ratio of Bi to Fe are found to be 1.3 to 1

X-ray photoelectron spectroscopy(XPS)

X-ray photoelectron spectroscopy (XPS) studies were conducted using a Kratos Axis 165 photoelectron spectrometer in order to investigate the oxidation states of Bi and Fe in BFO NTs. The high-resolution XPS core spectra of Bi 4f and Fe 2p for the BFO NTs are shown in Fig. 7.4 (a) and in Fig. 7.4(b) respectively. As shown in Fig. 7.4 (a), the peaks at 158.6 eV and 163.9 eV correspond to the binding energy of Bi $4f_{7/2}$ and $4f_{5/2}$ of Bi^{+3} state respectively. It is important to note that, even though Bi exists in a +3 state

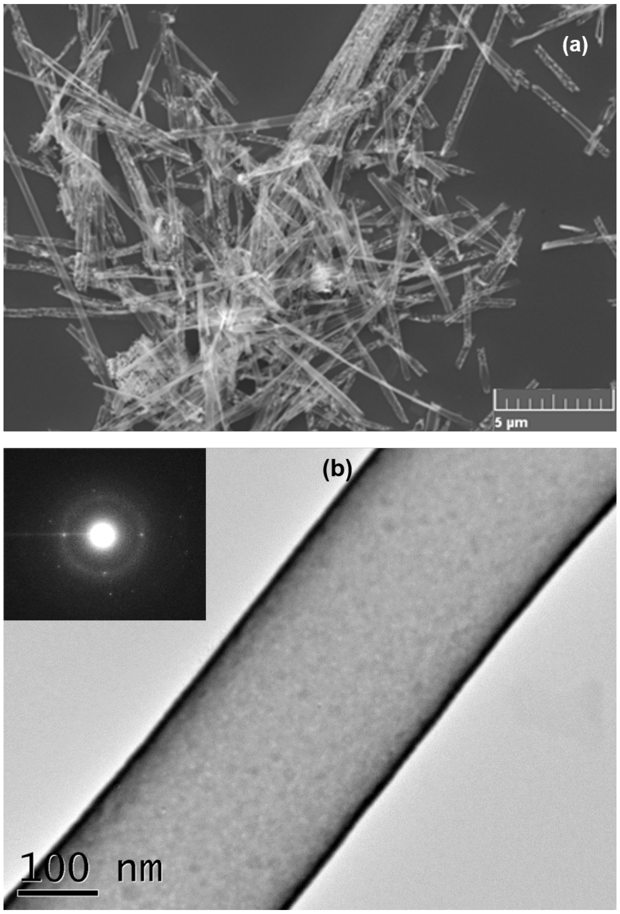

Figure 7.2: (a) SEM image of BFO NTs prepared by sol-gel template method. (b) TEM image of hollow NTs showing wall thickness ≈ 20 nm and diameter ≈ 250 nm. Inset shows SAED pattern.

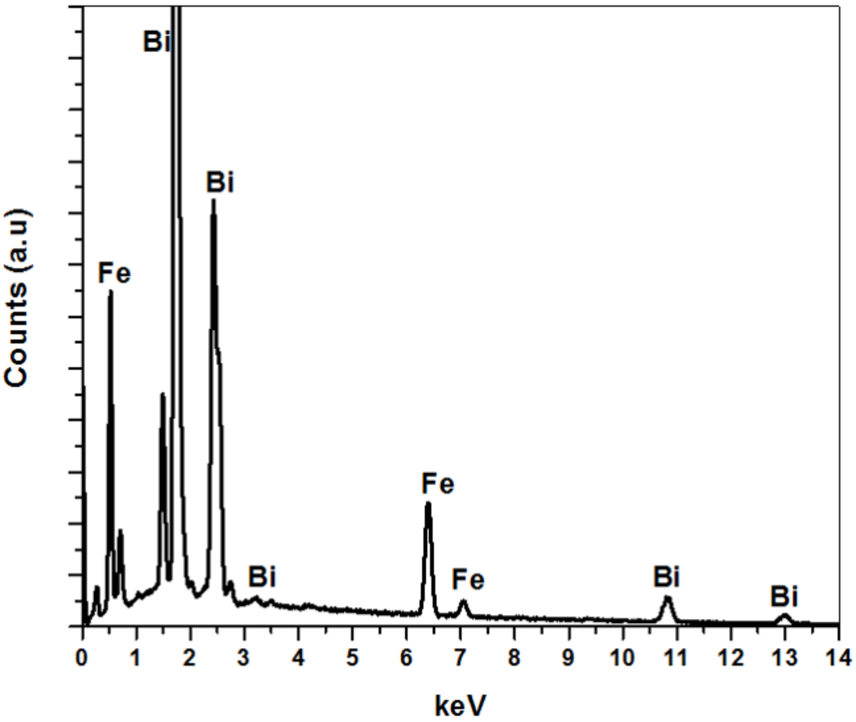

Figure 7.3: EDS spectra of BFO NTs confirming the constituent elements.

in many oxide compounds, the Bi 4f positions shown in the Fig. 7.4 (a) indicate that Bi exists in the form of BFO. No evident peaks are observed corresponding to lower oxidation states of Bi. The binding energy of 710.8 and 724.4 eV shown in Fig. 7.3(b) correspond to the Fe $2p_{3/2}$ and $Fe_{1/2}$ peaks arising from a spin-orbital interaction. Moreover, a broad satellite peak at 718.8 eV was found approximately 6-8 eV above the Fe $2p_{3/2}$ peak and was considered a characteristic of the mixed valence state of Fe [202, 203]. It is evident that Fe exists in both +2 and +3 states in as synthesized BFO NTs. According to the fitted XPS peak areas and atomic sensitivity factors for Bi and Fe elements, the Bi: Fe ratios are qualitatively determined to be 1.3:1, which closely resembles the EDX data. The existence of Bi vacancies is unlikely in BFO NTs as the Bi to Fe ratio is found to be more than 1. There is a high probability that oxygen vacancies might have been created in BFO to neutralize the charge arising from Fe^{+2} oxidation states. In stoichiometric BFO, the band gap is formed as a result of O 2p and Fe 3d hybrid states but the presence of oxygen vacancies may lower the adjacent 3d levels, thus creating sub-band gap defect states. These sub-band gap defect states might be the reason for anomalous photo properties in BFO NTs.

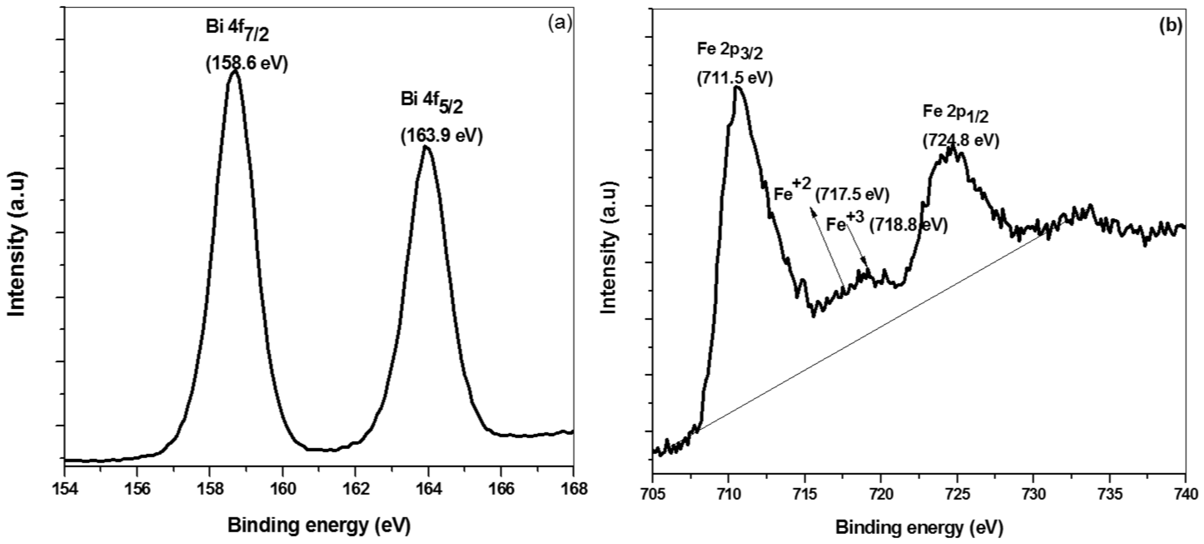

Figure 7.4: (a)High-resolution XPS core spectrum of Bi 4f and (b)XPS core spectrum of Fe 2p showing the availability of mixed valence state for Fe.

UV-Vis absorption spectrum

UV-Vis absorption spectra were measured using a Perkin Elmer Lambda-900 spectrometer 3000-190 nm. UV-Vis absorption spectrum of BFO NTs shown in Fig. 7.5 indicates significant visible light absorption, suggesting their potential use in visible light photocatalysis and photovoltaic applications. The optical absorption coefficient near the band edge follows [204]

$$(\alpha h\nu)^2 = A(h\nu - E_g) \tag{7.1}$$

Where α, h, ν, E_g are absorption coefficient, planks constant, the frequency of incident photons, band gap respectively and A is constant. The corresponding energy band gap of the material can be estimated from Kubelka-Munk (K-M) theory, from $(\alpha h\nu)^2$ and hν plot by extrapolating the linear portion of the ordinance to zero as shown in the inset of Fig. 7.5. The average band gap of BFO NTs was determined to be 2.5 eV, that is close to the reported values [108]. The wide photoabsorption spectrum in BFO nanostructures at sub-band gap illuminations could be attributed to the presence of an excess number of surface states [115]. The presence of surface states affects the band bending at the surface resulting in interesting photo properties [114]. A good linear fit above the band gap indicates direct band gap nature of BFO NTs.

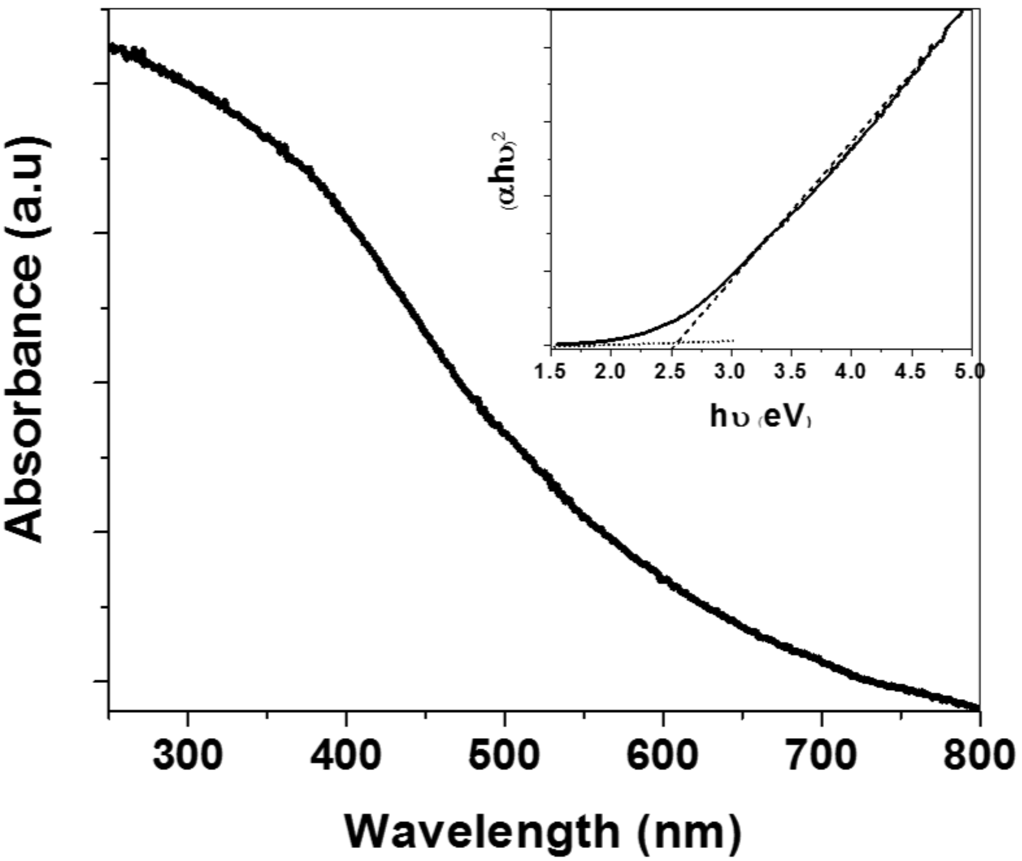

Figure 7.5: UV-Vis absorption spectrum obtained for BFO NTs. Inset shows the corresponding $(\alpha h\nu)^2$ and hν plot

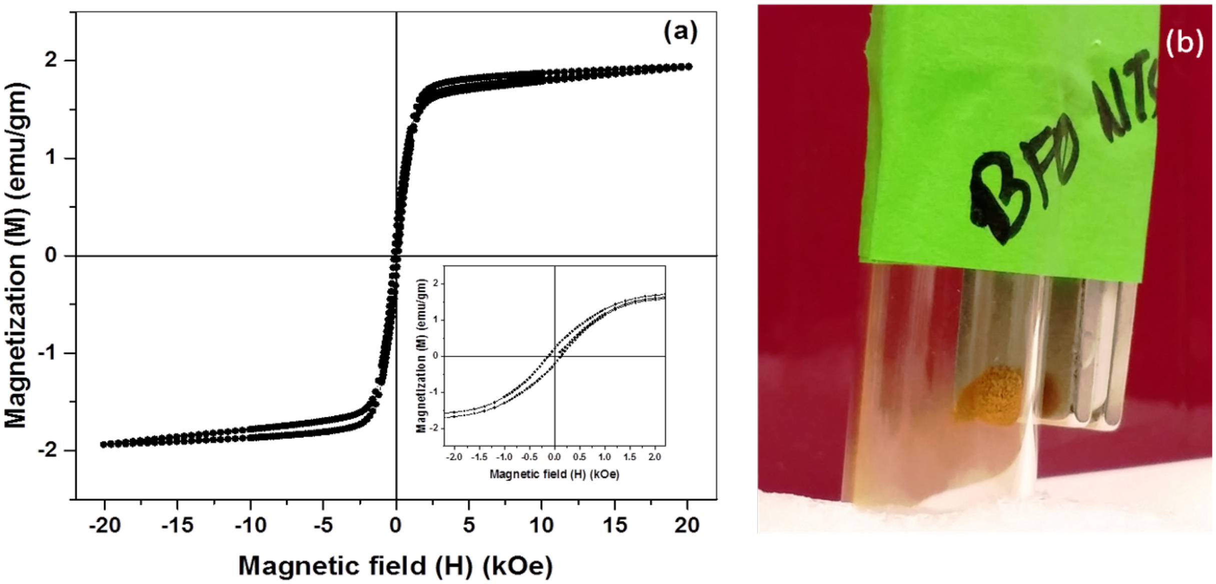

Figure 7.6: (a) Magnetization hysteresis loop of BFO NTs. (b) Picture showing easy magnetic separation of BFO NTs.

Magnetic nature characterization

As BFO is a multiferroic material having ferroelectric properties at room temperature, we have investigated the magnetic nature of BFO NTs. Magnetic properties were characterized by a vibrating sample magnetometer (VSM) at room temperature. As shown in the Fig. 7.6 (a), a significant ferromagnetic order with a saturated magnetization (M) of ≈1.94 emu/gm is observed for BFO NTs at room temperature, which is different from the linear M-H behavior in bulk BFO. The partially enlarged M-H curve shown in the inset reveals that the coercive field of BFO NTs is quite small ≈100 Oe. It was suggested that size effect of BFO nanostructures might be responsible for the magnetic ordering to exhibit ferromagnetism at the nanoscale. The presence of ferromagnetic order in BFO NTs can be attributed to the non-cancellation of the spiral spin structure with a period of 62 nm [205]. The BFO nanostructures with dimensions typically below 62 nm can possess favorable magnetic properties due to their grain size confinement, an effect that has been found to partially destroy the long range spiral spin structure of bulk BFO [206,207]. Photostability and easy separation are important for any photocatalyst. The easy magnetic separation depicted in Fig. 7.6(b), suggests the fact that BFO NTs can be considered as a promising material in semiconductor photocatalysis.

7.4 Anamalous photo effects in BFO nanotubes

The wide and enhanced photoabsorption in BFO NTs indicates the presence of sub-band gap defect states that have a direct influence on the photo properties. A detailed understanding of the effects of surface states on the optoelectronic properties of nanostructures is vital in extending the further use of BFO applications. In order to investigate the effect of these defect states we have carried out PL studies. The room temperature PL studies were conducted using a Cary Eclipse Fluorescence Spectrometer from Agilent Technologies. The slit width was kept at 5 nm for both emission and excitation spectra to obtain sharp PL characteristics. Here, we report strong visible PL in BFO NTs as a result of high concentration of oxygen vacancies. Contrary to the common perception of intense near band emission (NBE) in other nanostructures [208], BFO NTs show more intense defect level emission (DLE) as a result of the high concentration of oxygen vacancies. The presence of oxygen vacancies is more pronounced due to high surface area of BFO NTs resulted from its extremely thin walls ($\approx$20 nm).

Fig. 7.7 shows the room temperature PL emission spectrum of BFO NTs at an excitation wavelength of 400 nm. This wavelength of 400 nm was chosen by analyzing excitation spectrum at an emission wavelength of 540 nm as shown in the inset of Fig. 7.7. Three principal emissions were observed in the emission spectrum; one at 484 nm (2.55 eV), and others at 529 nm (2.34 eV) and 545 nm (2.2 eV). It is evident from Fig. 7.7 that the green emission at 545 nm is much stronger than the other two. As the excitation wavelength is changed, the emissions at 484 nm and 529 nm remained constant whereas the intense emission changed its position and intensity as shown in Fig. 7.8. From these observations, the emission at 484 nm (2.55 eV) could be attributed to NBE as a result of the radiative transition of photo-generated carriers. The smaller emission at 529 nm (2.34 eV) could be attributed to the presence of shallow acceptor-donor energy level which is 0.21 eV below the conduction band. These shallow acceptor-donor energy levels may be originated by defects at the grain boundaries or due to unavoidable impurities as shown in XRD in Fig. 7.1 or might be due to other valence states of oxygen vacancies [209, 210].

The intense green emission at 545 nm (2.2 eV) is attributed to oxygen vacancies present in BFO NTs. Defect emissions as a result of oxygen vacancies are well studied, but these defect emissions are considered as an emission loss and reported to be broad and weak [211]. Interestingly, in the case of BFO NTs, the DLE is much stronger and sharp. These oxygen vacancies act as potential recombination centers, or traps, for the carriers, which provide alternate paths for energy transfer and result in strong emission characteristics in the

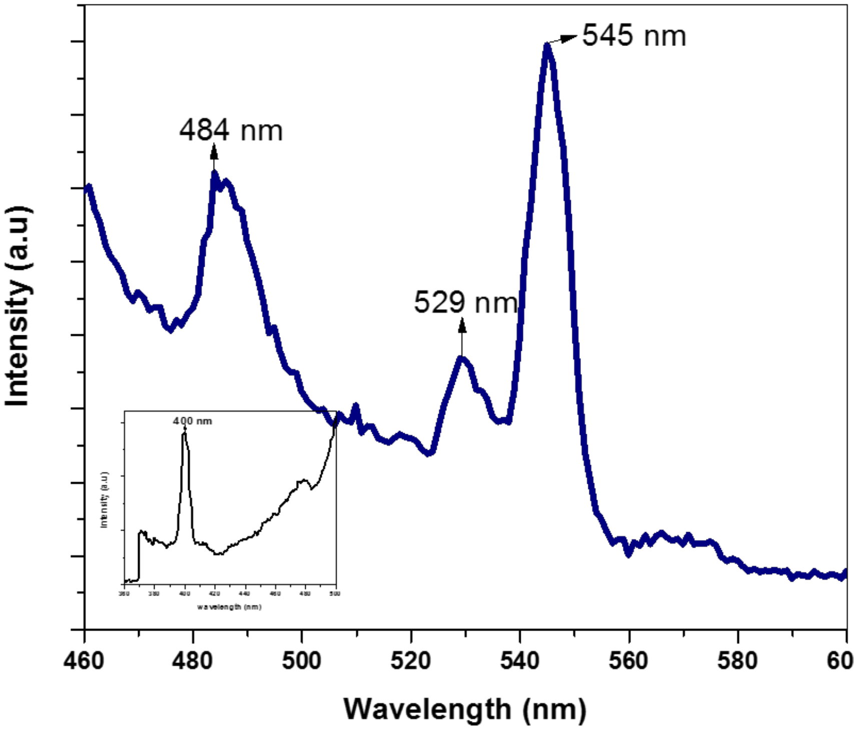

Figure 7.7: Room temperature PL spectra of BFO NTs at an excitation wavelength of 401 nm. Inset shows excitation spectra obtained for an emission wavelength of 545 nm.

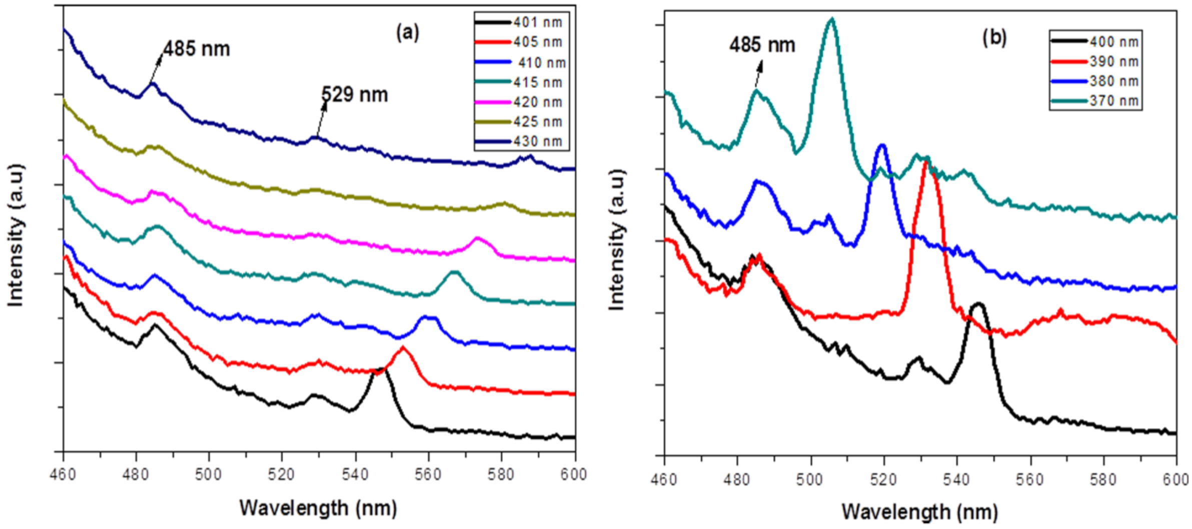

Figure 7.8: (a) Defect level emission (DLE) shifting towards red when excitation wavelength is increased from 401 nm to 430 nm in BFO NTs. (b) Defect level emission (DLE) shifting towards blue when excitation wavelength is decreased from 400 nm to 370 nm in BFO NTs. The near band emissions (NBE) at 484 nm and 529 nm remained constant irrespective of the excitation wavelength

PL spectrum. These oxygen vacancies are created to maintain the charge neutrality in multi-cation perovskite structures like BFO. As shown in Fig. 7.8 the green emission is shifted towards blue when the excitation wavelength is decreased from 400 nm and shifted towards red when the excitation wavelength is increased from 400 nm. The linear shift in the defect emission can be explained based on the number of photo-induced carriers, which are excited from the valence band to the oxygen vacancies with respect to excitation energy. The transition of photo-induced carriers from the oxygen vacancies to valence band results in green emission, thus changing its position and intensity with respect to excitation energy. A linear shift in the intense defect emission with respect to the excitation energy can be explained based on the occupancy of oxygen vacancies and detrapping ability to emit to the valence band [212]. Similar visible emission in PL spectrum with similar trends in the emission shift were observed in various nanostructures, such as nanoparticles (NPs) and nanowires (NWs) prepared using the same method under similar conditions. These results indicate that nanostructures of different morphology with different surface-to-volume ratio may affect the intensities of defect emissions, but not emission positions.

Mechanism

We suggest that abundant oxygen vacancies in BFO NTs act as deep carrier traps possessing occupancy according to Fermi-Dirac distribution. As the excitation energy is increased, a larger number of photo-induced carriers get excited to the oxygen vacancies resulting in an intense green emission as a result of the radiative transitions while emission. At lower energies (excitation at 450 nm), a smaller number of carriers are excited from the valence band to the oxygen vacancies resulting in a weak green emission, but still a stronger emission than the NBE. Defect emissions were further confirmed by conducting surface passivation studies. Since chemical passivation and annealing at high temperatures could not eliminate oxygen vacancies completely [114], physical passivation using a polymer coating was conducted to demonstrate the decrease in DLE to NBE intensity ratio as depicted in Fig. 7.9.

The observed PL spectrum can be interpreted according to the band structure as shown in Fig. 7.10. The emission at 484 nm is a result of the band-to-band electron transition, confirmed with the band gap of 2.55 eV from UV-Vis data. The emission at 529 nm is assigned as shallow energy state as a result of the defect in the grain boundary or impurity. The intense green emission at 545 nm is due to oxygen vacancies which are located in the sub-band gap as dense trap states. Oxygen vacancies are denoted as V_O^{-2} in Fig. 7.10.

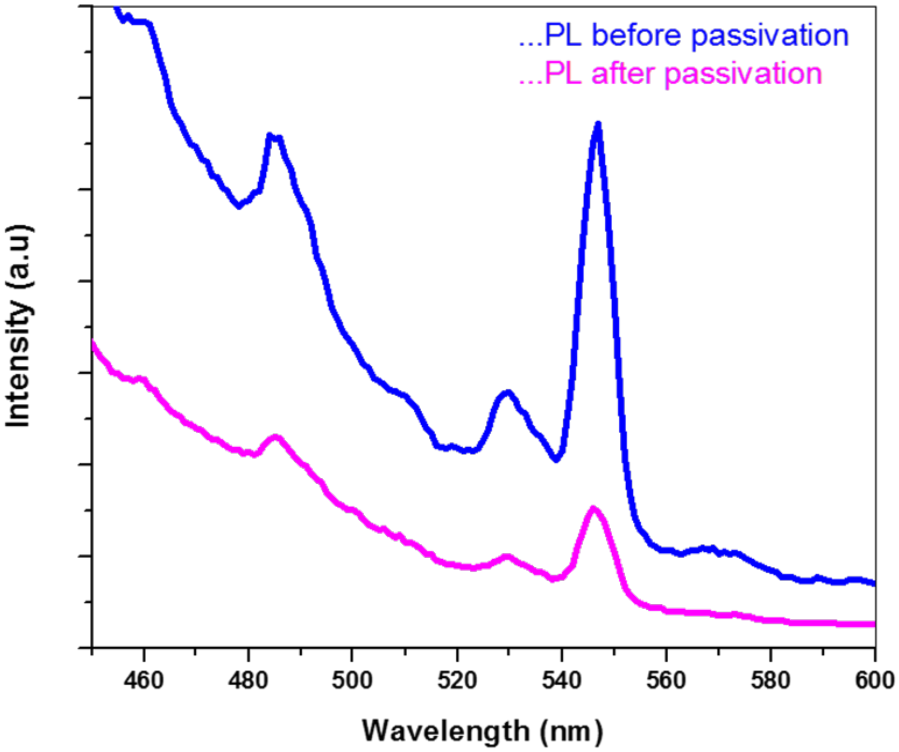

Figure 7.9: PL results showing significant decrease in DLE due to surface passivation using a polymer. It is to be noted that relative to NBE, DLE is always of higher intensity

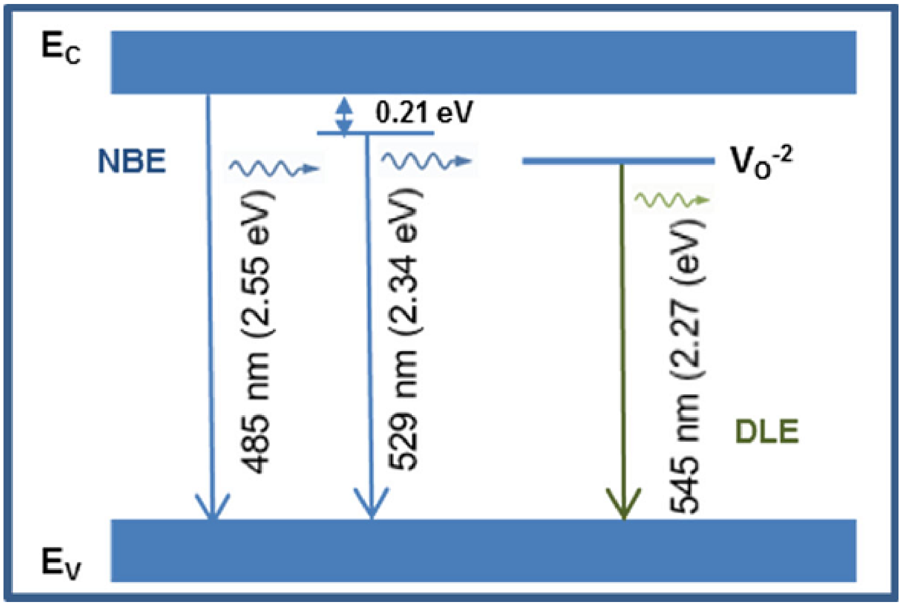

Figure 7.10: Schematic representation of electronic band structure of BFO NTs

7.5 BFO as a visible light photocatalyst

Photocatalytic activity test

The photocatalytic activity of BFO NTs were evaluated by the degradation of methylene blue (MB), a prototype organic contaminant, in aqueous solution under visible light irradiation (300 W halogen lamp with a cutoff filter greater than 420 nm). The experimental set up for visible light irradiation was indigenously made according to the requirements using a projector lamp and an optical mirror to focus the light. The lamp intensity was maintained at 70 mW/cm^2 throughout the experiment. In a typical reaction run, 20 ml of MB (10 mg/l) aqueous solution (DI water as solvent), was added to an optimized amount of photocatalyst. The reaction temperature was kept at room temperature using a cooling arrangement to avoid any thermal catalytic effect. After an elapse of time under illumination, a small quantity of the solution was taken, and the concentration of MB was determined using UV-Vis absorption spectroscopy, after removing the catalyst by centrifugation at 4000 rpm for 5 min followed by magnetic separation. The concentration of MB in the solution was determined by measuring the absorbance at 665 nm using UV-Vis spectrophotometer. The absorbance was converted to concentration referring to a standard calibration curve. To confirm the visible light photocatalytic activity, blank MB solution sample without the catalyst under illumination and with catalyst without illumination were studied as control experiments.

The photocatalytic activity of BFO NTs was evaluated by the degradation of MB aqueous solution under visible light illumination, by inspecting MB major absorption peak at 665 nm. The initial concentration of the MB aqueous solution 10 mg/l for all the tests. The concentration of photocatalyst loading was optimized to be 5 g/l considering the fact that higher concentration of catalyst will have adverse effects due to more light scattering than absorption. The temporal evolution of the spectral changes taking place during the photodegradation of MB using BFO NTs is displayed in Fig. 7.11 (a). Before the illumination, the suspensions were magnetically stirred in dark for 2 hr to obtain adsorption-desorption equilibrium between the photocatalyst and MB as shown in Fig. 7.12.

It is evident from Fig. 7.11 (a) that a noticeable change in absorbance of MB is observed after 120 min of magnetic stirring in dark in the presence of BFO NTs, amounting to be a $\approx$25% reduction in the concentration of MB. This result indicates that BFO NTs have good adsorbability due to higher surface area of NTs providing more number

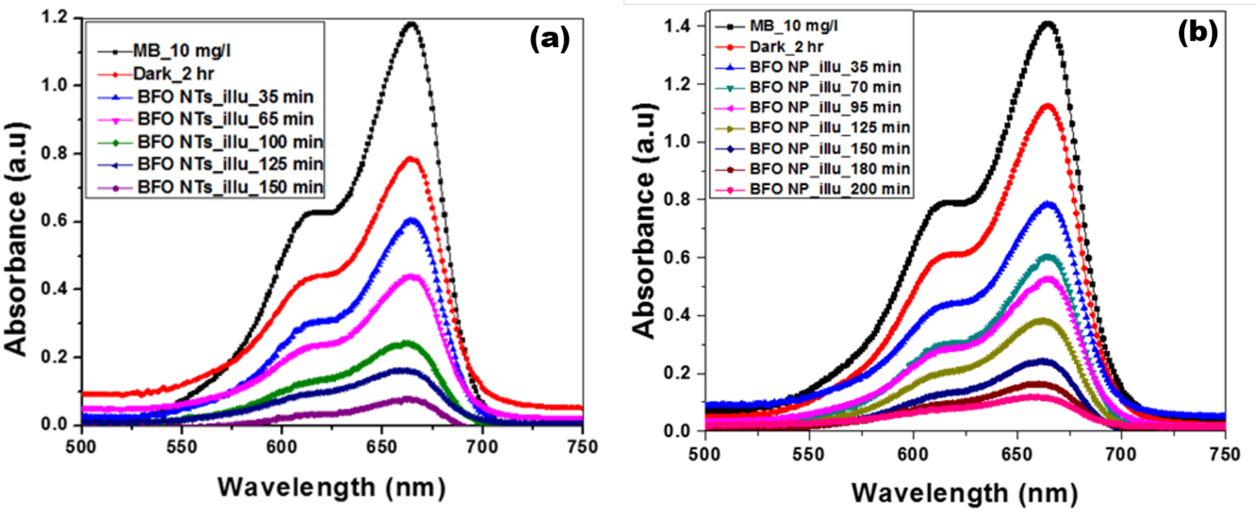

Figure 7.11: (a) Temporal UV-Vis kinetics of MB aqueous solution in the presence of BFO NTs under illumination. (b) Temporal UV-Vis kinetics of MB aqueous solution in the presence of BFO NPs under illumination.

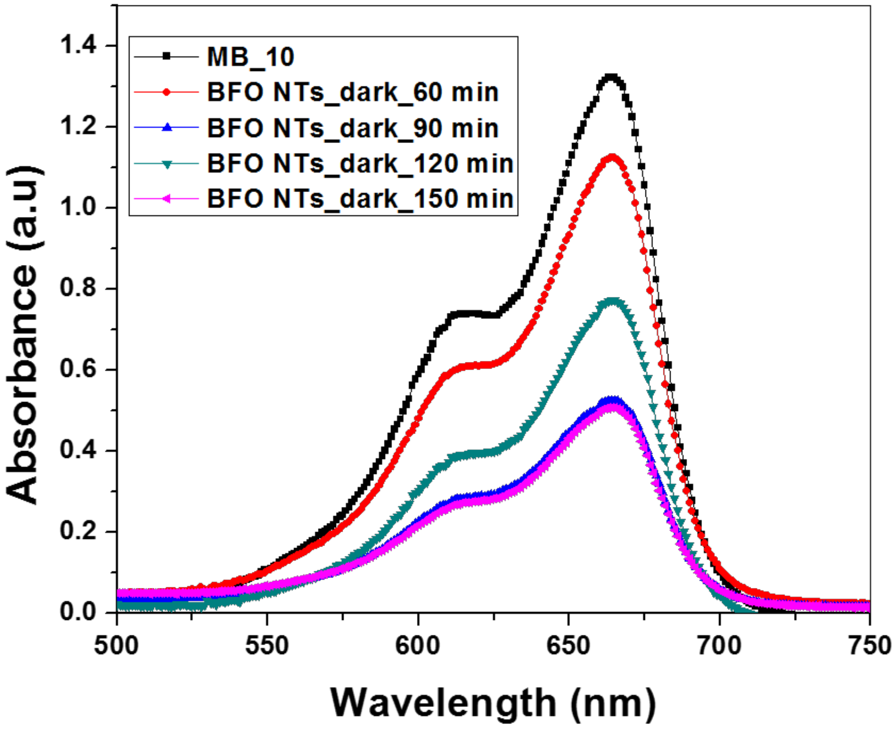

Figure 7.12: Temporal kinetics of MB in the presence of BFO NTs under dark conditions. It is evident from the figure that the initial sudden drop is due to the adsorption of MB on BFO NTs. The adsorption-desorption equilibrium is attained after 120 min.

of available adsorption sites, thus MB molecules are quickly transferred from solution phase to the surface of the photocatalyst. The absorption peaks corresponding to MB almost disappeared after about 150 min of visible light irradiation, suggesting the excellent photocatalytic activity of BFO NTs. Similar experiments are conducted using BFO NPs of diameter ≈80 nm. The temporal evolution of the spectral changes taking place during the photodegradation of MB using BFO NPs is displayed in Fig. 7.11 (b). The initial sudden decrease in the concentration of MB absorption peak at 665 nm after adsorption-desorption equilibrium in Fig. 7.11 (a) and Fig. 7.11 (b) indicates that the adsorbability of BFO NTs is more compared to BFO NPs. The higher adsorbability of BFO NTs could be attributed to the high surface area provided by the NTs in comparison to NPs. From the Fig. 7.11 (b) it is observed that the absorbance of MB reached to 85% of its initial value after an irradiation time of 200 min. The enhanced photocatalytic activity of BFO NTs compared to BFO NPs can be attributed to high MB adsorbability of BFO NTs and the ultra-thin wall thickness of BFO NTs facilitating the photo-generated carriers to reach the surface without much bulk recombination.

The photodegradation kinetics of MB in aqueous solution under visible light irradiation is displayed in Fig. 7.13. From the Fig. 7.13, it is evident that control experiment such as MB without any catalyst under illumination exhibit extremely small (only 5%) self-photocatalysis for the whole illumination. The degradation of the MB with BFO NTs under dark conditions for 4 hrs also show similar result demonstrating that the absorption of MB on BFO NTs is limited after the absorption-desorption equilibrium is attained. However after 150 min of illumination in the presence of BFO NTs, the MB degradation rate is 95%. The above result clearly demonstrates significantly high degradation efficiencies for MB with BFO NTs under illumination. The concentrations of MB at different times were calculated from the absorbance value using calibration curve plotted for MB as shown in Fig. 7.14. Furthermore, the photocatalytic kinetics of BFO NTs for aqueous MB solution was investigated using Langmuir-Hinshelwood model expressed as [213]

$$ln(\frac{C}{C_0}) = kt \tag{7.2}$$

where C, C_0, k and t are concentration of MB after time 't', initial concentration, first order rate constant and time respectively.

Fig. 7.13 inset, it is evident that the photocatalytic degradation follows first order rate of reaction approximation. The value of rate constant 'k' is determined to be 0.014 per min (0.87 h^{-1}), much higher than that of the reported for bulk BFO. The photostability of the

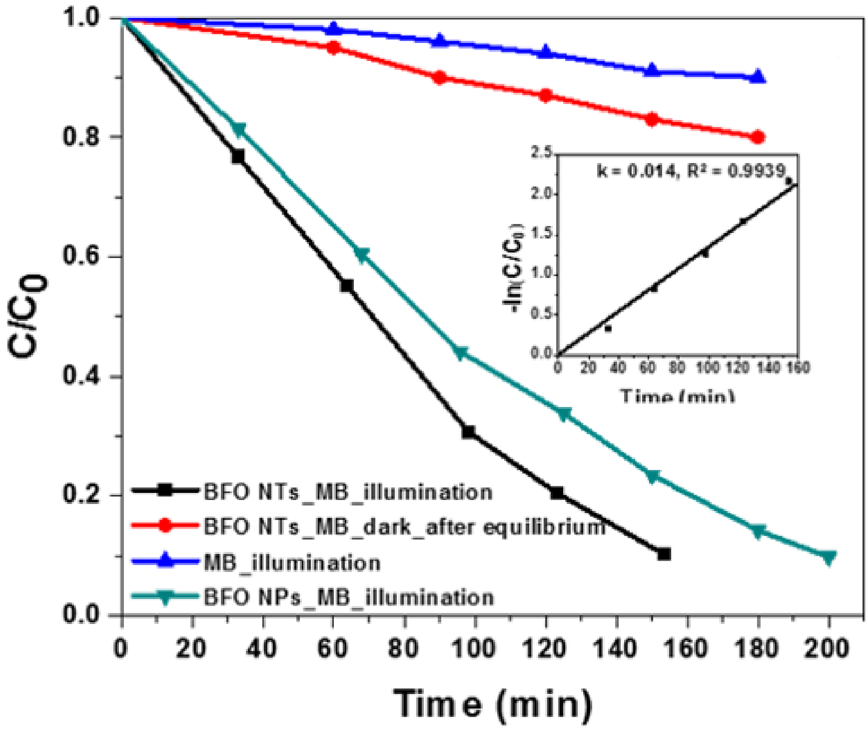

Figure 7.13: Photocatalytic reaction kinetics of MB using BFO NTs and BFO NPs. Inset shows the first order reaction rate for BFO NTs.

BFO NTs was investigated using XRD of the photocatalyst before and after illumination as presented in Fig. 7.15. The XRD data shows no significant change in crystal structure of BFO NTs even after 3 runs of photocatalysis, suggesting excellent photostability in applications for reusable visible light photocatalysis.

Mechanism

The mechanism for the enhanced photocatalytic activity of BFO NTs is explained using the schematic as shown in Fig. 7.16. When BFO NTs are illuminated with light of appropriate wavelength, photo-excited carriers are generated in the semiconductor. The subsequent de-excitation process, after the initial photo-excitation, involves electron or energy transfer resulting in redox reactions at the surface as shown in 7.16. The probability and the rate of the charge transfer depend on adsorbability of contaminants on the surface, availability of charge carriers at the surface and the positions of the band edges relative to the redox potential levels of the adsorbate. Counteracting to charge transfer process, electrons or holes may recombine within the volume of the material (bulk recombination) or on the surface (surface recombination) with the release of heat. The unique geometric features

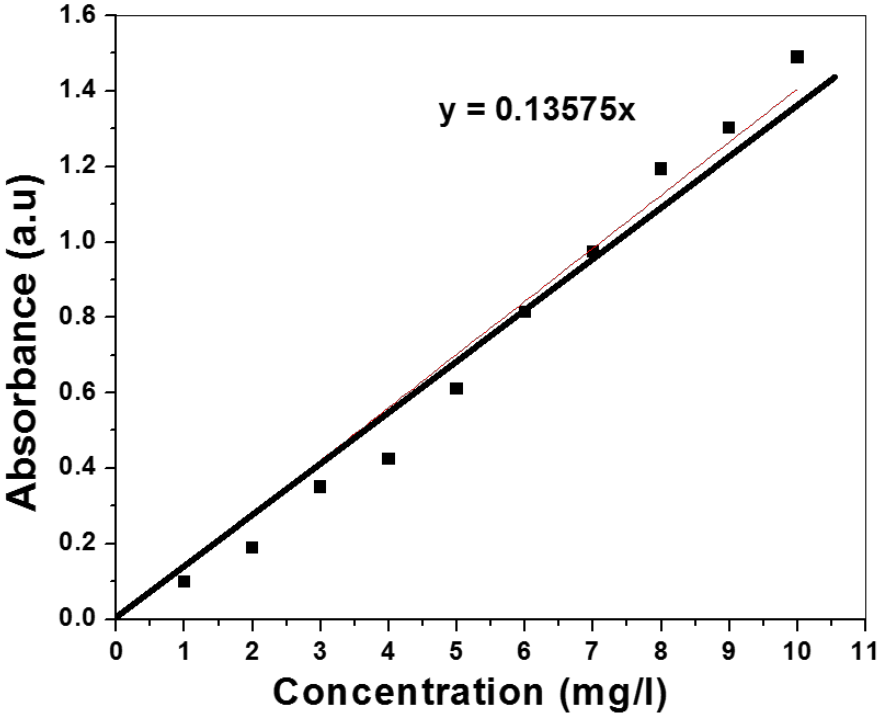

Figure 7.14: Calibration curve of MB aqueous solution at various concentrations at an absorption wavelength of 665 nm and path length of 1 cm.

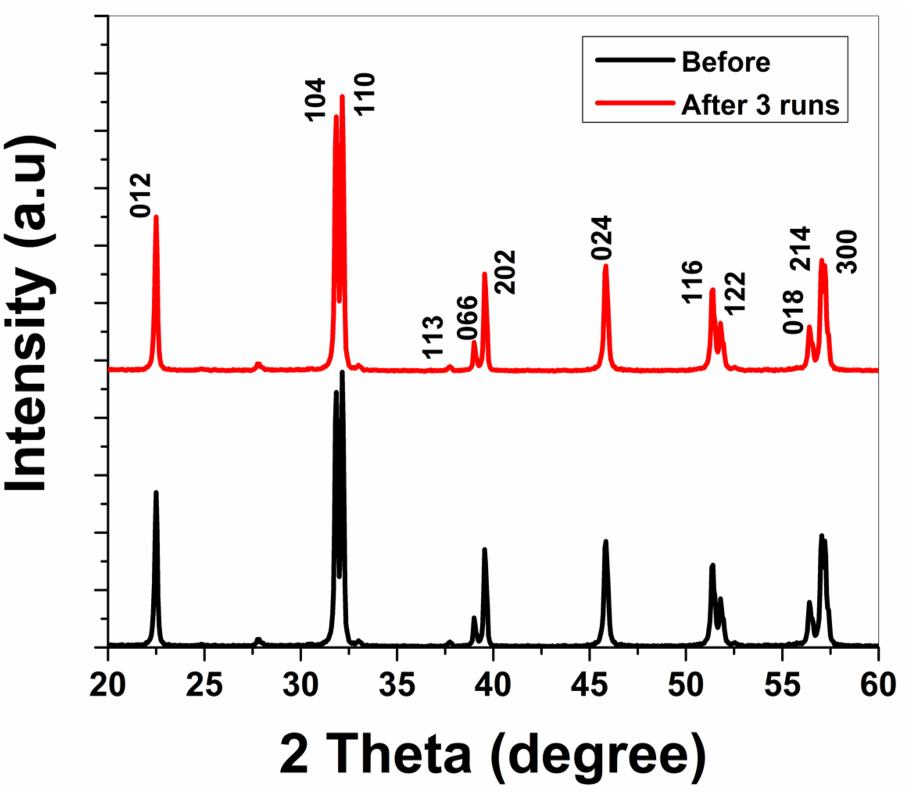

Figure 7.15: Demonstration of photostability of BFO by inspecting XRD spectra of BFO NTs before and after 3 runs of photocatalysis.

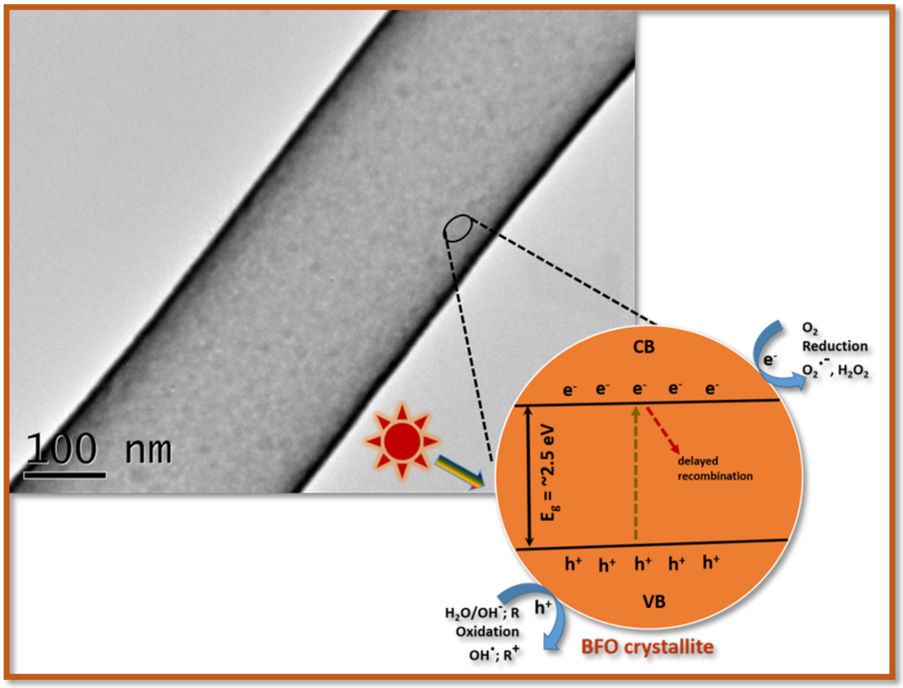

Figure 7.16: Schematic describing the mechanism of photocatalysis using BFO NTs

obtained by BFO NTs such as continuous structural integrity, extremely large interface area and ultra-thin wall thickness promote rapid diffusion of photogenerated carriers onto the surface before recombination occurs. In the case of BFO NTs once the charge separation is established, the electrons excited to the conduction band get delocalized and diffuse into these interconnected crystallites thus reducing the recombination [214]. The presence of surface states in the sub-band gap due to oxygen vacancies acts as electron donors thus facilitating charge transfer process [215]. The enhanced photocatalytic activity for BFO NTs compared to BFO NPs is due to the favorable charge transfer process between the adsorbate and substrate dominating the recombination of the carriers [216]. BFO NTs possess wide-spectrum optical absorption, high adsorbability, easy charge transfer process through ultra-thin wall thickness, excellent photostability, and easy magnetic separation, thus making it a promising candidate for visible light photocatalysis.

7.6 Conclusion

In summary, this chapter provides the detailed investigation of anomalous photo properties of BFO. Oxygen vacancies are created in BFO to neutralize the charge arising from Fe^{+2} oxidation states and are more pronounced in high surface area nanostructures. Oxygen vacancy dominant strong visible PL has been observed from BFO NTs and studied in detail. Understanding of the oxygen vacancies present in BFO NTs makes them interesting candidates for future visible light optoelectronic applications. One of the promising applications of using visible light is in photocatalysis. We have demonstrated enhanced visible light photocatalytic activity in BFO NTs. BFO NPs synthesized by the same method with the mean diameter of 80 nm show much less degradation activity compared to NTs. The continuity of the NTs, ultra- thin wall thickness (20 nm) and high interface area facilitate charge transfer process for redox reactions at the surface due to short diffusion lengths of photo carriers in NTs. The reported results on BFO NTs show promise for visible light photocatalysis because they possess excellent photostability, easy magnetic separation, significant visible light absorption and excellent photocatalytic activity. It is suggested that doping with heavy metal ions, noble metal decoration on the surface and operating at lower pH can further improve the visible light photocatalytic activity of BFO nanostructures. Temperature-induced population and de-population effect of surface states have been taken as an advantage to demonstrate molecular detection of trace quantity analytes using photothermal electrical resonance spectroscopy in our group.

Chapter 8

Conclusions and Future scope

8.1 Scientific contribution

Microfabricated sensors are proven to be excellent gravimetric sensors reaching a mass sensitivity of single protein [217]. Despite having great success and unprecedented sensitivities, real-time applications of theses sensors are limited due to poor chemical selectivity. Developing chemo-selective interfaces was attempted to solve the problem but realized that it was not sufficient enough [14]. Later photothermal techniques have been proposed to combine the high thermal sensitivity of these minuscule mass devices and extremely selective IR optical techniques in the molecular finger print region. Though application of photothermal techniques provide chemical identification from trace quantities on the surface of the sensor, one of the important feature of these techniques rely on the thermal sensitivity of the sensor. In the cutting edge time of approaching towards single-molecule nanomechanical mass spectrometry using NEMS [41], it is very important to have an orthogonal signal that can provide chemical identity of the analyte along with the mass information. In order to achieve this feat a thorough understanding of photo effects on MEMS/NEMS is not only crucial but also helps to build an insight towards nanomechanical analytical tools. Two novel and exciting sensor platforms namely, a SMR and a nanomechanical string have been selected for the study of dynamic behavior of these resonators under periodic IR radiation. Similar concept has been extended to fabricate an ultra-low thermal mass, thermally responsive suspended nanostructure. In the process we have explored anomalous photo behavior of BFO NTs and demonstrated a photocatalytic application.

One of the objective of the current thesis was to add chemical selectivity feature to the novel design of of SMRs. SMRs solve a decade old problem of damping issues in resonators when operated in liquid. We have converted the SMRs sensitive to temperature by converting them to bimaterial using a metal coating. Detailed experimental and theoretical investigations have been presented in the thesis. We have demonstrated a photothermal identification $\approx$ 1 ng in 113.5 ng mixture and predict that the resolution can go down to hundreds of picogram. Figures of merit have been discussed considering BMC as a thermal sensor. Though bimaterial cantilevers made of Si based materials have demonstrated superior thermal sensitivity, these BMCs have the advantage of chemical identification in the presence of liquid which is the need of the hour in biosensing applications. Efforts were made to widen the scope of BMC not just limited to gravimetric sensing but to add chemical identification feature and to use them as a thermo-analytical tool to estimate liquid thermal properties. In all these studies the static deflection of BMC due to thermal stress created because of the temperature gradient has been monitored. As discussed in Chapter 3, the sensitivity of chemical identification using photothermal techniques largely depends on the power of the IR, length and compliance of the device, thermal stress generated, thickness of the metal used, channel volume and noise in the measurement. Longer and lanky BMC with higher channel volume is suitable for lower detection limit but at the same time these characteristics also increase noise in the measurement.

Though BMC has its own merits in biosensing applications, from a miniaturization point of view bulky SMR cannot give best mass resolution hence one has to strike a balance between mass resolution and chemical identification using photothermal techniques in static deflection mode.

Recently silicon nitride nanomechanical strings have attracted great interest in the community of nanomechanics due to their exceptional quality factors as gravimetric sensors and temperature sensitivity. We have utilized the extreme thermal sensitivity of strings to demonstrate molecular identification from trace quantities analytes on a string surface using photothermal techniques. In contrast to deflection of the BMC to temperature here the change in frequency related dynamics of the string with respect to temperature have been monitored. Detailed theoretical and experimental analysis of dynamic thermomechanical behavior of string under periodic IR pulses has been presented. As discussed in chapters 5 and 6, the limit of detection for molecular identification using strings depends on IR power, IR spectral absorption characteristics of the analyte and thermal characteristics of the string. The thermal sensitivity of the string vibration mode number, Young's modulus of the string material, difference in thermal expansion coefficient of the string and support materials and inversely proportional to length density and pre-stress as given by the equation 2.5.3. Details of frequency shift of the string with respect to temperature also depends on the accuracy of frequency measurement. Though metallic strings can be considered as good choice for string materials but the frequency stability has been the issue hence silicon nitride strings have been chosen as the string material for further studies. An explosive material (RDX) has been used as a typical example to demonstrate femtogram scale ($\approx$ 42 fg) molecular recognition (lowest ever reported). Though nanomechanical string based sensors possess exceptionally good mass resolution and molecular identification by photothermal techniques, the experimental set up involving vacuum and optical method of reading the vibration of the string limit the scope to real-time applications.

In order to combine the mass sensitivity of minuscule mass string resonators and thermally active material nature, we have fabricated a suspended BFO NW pinned at the anchor points. BFO is a well known pyroelectric material along with its multiferroic properties. Though our initial experiments with IR did not give any positive results, we have observed anomalous photo behavior of BFO nanostructures. We have investigated the peculiar and interesting photo behavior of BFO and attributed the reason to be the surface states which have profound importance at the nanoscale. Oxygen vacancies present in BFO nanostructures play an important role in photoabsorption and photoluminescnce properties. These effects are studied in detail and an enhanced photocatalytic activity of BFO NTs has been demonstrated relative to BFO NPs. The efficient charge transport characteristics, excellent photostability and easy magnetic separation make BFO NTs a potential visible light photocatalyst. The study of surface states and their behavior upon photon irradiation can be a useful study considering BFO nanostructures as electrical resonators.

8.2 Achievements

1. Molecular identification of trace quantities ($\approx$ 1.15 ng) of analytes has been demonstrated using a novel BMC design and photothermal spectroscopy techniques.

2. Thermomechanical response of BMC when subjected to periodic IR radiation has been studied in detail. Figures of merit have been found considering BMC as a thermal sensor. A thorough understanding of heat transfer to and from the BMC has been studied.

3. Efforts are made to widen the scope of SMRs for not just mass sensing in the

presence of liquid but also to provide dynamic thermal properties of picoliter volume of liquid/colloidal solutions.

4. Dynamic thermomechanical response of nanomechanical strings were studied in detail to understand the thermal sensitivity of strings. Most influential parameters affecting the performance of strings were optimized and figure of merits have been found.

5. Molecular signature from femtogram quantities of analyte (RDX) on the string surface has been demonstrated. The thermomechanical frequency detuning of the string with RDX on it, has been monitored with respect to IR wavelength scan.

6. Oxygen vacancy dominated anomalous and strong visible photoluminescnce from BFO NTs has been studied in detail.

7. Enhanced visible light photocatalytic activity of BFO NTs relative NPs has been demonstrated. High interface area of BFO NTs and charge transport characteristics were studied in detail.

8.3 Future scope

To decrease the limit of detection in molecular identification using photothermal spectroscopy one has to fully understand the thermomechanical behavior of BMC. Here an effort was made considering the liquid as one more layer and solved the heat continuity equation in one dimension (along length) under steady state conditions. However this assumption does not represent the system with full accuracy but largely demonstrate the typical bimorph behavior. Detail analysis is required considering the heat flow in all directions.

We have demonstrated the detection of ≈ 1.15 ng of ethanol in ethanol-water binary mixtures of 113.5 ng mixture weight. To demonstrate high optical selectivity using photothermal spectroscopy techniques a complex mixture analysis involving more analytes can be vital to demonstrate real-time applications.

A detailed heat transfer model has the ability to estimate dynamic thermal properties of the BMC constituents when subjected to heating. We made an effort to estimate the thermal diffusivity of picoliter volume liquids by measuring the time constant of loaded BMC subjected to heat pulses. A thorough studies are yet to be performed to understand the nanoscale heat transport in liquid/colloidal solutions. This kind of study is vital in evaluating colloidal nano-coolants in the electronic industry.

Investigation of nanomechanical strings as thermal sensors not only add chemical selectivity feature to the highly mass sensitive strings but also useful as thermo-analytical tools. We have demonstrated identification of ≈ 42 fg of RDX using photothermal techniques and developed a detail theory considering strings as thermal sensors. In the process of utilizing the full strength of strings as thermal sensors many fundamental studies such as plasmonic behavior of single gold nanostructures, thermal behavior of polymers, observation of chemical reactions on the string..etc.

From the insights of this thesis we anticipate that photothermal spectroscopy of biomolecules using microchannel embedded string resonators could be interesting as it combines the thermal sensitivity of strings and ability to operate in liquid. We propose that by fabricating highly IR absorbing grating structures on the string, we can use strings as uncooled thermal detectors.

Anomalous photo behavior of BFO nanostructures investigated in this thesis are vital in exploring the optoelectronic applications of BFO. Enhanced photocatalytic activity of BFO NTs has been reported and propose that metal particle decoration or heavy metal doping can further increase the potential of BFO as visible light photocatalyst. As presented in the thesis if BFO can be fabricated as a nanomechanical string, many of the functionalities of BFO can be put in use to further explore functional nanostrings.

Bibliography

[1] Marc J Madou. *Fundamentals of microfabrication: the science of miniaturization*. CRC press, 2002.

[2] LA Pinnaduwage, V Boiadjiev, JE Hawk, and T Thundat. Sensitive detection of plastic explosives with self-assembled monolayer-coated microcantilevers. *Applied Physics Letters*, 83(7):1471–1473, 2003.

[3] LA Pinnaduwage, T Thundat, JE Hawk, DL Hedden, PF Britt, EJ Houser, S Stepnowski, RA McGill, and D Bubb. Detection of 2, 4-dinitrotoluene using microcantilever sensors. *Sensors and Actuators B: Chemical*, 99(2):223–229, 2004.

[4] Guanghua Wu, Ram H Datar, Karolyn M Hansen, Thomas Thundat, Richard J Cote, and Arun Majumdar. Bioassay of prostate-specific antigen (psa) using microcantilevers. *Nature Biotechnology*, 19(9):856–860, 2001.

[5] Nickolay V Lavrik and Panos G Datskos. Femtogram mass detection using photothermally actuated nanomechanical resonators. *Applied Physics Letters*, 82(16):2697–2699, 2003.

[6] B Lassagne, D Garcia-Sanchez, A Aguasca, and A Bachtold. Ultrasensitive mass sensing with a nanotube electromechanical resonator. *Nano Letters*, 8(11):3735–3738, 2008.

[7] Julien Chaste, A Eichler, J Moser, G Ceballos, R Rurali, and A Bachtold. A nanomechanical mass sensor with yoctogram resolution. *Nature Nanotechnology*, 7(5):301–304, 2012.

[8] Anja Boisen, Søren Dohn, Stephan Sylvest Keller, Silvan Schmid, and Maria Tenje. Cantilever-like micromechanical sensors. *Reports on Progress in Physics*, 74(3):036101, 2011.

[9] BD Hauer, C Doolin, KSD Beach, and JP Davis. A general procedure for thermomechanical calibration of nano/micro-mechanical resonators. *Annals of Physics*, 339:181–207, 2013.

[10] Laura G Carrascosa, M Moreno, Mar Álvarez, and Laura M Lechuga. Nanomechanical biosensors: a new sensing tool. *TrAC Trends in Analytical Chemistry*, 25(3):196–206, 2006.

[11] Seonghwan Kim, Dongkyu Lee, Xunchen Liu, Charles Van Neste, Sangmin Jeon, and Thomas Thundat. Molecular recognition using receptor-free nanomechanical infrared spectroscopy based on a quantum cascade laser. *Scientific Reports*, 3, 2013.

[12] Jürgen Fritz. Cantilever biosensors. *Analyst*, 133(7):855–863, 2008.

[13] Abraham J Qavi, Adam L Washburn, Ji-Yeon Byeon, and Ryan C Bailey. Label-free technologies for quantitative multiparameter biological analysis. *Analytical and Bioanalytical Chemistry*, 394(1):121–135, 2009.

[14] Srikanth Singamaneni, Melburne C LeMieux, Hans P Lang, Christoph Gerber, Yee Lam, Stefan Zauscher, Panos G Datskos, Nikolay V Lavrik, Hao Jiang, Rajesh R Naik, et al. Bimaterial microcantilevers as a hybrid sensing platform. *Advanced Materials*, 20(4):653–680, 2008.

[15] Kyo Seon Hwang, Sang-Myung Lee, Sang Kyung Kim, Jeong Hoon Lee, and Tae Song Kim. Micro-and nanocantilever devices and systems for biomolecule detection. *Annual Review of Analytical Chemistry*, 2:77–98, 2009.

[16] Thomas Thundat, Mehrdad Bagheri, Seonghwan Kim, Dongkyu Lee, and Samgmin Jeon. Photothermal cantilever deflection spectroscopy. In *Meeting Abstracts*, number 59, pages 3995–3995. The Electrochemical Society, 2012.

[17] Adam R Krause, Charles Van Neste, Larry Senesac, Thomas Thundat, and Eric Finot. Trace explosive detection using photothermal deflection spectroscopy. *Journal of Applied Physics*, 103(9):094906, 2008.

[18] Thomas P Burg, Michel Godin, Scott M Knudsen, Wenjiang Shen, Greg Carlson, John S Foster, Ken Babcock, and Scott R Manalis. Weighing of biomolecules, single cells and single nanoparticles in fluid. *Nature*, 446(7139):1066–1069, 2007.

[19] A Suhel, BD Hauer, Tushar S Biswas, Kevin SD Beach, and John P Davis. Dissipation mechanisms in thermomechanically driven silicon nitride nanostrings. *Applied Physics Letters*, 100(17):173111, 2012.

[20] Marc J Madou. *Manufacturing techniques for microfabrication and nanotechnology*, volume 2. CRC Press, 2011.

[21] Bharat Bhushan. *Springer handbook of nanotechnology*. Springer Science & Business Media, 2010.

[22] Stephen A Campbell. *Fabrication engineering at the micro and nanoscale*, volume 4. Oxford University Press New York, 2008.

[23] Adam Hulanicki, Stanislav Glab, and Folke Ingman. Chemical sensors: definitions and classification. *Pure and Applied Chemistry*, 63(9):1247–1250, 1991.

[24] Gerd Binnig, Calvin F Quate, and Ch Gerber. Atomic force microscope. *Physical Review Letters*, 56(9):930, 1986.

[25] Thomas Thundat, R Js Warmack, GY Chen, and DP Allison. Thermal and ambient-induced deflections of scanning force microscope cantilevers. *Applied Physics Letters*, 64(21):2894–2896, 1994.

[26] T Thundat, EA Wachter, SL Sharp, and RJ Warmack. Detection of mercury vapor using resonating microcantilevers. *Applied Physics Letters*, 66(13):1695–1697, 1995.

[27] Karolyn M Hansen and Thomas Thundat. Microcantilever biosensors. *Methods*, 37(1):57–64, 2005.

[28] Hai-Feng Ji, Hongyan Gao, Koutilya R Buchapudi, Xin Yang, Xiaohe Xu, and Marvin K Schulte. Microcantilever biosensors based on conformational change of proteins. *Analyst*, 133(4):434–443, 2008.

[29] Koutilya R Buchapudi, Xin Huang, Xin Yang, Hai-Feng Ji, and Thomas Thundat. Microcantilever biosensors for chemicals and bioorganisms. *Analyst*, 136(8):1539–1556, 2011.

[30] G Gerald Stoney. The tension of metallic films deposited by electrolysis. *Proceedings of the Royal Society of London. Series A, Containing Papers of a Mathematical and Physical Character*, 82(553):172–175, 1909.

[31] Natalija Backmann, Christian Zahnd, Francois Huber, Alexander Bietsch, Andreas Plückthun, Hans-Peter Lang, Hans-Joachim Güntherodt, Martin Hegner, and Christoph Gerber. A label-free immunosensor array using single-chain antibody fragments. *Proceedings of the National Academy of Sciences of the United States of America*, 102(41):14587–14592, 2005.

[32] Johann Mertens, Celia Rogero, Montserrat Calleja, Daniel Ramos, Jose Angel Martín-Gago, Carlos Briones, and Javier Tamayo. Label-free detection of dna hybridization based on hydration-induced tension in nucleic acid films. *Nature Nanotechnology*, 3(5):301–307, 2008.

[33] Michael Sepaniak, Panos Datskos, Nickolay Lavrik, and Christopher Tipple. Peer reviewed: microcantilever transducers: a new approach in sensor technology. *Analytical Chemistry*, 74(21):568–A, 2002.

[34] YT Yang, Carlo Callegari, XL Feng, KL Ekinci, and ML Roukes. Zeptogram-scale nanomechanical mass sensing. *Nano Letters*, 6(4):583–586, 2006.

[35] Thomas Peter Burg and Scott R Manalis. Suspended microchannel resonators for biomolecular detection. *Applied Physics Letters*, 83(13):2698–2700, 2003.

[36] William Weaver Jr, Stephen P Timoshenko, and Donovan Harold Young. *Vibration problems in engineering*. John Wiley & Sons, 1990.

[37] Silvan Schmid. *Electrostatically Actuated All-Polymer Microbeam Resonators-Characterization and Application*. PhD thesis, Citeseer, 2009.

[38] Tushar S Biswas, Abdul Suhel, Bradley D Hauer, Alberto Palomino, Kevin SD Beach, and John P Davis. High-q gold and silicon nitride bilayer nanostrings. *Applied Physics Letters*, 101(9):093105, 2012.

[39] Scott S Verbridge, Jeevak M Parpia, Robert B Reichenbach, Leon M Bellan, and HG Craighead. High quality factor resonance at room temperature with nanostrings under high tensile stress. *Journal of Applied Physics*, 99(12):124304, 2006.

[40] Scott S Verbridge, Daniel Finkelstein Shapiro, Harold G Craighead, and Jeevak M Parpia. Macroscopic tuning of nanomechanics: substrate bending for reversible control of frequency and quality factor of nanostring resonators. *Nano Letters*, 7(6):1728–1735, 2007.

[41] AK Naik, MS Hanay, WK Hiebert, XL Feng, and ML Roukes. Towards single-molecule nanomechanical mass spectrometry. *Nature Nanotechnology*, 4(7):445–450, 2009.

[42] Silvan Schmid, Søren Dohn, and Anja Boisen. Real-time particle mass spectrometry based on resonant micro strings. *Sensors*, 10(9):8092–8100, 2010.

[43] Tom Larsen, Silvan Schmid, L Grönberg, AO Niskanen, J Hassel, Søren Dohn, and Anja Boisen. Ultrasensitive string-based temperature sensors. *Applied Physics Letters*, 98(12):121901, 2011.

[44] Sanjukta Bose, Silvan Schmid, Tom Larsen, Stephan S Keller, Peter Sommer-Larsen, Anja Boisen, and Kristoffer Almdal. Micromechanical string resonators: analytical tool for thermal characterization of polymers. *ACS Macro Letters*, 3(1):55–58, 2013.

[45] Alicia Johansson, Montserrat Calleja, PA Rasmussen, and Anja Boisen. Su-8 cantilever sensor system with integrated readout. *Sensors and Actuators A: Physical*, 123:111–115, 2005.

[46] Qiang Zhao, Qing Zhu, Wan Y Shih, and Wei-Heng Shih. Array adsorbent-coated lead zirconate titanate (pzt)/stainless steel cantilevers for dimethyl methylphosphonate (dmmp) detection. *Sensors and Actuators B: Chemical*, 117(1):74–79, 2006.

[47] C Grogan, R Raiteri, GM O'Connor, TJ Glynn, V Cunningham, M Kane, M Charlton, and D Leech. Characterisation of an antibody coated microcantilever as a potential immuno-based biosensor. *Biosensors and Bioelectronics*, 17(3):201–207, 2002.

[48] GY Chen, T Thundat, EA Wachter, and RJ Warmack. Adsorption-induced surface stress and its effects on resonance frequency of microcantilevers. *Journal of Applied Physics*, 77(8):3618–3622, 1995.

[49] Thomas Thundat, GY Chen, RJ Warmack, DP Allison, and EA Wachter. Vapor detection using resonating microcantilevers. *Analytical Chemistry*, 67(3):519–521, 1995.

[50] Y-H Lin, Michael E McConney, Melburne C LeMieux, Sergiy Peleshanko, Chaoyang Jiang, Srikanth Singamaneni, and Vladimir V Tsukruk. Trilayered ceramic–metal–polymer microcantilevers with dramatically enhanced thermal sensitivity. *Advanced Materials*, 18(9):1157–1161, 2006.

[51] Melburne C LeMieux, Michael E McConney, Yen-Hsi Lin, Srikanth Singamaneni, Hao Jiang, Timothy J Bunning, and Vladimir V Tsukruk. Polymeric nanolayers as actuators for ultrasensitive thermal bimorphs. *Nano Letters*, 6(4):730–734, 2006.

[52] Mo Li, Hong X Tang, and Michael L Roukes. Ultra-sensitive nems-based cantilevers for sensing, scanned probe and very high-frequency applications. *Nature Nanotechnology*, 2(2):114–120, 2007.

[53] Hai-Feng Ji, Eric Finot, Reza Dabestani, Thomas Thundat, Gilbert M Brown, and Phillip F Britt. A novel self-assembled monolayer (sam) coated microcantilever for low level caesium detection. *Chemical Communications*, (6):457–458, 2000.

[54] Hai-Feng Ji, Thomas Thundat, Reza Dabestani, Gilbert M Brown, Philip F Britt, and Peter V Bonnesen. Ultrasensitive detection of cro42-using a microcantilever sensor. *Analytical Chemistry*, 73(7):1572–1576, 2001.

[55] Guomin Zuo, Xinxin Li, Peng Li, Tiantian Yang, Yuelin Wang, Zhenxing Cheng, and Songlin Feng. Detection of trace organophosphorus vapor with a self-assembled bilayer functionalized sio 2 microcantilever piezoresistive sensor. *Analytica Chimica Acta*, 580(2):123–127, 2006.

[56] Digvijay Raorane, Srinath Satyanarayana, Arunava Majumdar, et al. Nano-chemo-mechanical sensor array platform for high-throughput chemical analysis. *Sensors and Actuators B: Chemical*, 119(2):466–474, 2006.

[57] Alexander Bietsch, Jiayun Zhang, Martin Hegner, Hans Peter Lang, and Christoph Gerber. Rapid functionalization of cantilever array sensors by inkjet printing. *Nanotechnology*, 15(8):873, 2004.

[58] Alexander Bietsch, Martin Hegner, Hans Peter Lang, and Christoph Gerber. Inkjet deposition of alkanethiolate monolayers and dna oligonucleotides on gold: Evaluation of spot uniformity by wet etching. *Langmuir*, 20(12):5119–5122, 2004.

[59] Chunguang Jin and Edward T Zellers. Limits of recognition for binary and ternary vapor mixtures determined with multitransducer arrays. *Analytical Chemistry*, 80(19):7283–7293, 2008.

[60] Weichang Zhao, Lal A Pinnaduwage, John W Leis, Anthony C Gehl, Steve L Allman, Allan Shepp, and Ken K Mahmud. Identification and quantification of components

in ternary vapor mixtures using a microelectromechanical-system-based electronic nose. *Journal of Applied Physics*, 103(10):104902, 2008.

[61] E Bright Wilson, John Courtney Decius, and Paul C Cross. *Molecular vibrations: the theory of infrared and Raman vibrational spectra*. Courier Corporation, 2012.

[62] Stephen Bialkowski. *Photothermal spectroscopy methods for chemical analysis*, volume 134. John Wiley & Sons, 1996.

[63] Allan Rosencwaig and Allen Gersho. Theory of the photoacoustic effect with solids. *Journal of Applied Physics*, 47(1):64–69, 1976.

[64] Andrew C Tam. Applications of photoacoustic sensing techniques. *Reviews of Modern Physics*, 58(2):381, 1986.

[65] H Coufal. Photothermal spectroscopy using a pyroelectric thin-film detector. *Applied Physics Letters*, 44(1):59–61, 1984.

[66] Zafer A Yasa, Warren B Jackson, and Nabil M Amer. Photothermal spectroscopy of scattering media. *Applied optics*, 21(1):21–31, 1982.

[67] JR Barnes, RJ Stephenson, CN Woodburn, SJ O'shea, ME Welland, T Rayment, JK Gimzewski, and Ch Gerber. A femtojoule calorimeter using micromechanical sensors. *Review of Scientific Instruments*, 65(12):3793–3798, 1994.

[68] I Galaxy. Photothermal spectroscopy with femtojoule sensitivity using a micromechanical device. *Nature*, 372:3, 1994.

[69] LR Senesac, JL Corbeil, S Rajic, NV Lavrik, and PG Datskos. Ir imaging using uncooled microcantilever detectors. *Ultramicroscopy*, 97(1):451–458, 2003.

[70] D Grbovic, NV Lavrik, PG Datskos, D Forrai, E Nelson, J Devitt, and B McIntyre. Uncooled infrared imaging using bimaterial microcantilever arrays. *Applied Physics Letters*, 89(7):073118, 2006.

[71] PG Datskos, NV Lavrik, and S Rajic. Performance of uncooled microcantilever thermal detectors. *Review of Scientific Instruments*, 75(4):1134–1148, 2004.

[72] A Majumdar, JP Carrejo, and J Lai. Thermal imaging using the atomic force microscope. *Applied Physics Letters*, 62(20):2501–2503, 1993.

[73] Yanan Yue and Xinwei Wang. Nanoscale thermal probing. *Nano Reviews*, 3, 2012.

[74] J Varesi, J Lai, T Perazzo, Z Shi, and A Majumdar. Photothermal measurements at picowatt resolution using uncooled micro-optomechanical sensors. *Applied physics letters*, 71(3):306–308, 1997.

[75] Beomjin Kwon, C Wang, K Park, R Bhargava, and WP King. Thermomechanical sensitivity of microcantilevers in the mid-infrared spectral region. *Nanoscale and Microscale Thermophysical Engineering*, 15(1):16–27, 2011.

[76] Arvind Narayanaswamy and Ning Gu. Thermal characterization of bi-material microcantilevers: Thermal conductance and microscale convection. In *ASME 2009 Heat Transfer Summer Conference collocated with the InterPACK09 and 3rd Energy Sustainability Conferences*, pages 793–800. American Society of Mechanical Engineers, 2009.

[77] Beomjin Kwon, Matthew Rosenberger, Rohit Bhargava, David G Cahill, and William P King. Dynamic thermomechanical response of bimaterial microcantilevers to periodic heating by infrared radiation. *Review of Scientific Instruments*, 83(1):015003, 2012.

[78] J Lai, T Perazzo, Z Shi, and A Majumdar. Optimization and performance of high-resolution micro-optomechanical thermal sensors. *Sensors and Actuators A: Physical*, 58(2):113–119, 1997.

[79] EA Wachter, T Thundat, PI Oden, RJ Warmack, PG Datskos, and SL Sharp. Remote optical detection using microcantilevers. *Review of Scientific Instruments*, 67(10):3434–3439, 1996.

[80] PI Oden, PG Datskos, T Thundat, and RJ Warmack. Uncooled thermal imaging using a piezoresistive microcantilever. *Applied Physics Letters*, 69(21):3277–3279, 1996.

[81] Matthew R Rosenberger, Beomjin Kwon, David G Cahill, and William P King. Impact of silicon nitride thickness on the infrared sensitivity of silicon nitride–aluminum microcantilevers. *Sensors and Actuators A: Physical*, 185:17–23, 2012.

[82] T Perazzo, M Mao, O Kwon, A Majumdar, JB Varesi, and P Norton. Infrared vision using uncooled micro-optomechanical camera. *Applied Physics Letters*, 74(23):3567–3569, 1999.

[83] Sheng Shen, Arvind Narayanaswamy, Shireen Goh, and Gang Chen. Thermal conductance of bimaterial microcantilevers. *Applied Physics Letters*, 92(6):063509, 2008.

[84] Tom Larsen, Anja Boisen, and Silvan Schmid. *Micro-Mechanical Temperature Sensors*. PhD thesis, Technical University of DenmarkDanmarks Tekniske Universitet, Department of Micro-and NanotechnologyInstitut for Mikro-og Nanoteknologi, NanoprobesNanoprobes, 2012.

[85] John G Webster and Halit Eren. *Measurement, Instrumentation, and Sensors Handbook: Spatial, Mechanical, Thermal, and Radiation Measurement*, volume 1. CRC press, 2014.

[86] Seid Sadat, Yi Jie Chua, Woochul Lee, Yashar Ganjeh, Katsuo Kurabayashi, Edgar Meyhofer, and Pramod Reddy. Room temperature picowatt-resolution calorimetry. *Applied Physics Letters*, 99(4):043106, 2011.

[87] JK Gimzewski, Ch Gerber, E Meyer, and RR Schlittler. Observation of a chemical reaction using a micromechanical sensor. *Chemical Physics Letters*, 217(5):589–594, 1994.

[88] A Wig, Edward T Arakawa, Ali Passian, Thomas L Ferrell, and T Thundat. Photothermal spectroscopy of bacillus anthracis and bacillus cereus with microcantilevers. *Sensors and Actuators B: Chemical*, 114(1):206–211, 2006.

[89] Guangming Li, Larry W Burggraf, and William P Baker. Photothermal spectroscopy using multilayer cantilever for chemical detection. *Applied Physics Letters*, 76:1122, 2000.

[90] Edward T Arakawa, Nickolay V Lavrik, and Panos G Datskos. Detection of anthrax simulants with microcalorimetric spectroscopy: Bacillus subtilis and bacillus cereus spores. *Applied optics*, 42(10):1757–1762, 2003.

[91] ET Arakawa, NV Lavrik, S Rajic, and PG Datskos. Detection and differentiation of biological species using microcalorimetric spectroscopy. *Ultramicroscopy*, 97(1):459–465, 2003.

[92] Dongkyu Lee, Seonghwan Kim, and Thomas Thundat. Detection of biological analytes using nanomechanical infrared spectroscopy with a nanoporous microcantilever. In *Nano-Bio Sensing, Imaging and Spectroscopy*, pages 88790Q–88790Q. International Society for Optics and Photonics, 2013.

[93] PG Datskos, NV Lavrik, and MJ Sepaniak. Chemical and biological sensors based on microcantilevers. In *Smart sensors and MEMS*, pages 331–379. Springer, 2004.

[94] PG Datskos, MJ Sepaniak, CA Tipple, and N Lavrik. Photomechanical chemical microsensors. *Sensors and Actuators B: Chemical*, 76(1):393–402, 2001.

[95] Charles W Van Neste, Marissa E Morales-Rodríguez, Larry R Senesac, Satish M Mahajan, and Thomas Thundat. Quartz crystal tuning fork photoacoustic point sensing. *Sensors and Actuators B: Chemical*, 150(1):402–405, 2010.

[96] Charles W Van Neste, Larry R Senesac, and T Thundat. Standoff photoacoustic spectroscopy. *Applied Physics Letters*, 92(23):234102, 2008.

[97] Dongkyu Lee, Seonghwan Kim, Inseok Chae, Sangmin Jeon, and Thomas Thundat. Nanowell-patterned TiO_2 microcantilevers for calorimetric chemical sensing. *Applied Physics Letters*, 104(14):141903, 2014.

[98] Dongkyu Lee, Seonghwan Kim, Sangmin Jeon, and Thomas Thundat. Direct detection and speciation of trace explosives using a nanoporous multifunctional microcantilever. *Analytical Chemistry*, 86(10):5077–5082, 2014.

[99] Minhyuk Yun, Seonghwan Kim, Dongkyu Lee, Namchul Jung, Inseok Chae, Sangmin Jeon, and Thomas Thundat. Photothermal cantilever deflection spectroscopy of a photosensitive polymer. *Applied Physics Letters*, 100(20):204103, 2012.

[100] Mehrdad Bagheri, Inseok Chae, Dongkyu Lee, Seonghwan Kim, and Thomas Thundat. Selective detection of physisorbed hydrocarbons using photothermal cantilever deflection spectroscopy. *Sensors and Actuators B: Chemical*, 191:765–769, 2014.

[101] Dongkyu Lee, Kyo Seon Hwang, Seonghwan Kim, and Thomas Thundat. Rapid discrimination of dna strands using an opto-calorimetric microcantilever sensor. *Lab on a Chip*, 14(24):4659–4664, 2014.

[102] TS Biswas, N Miriyala, C Doolin, X Liu, T Thundat, and JP Davis. Femtogram-scale photothermal spectroscopy of explosive molecules on nanostrings. *Analytical Chemistry*, 86(22):11368–11372, 2014.

[103] M Faheem Khan, Seonghwan Kim, Dongkyu Lee, Silvan Schmid, Anja Boisen, and Thomas Thundat. Nanomechanical identification of liquid reagents in a microfluidic channel. *Lab on a Chip*, 14(7):1302–1307, 2014.

[104] Tom Larsen, Silvan Schmid, Luis G Villanueva, and Anja Boisen. Photothermal analysis of individual nanoparticulate samples using micromechanical resonators. *ACS nano*, 7(7):6188–6193, 2013.

[105] Shoko Yamada, Silvan Schmid, Tom Larsen, Ole Hansen, and Anja Boisen. Photothermal infrared spectroscopy of airborne samples with mechanical string resonators. *Analytical Chemistry*, 85(21):10531–10535, 2013.

[106] Silvan Schmid, Kaiyu Wu, Peter Emil Larsen, Tomas Rindzevicius, and Anja Boisen. Low-power photothermal probing of single plasmonic nanostructures with nanomechanical string resonators. *Nano Letters*, 14(5):2318–2321, 2014.

[107] Marin Alexe and Dietrich Hesse. Tip-enhanced photovoltaic effects in bismuth ferrite. *Nature Communications*, 2:256, 2011.

[108] Feng Gao, Y Yuan, KF Wang, XY Chen, F Chen, JM Liu, and ZF Ren. Preparation and photoabsorption characterization of $BiFeO_3$ nanowires. *Applied Physics Letters*, 89(10):102506–102900, 2006.

[109] Kuibo Yin, Mi Li, Yiwei Liu, Congli He, Fei Zhuge, Bin Chen, Wei Lu, Xiaoqing Pan, and Run-Wei Li. Resistance switching in polycrystalline $BiFeO_3$ thin films. *Appl. Phys. Lett*, 97(042101):3pp, 2010.

[110] Sheng Ju and Tian-Yi Cai. First-principles studies of the effect of oxygen vacancies on the electronic structure and linear optical response of multiferroic $BiFeO_3$. *Applied Physics Letters*, 95(23):231906, 2009.

[111] Gustau Catalan, J Seidel, R Ramesh, and James F Scott. Domain wall nanoelectronics. *Reviews of Modern Physics*, 84(1):119, 2012.

[112] K Ahadi, SM Mahdavi, A Nemati, and M Kianinia. Photoconductivity and diode effect in bi rich multiferroic $BiFeO_3$ thin films grown by pulsed-laser deposition. *Journal of Materials Science: Materials in Electronics*, 22(7):815–820, 2011.

[113] T Choi, S Lee, YJ Choi, V Kiryukhin, and S-W Cheong. Switchable ferroelectric diode and photovoltaic effect in $BiFeO_3$. *Science*, 324(5923):63–66, 2009.

[114] K Prashanthi, G Thakur, and T Thundat. Surface enhanced strong visible photoluminescence from one-dimensional multiferroic $BiFeO_3$ nanostructures. *Surface Science*, 606(19):L83–L86, 2012.

[115] Kovur Prashanthi, Ravi Gaikwad, and Thomas Thundat. Surface dominant photoresponse of multiferroic $BiFeO_3$ nanowires under sub-bandgap illumination. *Nanotechnology*, 24(50):505710, 2013.

[116] Kovur Prashanthi, Arindam Phani, and Thomas Thundat. Photothermal electrical resonance spectroscopy of physisorbed molecules on a nanowire resonator. *Nano Letters*, 15(8):5658–5663, 2015.

[117] PG Datskos, PI Oden, T Thundat, EA Wachter, RJ Warmack, and SR Hunter. Remote infrared radiation detection using piezoresistive microcantilevers. *Applied Physics Letters*, 69(20):2986–2988, 1996.

[118] Javier Tamayo, ADL Humphris, AM Malloy, and MJ Miles. Chemical sensors and biosensors in liquid environment based on microcantilevers with amplified quality factor. *Ultramicroscopy*, 86(1):167–173, 2001.

[119] Thomas P Burg, Amir R Mirza, Nebojsa Milovic, Christine H Tsau, George Popescu, John S Foster, Scott R Manalis, et al. Vacuum-packaged suspended microchannel resonant mass sensor for biomolecular detection. *Microelectromechanical Systems, Journal of*, 15(6):1466–1476, 2006.

[120] Jungchul Lee, Wenjiang Shen, Kris Payer, Thomas P Burg, and Scott R Manalis. Toward attogram mass measurements in solution with suspended nanochannel resonators. *Nano Letters*, 10(7):2537–2542, 2010.

[121] Marcio G von Muhlen, Norman D Brault, Scott M Knudsen, Shaoyi Jiang, and Scott R Manalis. Label-free biomarker sensing in undiluted serum with suspended microchannel resonators. *Analytical Chemistry*, 82(5):1905–1910, 2010.

[122] Andrea K Bryan, Vivian C Hecht, Wenjiang Shen, Kristofor Payer, William H Grover, and Scott R Manalis. Measuring single cell mass, volume, and density with dual suspended microchannel resonators. *Lab on a chip*, 14(3):569–576, 2014.

[123] Selim Olcum, Nathan Cermak, Steven C Wasserman, Kathleen S Christine, Hiroshi Atsumi, Kris R Payer, Wenjiang Shen, Jungchul Lee, Angela M Belcher, Sangeeta N Bhatia, et al. Weighing nanoparticles in solution at the attogram scale. *Proceedings of the National Academy of Sciences*, 111(4):1310–1315, 2014.

[124] MF Khan, Silvan Schmid, Peter Emil Larsen, Zachary James Davis, Wei Yan, Erling Halfdan Stenby, and Anja Boisen. Online measurement of mass density and viscosity of pl fluid samples with suspended microchannel resonator. *Sensors and Actuators B: Chemical*, 185:456–461, 2013.

[125] MF Khan, Silvan Schmid, Zachary James Davis, Søren Dohn, and Anja Boisen. Fabrication of resonant micro cantilevers with integrated transparent fluidic channel. *Microelectronic Engineering*, 88(8):2300–2303, 2011.

[126] D Ramos, Johann Mertens, M Calleja, and J Tamayo. Phototermal self-excitation of nanomechanical resonators in liquids. *Applied physics letters*, 92(17):173108, 2008.

[127] Yang Zhao, Minyao Mao, Roberto Horowitz, Arunava Majumdar, John Varesi, Paul Norton, and John Kitching. Optomechanical uncooled infrared imaging system: design, microfabrication, and performance. *Microelectromechanical Systems, Journal of*, 11(2):136–146, 2002.

[128] Irina Doroshenko, Valeriy Pogorelov, and Valdas Sablinskas. Infrared absorption spectra of monohydric alcohols. *Dataset Papers in Science*, 2013, 2012.

[129] Scott T Huxtable, David G Cahill, Sergei Shenogin, Liping Xue, Rahmi Ozisik, Paul Barone, Monica Usrey, Michael S Strano, Giles Siddons, Moonsub Shim, et al. Interfacial heat flow in carbon nanotube suspensions. *Nature Materials*, 2(11):731–734, 2003.

[130] Orla M Wilson, Xiaoyuan Hu, David G Cahill, and Paul V Braun. Colloidal metal particles as probes of nanoscale thermal transport in fluids. *Physical Review B*, 66(22):224301, 2002.

[131] Anna J Tüdős, Geert AJ Besselink, and Richard BM Schasfoort. Trends in miniaturized total analysis systems for point-of-care testing in clinical chemistry. *Lab on a Chip*, 1(2):83–95, 2001.

[132] Inhee Choi, Yun Suk Huh, and David Erickson. Size-selective concentration and label-free characterization of protein aggregates using a raman active nanofluidic device. *Lab on a Chip*, 11(4):632–638, 2011.

[133] Zhenbin Ge, David G Cahill, and Paul V Braun. Aupd metal nanoparticles as probes of nanoscale thermal transport in aqueous solution. *The Journal of Physical Chemistry B*, 108(49):18870–18875, 2004.

[134] Y Nagasaka and A Nagashima. Simultaneous measurement of the thermal conductivity and the thermal diffusivity of liquids by the transient hot-wire method. *Review of Scientific Instruments*, 52(2):229–232, 1981.

[135] Yuji Nagasaka, T Hatakeyama, M Okuda, and A Nagashima. Measurement of the thermal diffusivity of liquids by the forced rayleigh scattering method: Theory and experiment. *Review of Scientific Instruments*, 59(7):1156–1168, 1988.

[136] B Håkansson, P Andersson, and G Bäckström. Improved hot-wire procedure for thermophysical measurements under pressure. *Review of scientific instruments*, 59(10):2269–2275, 1988.

[137] Ki-Yeol Shin, Sang-Baik Kim, Jong-Hwan Kim, Mo Chung, and Pyung-Suk Jung. Thermo-physical properties and transient heat transfer of concrete at elevated temperatures. *Nuclear Engineering and Design*, 212(1):233–241, 2002.

[138] Huaqing Xie, Hua Gu, Motoo Fujii, and Xing Zhang. Short hot wire technique for measuring thermal conductivity and thermal diffusivity of various materials. *Measurement Science and Technology*, 17(1):208, 2006.

[139] JA Palacios, JJ Alvarado-Gil, et al. Determination of the thermophysical properties of polymers (pet) using photoacoustic spectroscopy. *Journal of materials science*, 34(9):2113–2119, 1999.

[140] KH Michaelian, RH Hall, and J Tim Bulmer. Photoacoustic infrared spectroscopy and thermophysical properties of syncrude cokes. *Journal of thermal analysis and calorimetry*, 69(1):135–147, 2002.

[141] Konrad Lukaszewski. Thermophysical properties of liquids examined with the photoacoustic method. In *Laser Technology VII: Applications of Lasers*, pages 344–347. International Society for Optics and Photonics, 2003.

[142] H Vargas and LCM Miranda. Photothermal techniques applied to thermophysical properties measurements (plenary). *Review of Scientific Instruments*, 74(1):794–799, 2003.

[143] Silas E Gustafsson and Ernest Karawacki. Transient hot-strip probe for measuring thermal properties of insulating solids and liquids. *Review of Scientific Instruments*, 54(6):744–747, 1983.

[144] Roman Beigelbeck, Herbert Nachtnebel, Franz Kohl, and Bernhard Jakoby. A novel measurement method for the thermal properties of liquids by utilizing a bridge-based micromachined sensor. *Measurement Science and Technology*, 22(10):105407, 2011.

[145] J Kuntner, F Kohl, and B Jakoby. Simultaneous thermal conductivity and diffusivity sensing in liquids using a micromachined device. *Sensors and Actuators A: Physical*, 130:62–67, 2006.

[146] Chen Wang, De-Kai Ye, Yun-Yi Wang, Tao Lu, and Xing-Hua Xia. Insights into the free state enzyme reaction kinetics in nanoconfinement. *Lab on a Chip*, 13(8):1546–1553, 2013.

[147] David G Cahill, Paul V Braun, Gang Chen, David R Clarke, Shanhui Fan, Kenneth E Goodson, Pawel Keblinski, William P King, Gerald D Mahan, Arun Majumdar, et al. Nanoscale thermal transport. ii. 2003–2012. *Applied Physics Reviews*, 1(1):011305, 2014.

[148] WA Wakeham, MA Assael, JK Atkinson, J Bilek, JMNA Fareleira, AD Fitt, ARH Goodwin, and CMBP Oliveira. Thermophysical property measurements: the journey from accuracy to fitness for purpose. *International journal of Thermophysics*, 28(2):372–416, 2007.

[149] Yaochung Weng, Francisco Feijó Delgado, Sungmin Son, Thomas P Burg, Steven C Wasserman, and Scott R Manalis. Mass sensors with mechanical traps for weighing single cells in different fluids. *Lab on a Chip*, 11(24):4174–4180, 2011.

[150] I Lee, K Park, and J Lee. Note: Precision viscosity measurement using suspended microchannel resonators. *Review of Scientific Instruments*, 83(11):116106, 2012.

[151] G Scardera, T Puzzer, G Conibeer, and MA Green. Fourier transform infrared spectroscopy of annealed silicon-rich silicon nitride thin films. *Journal of Applied Physics*, 104(10):104310, 2008.

[152] A Kayode Coker. *Ludwig's applied process design for chemical and petrochemical plants*, volume 1. Elsevier Gulf Professional Pub., 2007.

[153] Wonhee Lee, Warren Fon, Blake W Axelrod, and Michael L Roukes. High-sensitivity microfluidic calorimeters for biological and chemical applications. *Proceedings of the National Academy of Sciences*, 106(36):15225–15230, 2009.

[154] Luke MacQueen, Oleg Chebotarev, Craig A Simmons, and Yu Sun. Miniaturized platform with on-chip strain sensors for compression testing of arrayed materials. *Lab on a chip*, 12(20):4178–4184, 2012.

[155] TS Biswas, Jin Xu, X Rojas, C Doolin, A Suhel, KSD Beach, and JP Davis. Remote sensing in hybridized arrays of nanostrings. *Nano Letters*, 14(5):2541–2545, 2014.

[156] MJ Madou. Fundamentals of microfabrication-the science of miniaturization. second.

[157] Yong Kyoung Yoo, Myung-Sic Chae, Ji Yoon Kang, Tae Song Kim, Kyo Seon Hwang, and Jeong Hoon Lee. Multifunctionalized cantilever systems for electronic nose applications. *Analytical Chemistry*, 84(19):8240–8245, 2012.

[158] Mo Li, EB Myers, HX Tang, SJ Aldridge, HC McCaig, JJ Whiting, RJ Simonson, NS Lewis, and ML Roukes. Nanoelectromechanical resonator arrays for ultrafast, gas-phase chromatographic chemical analysis. *Nano Letters*, 10(10):3899–3903, 2010.

[159] Seonghwan Kim, Dongkyu Lee, and Thomas Thundat. Photothermal cantilever deflection spectroscopy. *EPJ Techniques and Instrumentation*, 1(1):1–12, 2014.

[160] Scott S Verbridge, Rob Ilic, HG Craighead, and Jeevak M Parpia. Size and frequency dependent gas damping of nanomechanical resonators. *Applied Physics Letters*, 93(1):013101, 2008.

[161] Silvan Schmid, KD Jensen, KH Nielsen, and Anja Boisen. Damping mechanisms in high-q micro and nanomechanical string resonators. *Physical Review B*, 84(16):165307, 2011.

[162] Jerome Faist, Federico Capasso, Deborah L Sivco, Carlo Sirtori, Albert L Hutchinson, and Alfred Y Cho. Quantum cascade laser. *Science*, 264(5158):553–556, 1994.

[163] Xunchen Liu, Charles W Van Neste, Manisha Gupta, Ying Y Tsui, Seonghwan Kim, and Thomas Thundat. Standoff reflection–absorption spectra of surface adsorbed explosives measured with pulsed quantum cascade lasers. *Sensors and Actuators B: Chemical*, 191:450–456, 2014.

[164] Sunwoo Lee, Vivekananda P Adiga, Robert A Barton, Arend M van der Zande, Gwan-Hyoung Lee, B Rob Ilic, Alexander Gondarenko, Jeevak M Parpia, Harold G Craighead, and James Hone. Graphene metallization of high-stress silicon nitride resonators for electrical integration. *Nano Letters*, 13(9):4275–4279, 2013.

[165] VP Adiga, R De Alba, IR Storch, PA Yu, B Ilic, RA Barton, S Lee, J Hone, PL McEuen, JM Parpia, et al. Simultaneous electrical and optical readout of graphene-coated high q silicon nitride resonators. *Applied Physics Letters*, 103(14):143103, 2013.

[166] MD LaHaye, J Suh, PM Echternach, KC Schwab, and ML Roukes. Nanomechanical measurements of a superconducting qubit. *Nature*, 459(7249):960–964, 2009.

[167] Emanuel Gavartin, Pierre Verlot, and Tobias J Kippenberg. A hybrid on-chip optomechanical transducer for ultrasensitive force measurements. *Nature Nanotechnology*, 7(8):509–514, 2012.

[168] Matthias Pernpeintner, Thomas Faust, Fredrik Hocke, Jörg Peter Kotthaus, Eva Maria Weig, Hans Huebl, and Rudolf Gross. Circuit electromechanics with a non-metallized nanobeam. *Applied Physics Letters*, 105(12):123106, 2014.

[169] C Doolin, PH Kim, BD Hauer, AJR MacDonald, and JP Davis. Multidimensional optomechanical cantilevers for high-frequency force sensing. *New Journal of Physics*, 16(3):035001, 2014.

[170] Thomas Faust, Peter Krenn, Stephan Manus, Jörg Peter Kotthaus, and Eva Maria Weig. Microwave cavity-enhanced transduction for plug and play nanomechanics at room temperature. *Nature Communications*, 3:728, 2012.

[171] James R Teague, Robert Gerson, and William Joseph James. Dielectric hysteresis in single crystal $BiFeO_3$. *Solid State Communications*, 8(13):1073–1074, 1970.

[172] JBNJ Wang, JB Neaton, H Zheng, V Nagarajan, SB Ogale, B Liu, D Viehland, V Vaithyanathan, DG Schlom, UV Waghmare, et al. Epitaxial $BiFeO_3$ multiferroic thin film heterostructures. *Science*, 299(5613):1719–1722, 2003.

[173] T Zhao, A Scholl, F Zavaliche, K Lee, M Barry, A Doran, MP Cruz, YH Chu, C Ederer, NA Spaldin, et al. Electrical control of antiferromagnetic domains in multiferroic $BiFeO_3$ films at room temperature. *Nature Materials*, 5(10):823–829, 2006.

[174] Tae-Jin Park, Georgia C Papaefthymiou, Arthur J Viescas, Arnold R Moodenbaugh, and Stanislaus S Wong. Size-dependent magnetic properties of single-crystalline multiferroic $BiFeO_3$ nanoparticles. *Nano Letters*, 7(3):766–772, 2007.

[175] B Kundys, M Viret, D Colson, and DO Kundys. Light-induced size changes in $BiFeO_3$ crystals. *Nature Materials*, 9(10):803–805, 2010.

[176] SY Yang, J Seidel, SJ Byrnes, P Shafer, C-H Yang, MD Rossell, P Yu, Y-H Chu, JF Scott, JW Ager, et al. Above-bandgap voltages from ferroelectric photovoltaic devices. *Nature Nanotechnology*, 5(2):143–147, 2010.

[177] JF Scott and Matthew Dawber. Oxygen-vacancy ordering as a fatigue mechanism in perovskite ferroelectrics. *Applied Physics Letters*, 76(25):3801–3803, 2000.

[178] Shun Li, Yuan-Hua Lin, Bo-Ping Zhang, Ce-Wen Nan, Yao Wang, et al. Photocatalytic and magnetic behaviors observed in nanostructured $BiFeO_3$ particles. *Journal of Applied Physics*, 105(5):56105, 2009.

[179] Shun Li, Yuan-Hua Lin, Bo-Ping Zhang, Yao Wang, and Ce-Wen Nan. Controlled fabrication of $BiFeO_3$ uniform microcrystals and their magnetic and photocatalytic behaviors. *The Journal of Physical Chemistry C*, 114(7):2903–2908, 2010.

[180] SH Xie, JY Li, Roger Proksch, YM Liu, YC Zhou, YY Liu, Y Ou, LN Lan, Y Qiao, et al. Nanocrystalline multiferroic $BiFeO_3$ ultrafine fibers by sol-gel based electrospinning. *Applied Physics Letters*, 93(22):222904, 2008.

[181] K Prashanthi, PM Shaibani, A Sohrabi, TS Natarajan, and T Thundat. Nanoscale magnetoelectric coupling in multiferroic $BiFeO_3$ nanowires. *physica status solidi (RRL)-Rapid Research Letters*, 6(6):244–246, 2012.

[182] Feng Gao, XY Chen, KB Yin, Shuai Dong, ZF Ren, Fang Yuan, Tao Yu, ZG Zou, Jun-Ming Liu, et al. Visible-light photocatalytic properties of weak magnetic $BiFeO_3$ nanoparticles. *Advanced Materials*, 19(19):2889, 2007.

[183] Shun Li, Jianming Zhang, Md Golam Kibria, Zetian Mi, Mohamed Chaker, Dongling Ma, Riad Nechache, and Federico Rosei. Remarkably enhanced photocatalytic activity of laser ablated au nanoparticle decorated $BiFeO_3$ nanowires under visible-light. *Chemical Communications*, 49(52):5856–5858, 2013.

[184] AB Djurišić, YH Leung, KH Tam, YF Hsu, L Ding, WK Ge, YC Zhong, KS Wong, WK Chan, HL Tam, et al. Defect emissions in zno nanostructures. *Nanotechnology*, 18(9):095702, 2007.

[185] Amy L Linsebigler, Guangquan Lu, and John T Yates Jr. Photocatalysis on TiO_2 surfaces: principles, mechanisms, and selected results. *Chemical Reviews*, 95(3):735–758, 1995.

[186] Yuning Huo, Yi Jin, and Ya Zhang. Citric acid assisted solvothermal synthesis of $BiFeO_3$ microspheres with high visible-light photocatalytic activity. *Journal of Molecular Catalysis A: Chemical*, 331(1):15–20, 2010.

[187] Jinyi Deng, Subarna Banerjee, Susanta K Mohapatra, York R Smith, and Mano Misra. Bismuth iron oxide nanoparticles as photocatalyst for solar hydrogen generation from water. *Journal of Fundamentals of Renewable Energy and Applications*, 1:1–10, 2011.

[188] Wei Luo, Lihua Zhu, Nan Wang, Heqing Tang, Meijuan Cao, and Yuanbin She. Efficient removal of organic pollutants with magnetic nanoscaled $BiFeO_3$ as a reusable heterogeneous fenton-like catalyst. *Environmental Science & Technology*, 44(5):1786–1791, 2010.

[189] Shun Li, Yuan-Hua Lin, Bo-Ping Zhang, Jing-Feng Li, Ce-Wen Nan, et al. $BiFeO_3/TiO_2$ core-shell structured nanocomposites as visible-active photocatalysts and their optical response mechanism. *Journal of Applied Physics*, 105(5):54310, 2009.

[190] Yuning Huo, Miao Miao, Yi Zhang, Jian Zhu, and Hexing Li. Aerosol-spraying preparation of a mesoporous hollow spherical $BiFeO_3$ visible photocatalyst with enhanced activity and durability. *Chemical Communications*, 47(7):2089–2091, 2011.

[191] Kazuya Nakata, Tsuyoshi Ochiai, Taketoshi Murakami, and Akira Fujishima. Photoenergy conversion with TiO_2 photocatalysis: new materials and recent applications. *Electrochimica Acta*, 84:103–111, 2012.

[192] Jie Wei, Desheng Xue, and Yan Xu. Photoabsorption characterization and magnetic property of multiferroic $BiFeO_3$ nanotubes synthesized by a facile sol–gel template process. *Scripta Materialia*, 58(1):45–48, 2008.

[193] Xingyan Wang, Xianyou Wang, Weiguo Huang, PJ Sebastian, and Sergio Gamboa. Sol–gel template synthesis of highly ordered MnO_2 nanowire arrays. *Journal of Power Sources*, 140(1):211–215, 2005.

[194] Brinda B Lakshmi, Peter K Dorhout, and Charles R Martin. Sol-gel template synthesis of semiconductor nanostructures. *Chemistry of Materials*, 9(3):857–862, 1997.

[195] Bernadette A Hernandez, Ki-Seog Chang, Ellen R Fisher, and Peter K Dorhout. Sol-gel template synthesis and characterization of $BaTiO_3$ and $PbTiO_3$ nanotubes. *Chemistry of Materials*, 14(2):480–482, 2002.

[196] Ming Liu, Xin Li, Hassan Imrane, Yajie Chen, Trevor Goodrich, Zhuhua Cai, Katherine S Ziemer, Jian Y Huang, and Nian X Sun. Synthesis of ordered arrays of multiferroic $NiFe_2O_4$-Pb (Zr0. $_{52}$Ti0. $_{48}$) O_3 core-shell nanowires. *Applied physics letters*, 90(15):152501, 2007.

[197] XY Zhang, CW Lai, X Zhao, DY Wang, and Jiyan Dai. Synthesis and ferroelectric properties of multiferroic $BiFeO_3$ nanotube arrays. *Applied Physics Letters*, 87(14):1–3, 2005.

[198] Nirupam Banerjee and Saluru Baba Krupanidhi. Synthesis, structural characterization and formation mechanism of giant-dielectric $CaCu_3Ti_4O_12$ nanotubes. *Natural Science*, 2(07):688, 2010.

[199] Bipin KumaráGupta et al. Probing the highly efficient room temperature ammonia gas sensing properties of a luminescent ZnO nanowire array prepared via an aao-assisted template route. *Dalton Transactions*, 43(15):5713–5720, 2014.

[200] GS Wu, T Xie, XY Yuan, Y Li, L Yang, YH Xiao, and LD Zhang. Controlled synthesis of zno nanowires or nanotubes via sol–gel template process. *Solid State Communications*, 134(7):485–489, 2005.

[201] Ming Zhang, Y Bando, and K Wada. Sol-gel template preparation of TiO_2 nanotubes and nanorods. *Journal of materials science letters*, 20(2):167–170, 2001.

[202] Xiong Wang, Ying Lin, Xifeng Ding, and Jinguo Jiang. Enhanced visible-light-response photocatalytic activity of bismuth ferrite nanoparticles. *Journal of Alloys and Compounds*, 509(23):6585–6588, 2011.

[203] T Fujii, FMF De Groot, GA Sawatzky, FC Voogt, T Hibma, and K Okada. In situ XPS analysis of various iron oxide films grown by NO_2-assisted molecular-beam epitaxy. *Physical Review B*, 59(4):3195–3202, 2001.

[204] Sakar Mohan, Balakumar Subramanian, and Ganesamoorthy Sarveswaran. A prototypical development of plasmonic multiferroic bismuth ferrite particulate and fiber nanostructures and their remarkable photocatalytic activity under sunlight. *Journal of Materials Chemistry C*, 2(33):6835–6842, 2014.

[205] I Sosnowska, T Peterlin Neumaier, and E Steichele. Spiral magnetic ordering in bismuth ferrite. *Journal of Physics C: Solid State Physics*, 15(23):4835, 1982.

[206] Renqing Guo, Liang Fang, Wen Dong, Fengang Zheng, and Mingrong Shen. Enhanced photocatalytic activity and ferromagnetism in gd doped $BiFeO_3$ nanoparticles. *The Journal of Physical Chemistry C*, 114(49):21390–21396, 2010.

[207] Tayyebe Soltani and Mohammad H Entezari. Sono-synthesis of bismuth ferrite nanoparticles with high photocatalytic activity in degradation of rhodamine b under solar light irradiation. *Chemical Engineering Journal*, 223:145–154, 2013.

[208] Yinyan Gong, Tamar Andelman, Gertrude F Neumark, Stephen O'Brien, and Igor L Kuskovsky. Origin of defect-related green emission from zno nanoparticles: effect of surface modification. *Nanoscale Research Letters*, 2(6):297–302, 2007.

[209] Dillip K Mishra and Xiaoding Qi. Energy levels and photoluminescence properties of nickel-doped bismuth ferrite. *Journal of Alloys and Compounds*, 504(1):27–31, 2010.

[210] B Ramachandran, A Dixit, R Naik, G Lawes, and MS Ramachandra Rao. Charge transfer and electronic transitions in polycrystalline $BiFeO_3$. *Physical Review B*, 82(1):012102, 2010.

[211] AJ Hauser, J Zhang, L Mier, RA Ricciardo, PM Woodward, TL Gustafson, LJ Brillson, and FY Yang. Characterization of electronic structure and defect states of thin epitaxial $BiFeO_3$ films by uv-visible absorption and cathodoluminescence spectroscopies. *Applied Physics Letters*, 92(22):2901, 2008.

[212] Ivan Mora-Seró and Juan Bisquert. Fermi level of surface states in TiO_2 nanoparticles. *Nano Letters*, 3(7):945–949, 2003.

[213] K Vasanth Kumar, K Porkodi, and F Rocha. Langmuir–hinshelwood kinetics–a theoretical study. *Catalysis Communications*, 9(1):82–84, 2008.

[214] Mustafa Supur, Yusuke Yamada, Mohamed E El-Khouly, Tatsuhiko Honda, and Shunichi Fukuzumi. Electron delocalization in one-dimensional perylenediimide nanobelts through photoinduced electron transfer. *The Journal of Physical Chemistry C*, 115(30):15040–15047, 2011.

[215] Ashu Zhu, Qidong Zhao, Xinyong Li, and Yong Shi. $BiFeO_3/TiO_2$ nanotube arrays composite electrode: Construction, characterization, and enhanced photoelectrochemical properties. *ACS applied materials & interfaces*, 6(1):671–679, 2013.

[216] Indhumati Paramasivam, Himendra Jha, Ning Liu, and Patrik Schmuki. A review of photocatalysis using self-organized TiO_2 nanotubes and other ordered oxide nanostructures. *Small*, 8(20):3073–3103, 2012.

[217] MS Hanay, S Kelber, AK Naik, D Chi, S Hentz, EC Bullard, E Colinet, L Duraffourg, and ML Roukes. Single-protein nanomechanical mass spectrometry in real time. *Nature Nanotechnology*, 7(9):602–608, 2012.

Appendices

Appendix A

Analytical model for the theory of BMC

We have solved the one dimensional heat equation presented in Chapter 3 for the theory of BMC using Finite Difference method with the help of Mathematica software. The code used to solve the equation along with parameters are shown in Fig. A.1

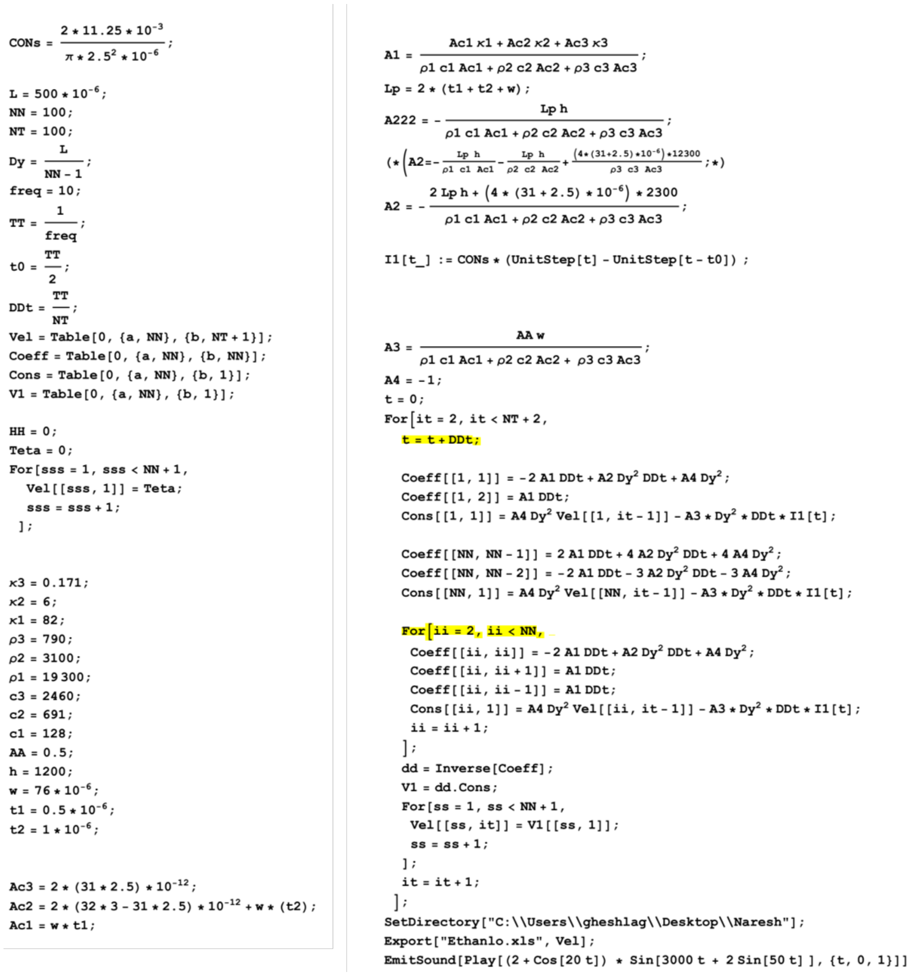

```
CONs = (2 * 11.25 * 10^-3)/(π * 2.5^2 * 10^-6);

L = 500 * 10^-6;
NN = 100;
NT = 100;
Dy = L/(NN - 1);
freq = 10;
TT = 1/freq;
t0 = TT/2;
DDt = TT/NT;
Vel = Table[0, {a, NN}, {b, NT + 1}];
Coeff = Table[0, {a, NN}, {b, NN}];
Cons = Table[0, {a, NN}, {b, 1}];
V1 = Table[0, {a, NN}, {b, 1}];

HH = 0;
Teta = 0;
For[sss = 1, sss < NN + 1,
  Vel[[sss, 1]] = Teta;
  sss = sss + 1;
 ];


κ3 = 0.171;
κ2 = 6;
κ1 = 82;
ρ3 = 790;
ρ2 = 3100;
ρ1 = 19300;
c3 = 2460;
c2 = 691;
c1 = 128;
AA = 0.5;
h = 1200;
w = 76 * 10^-6;
t1 = 0.5 * 10^-6;
t2 = 1 * 10^-6;


Ac3 = 2 * (31 * 2.5) * 10^-12;
Ac2 = 2 * (32 * 3 - 31 * 2.5) * 10^-12 + w * (t2);
Ac1 = w * t1;
```

```
A1 = (Ac1 κ1 + Ac2 κ2 + Ac3 κ3)/(ρ1 c1 Ac1 + ρ2 c2 Ac2 + ρ3 c3 Ac3);
Lp = 2 * (t1 + t2 + w);
A222 = -(Lp h)/(ρ1 c1 Ac1 + ρ2 c2 Ac2 + ρ3 c3 Ac3);
(*(A2=-(Lp h)/(ρ1 c1 Ac1)-(Lp h)/(ρ2 c2 Ac2)+((4*(31+2.5)*10^-6)*12300)/(ρ3 c3 Ac3);*)
A2 = -(2 Lp h + (4 * (31 + 2.5) * 10^-6) * 2300)/(ρ1 c1 Ac1 + ρ2 c2 Ac2 + ρ3 c3 Ac3);

I1[t_] := CONs * (UnitStep[t] - UnitStep[t - t0]) ;



A3 = (AA w)/(ρ1 c1 Ac1 + ρ2 c2 Ac2 +  ρ3 c3 Ac3);
A4 = -1;
t = 0;
For[it = 2, it < NT + 2,
  t = t + DDt;

  Coeff[[1, 1]] = -2 A1 DDt + A2 Dy^2 DDt + A4 Dy^2;
  Coeff[[1, 2]] = A1 DDt;
  Cons[[1, 1]] = A4 Dy^2 Vel[[1, it - 1]] - A3 * Dy^2 * DDt * I1[t];

  Coeff[[NN, NN - 1]] = 2 A1 DDt + 4 A2 Dy^2 DDt + 4 A4 Dy^2;
  Coeff[[NN, NN - 2]] = -2 A1 DDt - 3 A2 Dy^2 DDt - 3 A4 Dy^2;
  Cons[[NN, 1]] = A4 Dy^2 Vel[[NN, it - 1]] - A3 * Dy^2 * DDt * I1[t];

  For[ii = 2, ii < NN,
   Coeff[[ii, ii]] = -2 A1 DDt + A2 Dy^2 DDt + A4 Dy^2;
   Coeff[[ii, ii + 1]] = A1 DDt;
   Coeff[[ii, ii - 1]] = A1 DDt;
   Cons[[ii, 1]] = A4 Dy^2 Vel[[ii, it - 1]] - A3 * Dy^2 * DDt * I1[t];
   ii = ii + 1;
  ];
  dd = Inverse[Coeff];
  V1 = dd.Cons;
  For[ss = 1, ss < NN + 1,
   Vel[[ss, it]] = V1[[ss, 1]];
   ss = ss + 1;
  ];
  it = it + 1;
 ];
SetDirectory["C:\\Users\\gheshlag\\Desktop\\Naresh"];
Export["Ethanlo.xls", Vel];
EmitSound[Play[(2 + Cos[20 t]) * Sin[3000 t + 2 Sin[50 t] ], {t, 0, 1}]]
```

Figure A.1: Mathematica code to solve the one dimensional heat equation using Finite Difference (FD)method

Appendix B

Basics of QCL modules

B.1 Description

QCL is a broadly tunable mid IR laser ranging from 6 μm to 12 μm and provide continuous tuning up to 100 cm^{-1}. Generally they come with a pulse repetition rate of 100 kHz and a duty cycle of 5%. At 5% duty cycle, the pulse width of 100 kHz IR wave is 500 ns. Both of these can be controlled using a controller. Laser can be operated in internal pulse mode or external trigger mode. The IR pulses can be electrically modulated by running a burst square wave using a function generator in external trigger mode. Note that the laser is pulsed not continuous. Individual QCLs have their own range of IR wavenumbers that have been mentioned on the laser head whereas MIR cat is an ensemble of 4 QCLs controlled by a computer program. MIRcat has a motor inside to move from one QCL to other. The average IR power output from a QCL varies with wavenumber, having maximum power at central wavenumbers. Every QCL has its own power spectrum and average power output. In general the average power output is less than 5 mW. Note that the peak power is more than 250 mW because of the duty cycle. The laser controller is communicated to a PC using a RS 232 or GPIB interface. The IR spot has a minimum diameter of 2.5 mm. The mid IR range is suitable for exciting molecular resonances of many organic compounds and associated bonds thus used in molecular spectroscopy.

B.2 Working principle

QCLs are semiconductor lasers that emit mid to far infrared IR through the use of intersubband transitions in a repeated stack of semiconductor multiple quantum well heterostructures. QCL consists of a periodic series of thin layers of varying material composition forming a superlattice. The superlattice introduces a varying electric potential across the length of the device producing one-dimensional multiple quantum well confinement and leads to the splitting of the band of permitted energies into a number of discrete electronic subbands. By suitable design of the layer thicknesses it is possible to engineer a population inversion between two subbands in the system which is required in order to achieve laser emission. Since the position of the energy levels in the system is primarily determined by the layer thicknesses and not the material, it is possible to tune the emission wavelength of QCLs over a wide range in the same material system. In QCL, once an electron has undergone an intersubband transition and emitted a photon in one period of the superlattice, it can tunnel into the next period of the structure where another photon can be emitted. This process of a single electron causing the emission of multiple photons as it traverses through the QCL structure gives rise to the name cascade and makes a quantum efficiency of greater than unity possible which leads to higher output powers than semiconductor laser diodes.

The laser head is connected to a controller that can be externally triggered. The communication to PC can be done through a GPIB interface. QCL can be operated in scan mode with a desired scan rate as high as 50 cm^{-1} per second or can be operated in step mode where the laser communicates to a program to step to a wavenumber and take lock in amplifier readings. The laser can be operated in both the directions and for infinite loops. Lab view programs for MIRcat are yet to be developed. We have two QCLs (1760 to 1656 cm^{-1}(UT 6) and 1410 to 1145 cm^{-1} (UT 8)), MIRcat (1650 cm^{-1} to 820 cm^{-1}) .

The peak power output of the laser varies with IR wavenumber and the drive current. At maximum drive current the IR peak power from MIRcat is shown in B.1. The specifications of UT 6 (1760-1565 cm^{-1}) are shown in Fig. B.2. The details of UT 8 (1410-1145 cm^{-1})are presented in Fig. B.3

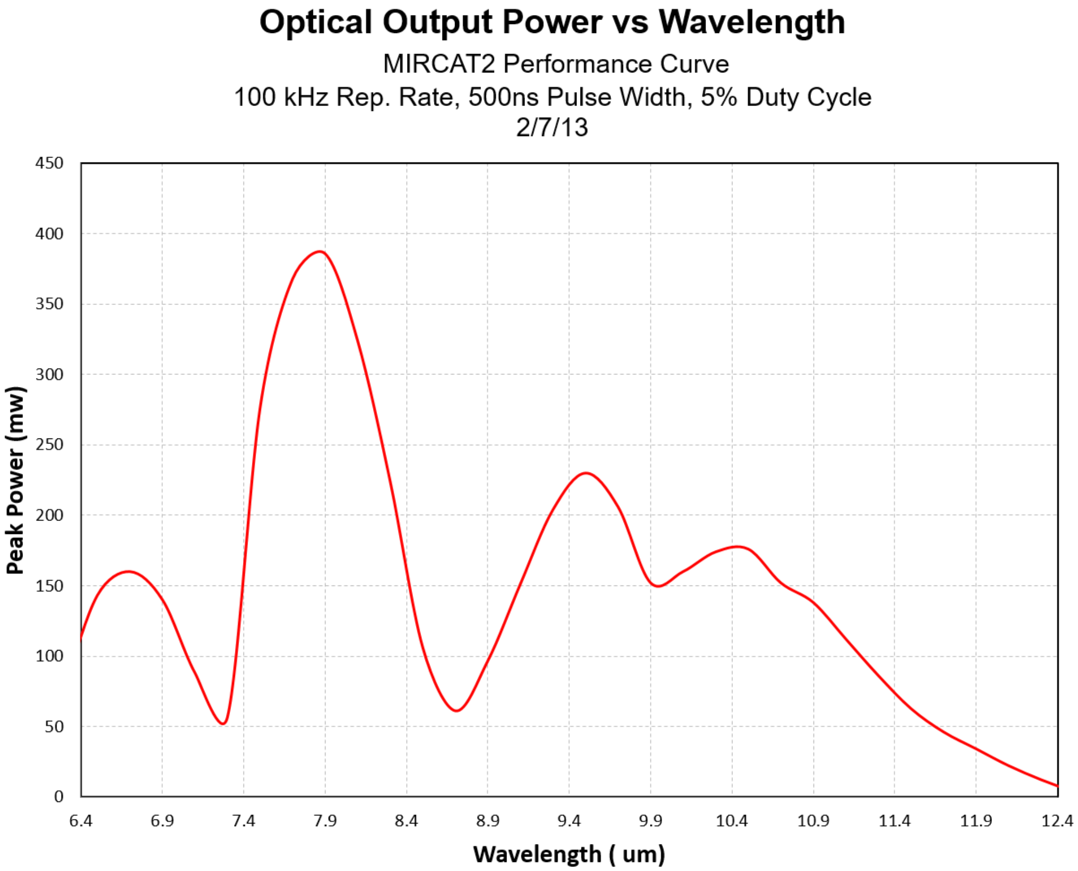

Figure B.1: Peak output power of MIRcat with respect to IR wavenumber at 100 kHZ repetition rate at 5 % duty cycle.

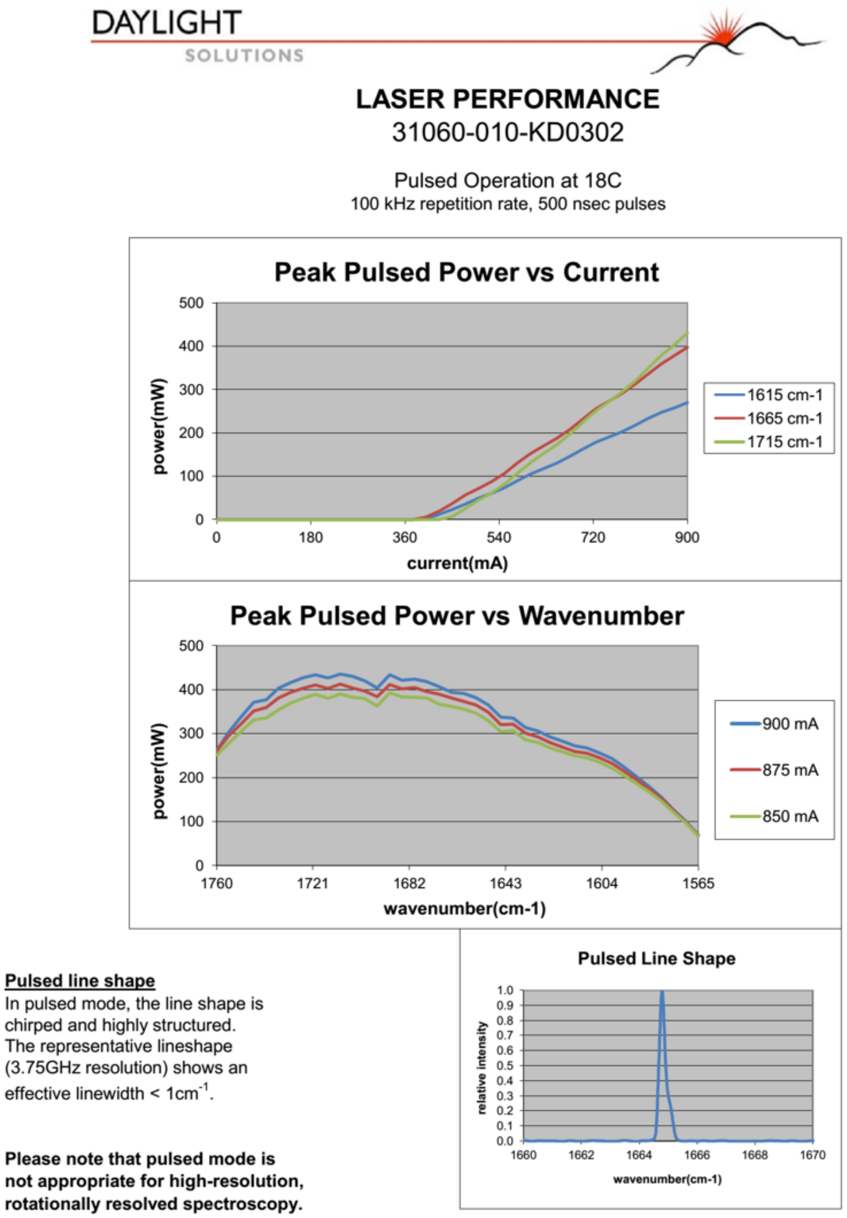

DAYLIGHT
SOLUTIONS

LASER PERFORMANCE
31060-010-KD0302

Pulsed Operation at 18C
100 kHz repetition rate, 500 nsec pulses

Peak Pulsed Power vs Current

Peak Pulsed Power vs Wavenumber

Pulsed Line Shape

Pulsed line shape
In pulsed mode, the line shape is chirped and highly structured. The representative lineshape (3.75GHz resolution) shows an effective linewidth < 1cm^{-1}.

Please note that pulsed mode is not appropriate for high-resolution, rotationally resolved spectroscopy.

Figure B.2: Peak output power of UT 6 with respect to IR wavenumber at 100 kHZ repetition rate at 5 % duty cycle.

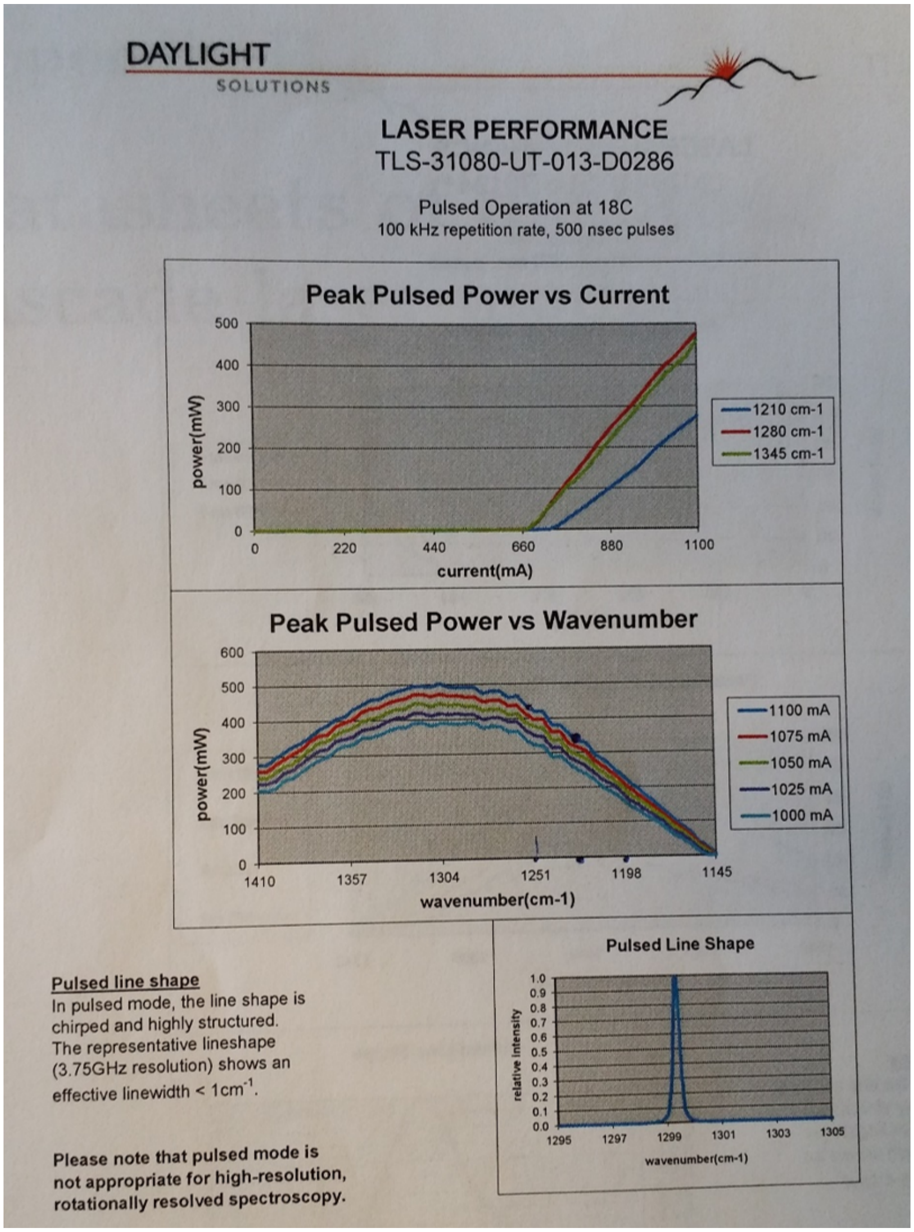

DAYLIGHT
SOLUTIONS

LASER PERFORMANCE
TLS-31080-UT-013-D0286

Pulsed Operation at 18C
100 kHz repetition rate, 500 nsec pulses

Pulsed line shape
In pulsed mode, the line shape is chirped and highly structured. The representative lineshape (3.75GHz resolution) shows an effective linewidth < 1cm^{-1}.

Please note that pulsed mode is not appropriate for high-resolution, rotationally resolved spectroscopy.

Figure B.3: Peak output power of UT 8 with respect to IR wavenumber at 100 kHZ repetition rate at 5 % duty cycle.

Appendix C

Specifications of PSD from SiTek

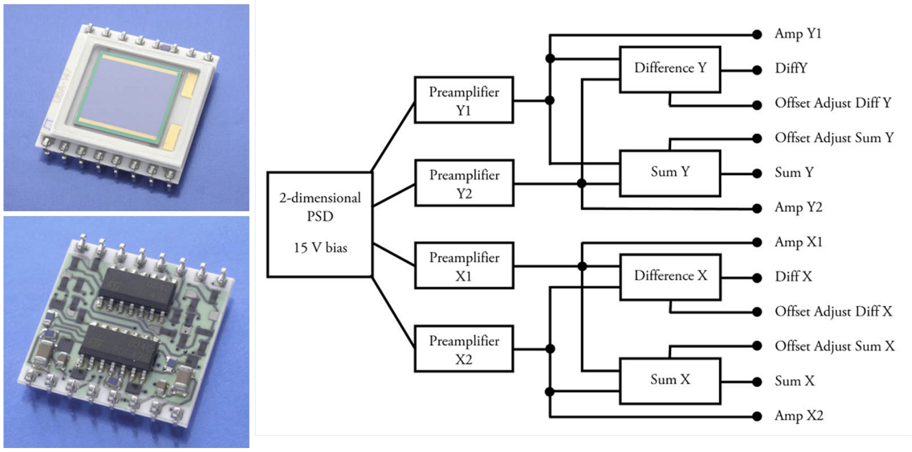

Figure C.1: Block diagram of the PSD.

The photosensitive detector used in the current thesis was purchased from SiTeck numbered S2-0171. The S2-0171 PSD belongs to a category of 2L10-SU65-SPC01. When light of sufficient energy falls on to the PSD, it produces photo currents as the output. As the PSD is under a bias voltage of 15 V, these output currents are directed as shown in the block diagram in right side of Fig. C.1. The position and intensity of the centroid of the light spot can be accurately measured. The difference in the Y signals at two different locations are referred as vertical displacement. All the values presented in the thesis are normalized by SUM value as the signals have dependence over the intensity of the light. To ensure repeatable measurements we have always maintained the laser spot to be focused to a fine diameter less than the width of the device under study. This PSD comes with an attached signal processing unit at the back. The images of the SPC-PSD can be seen from left side of Fig. C.1. Detailed Electrical specifications are found in Fig.C.2.

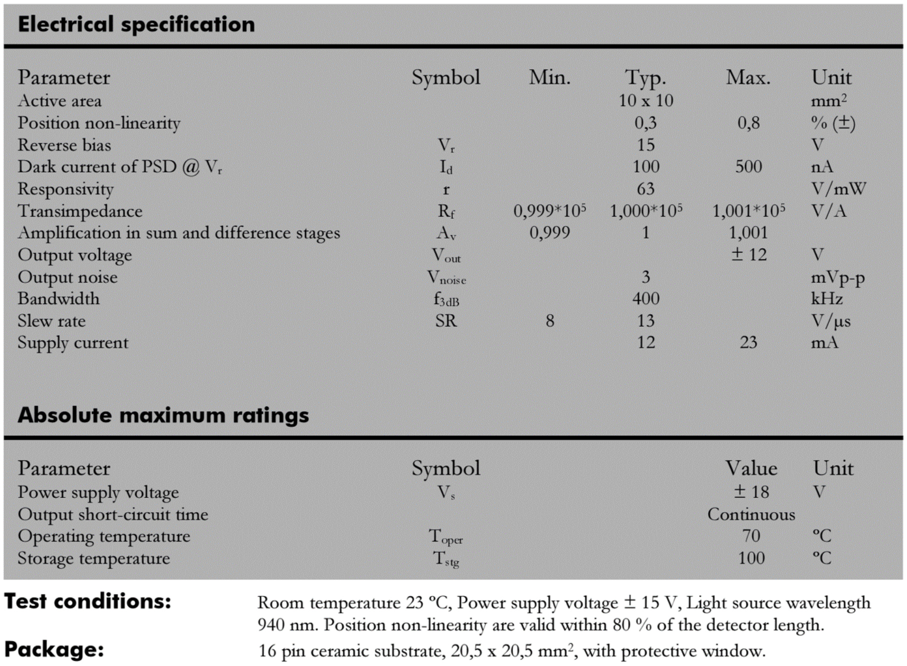

Electrical specification

Parameter	Symbol	Min.	Typ.	Max.	Unit
Active area			10 x 10		mm^2
Position non-linearity			0,3	0,8	% (±)
Reverse bias	V_r		15		V
Dark current of PSD @ V_r	I_d		100	500	nA
Responsivity	r		63		V/mW
Transimpedance	R_f	$0{,}999 * 10^5$	$1{,}000 * 10^5$	$1{,}001 * 10^5$	V/A
Amplification in sum and difference stages	A_v	0,999	1	1,001	
Output voltage	V_{out}			± 12	V
Output noise	V_{noise}		3		mVp-p
Bandwidth	f_{3dB}		400		kHz
Slew rate	SR	8	13		V/µs
Supply current			12	23	mA

Absolute maximum ratings

Parameter	Symbol	Value	Unit
Power supply voltage	V_s	± 18	V
Output short-circuit time		Continuous	
Operating temperature	T_{oper}	70	ºC
Storage temperature	T_{stg}	100	ºC

Test conditions: Room temperature 23 ºC, Power supply voltage ± 15 V, Light source wavelength 940 nm. Position non-linearity are valid within 80 % of the detector length.

Package: 16 pin ceramic substrate, 20,5 x 20,5 mm^2, with protective window.

Figure C.2: Electrical specifications of the PSD.

Appendix D

Projects involved

Title: Vibrational energy harvesting using Photo patternable Piezoelectric polymer nanocomposite MEMS devices
Objective: To fabricate a polymer piezoelectric nanocomposite microcantilevers that can resonate at environmental vibrations and harvest the energy.
Team members: Naresh Miriyala, Dr. Kovur Prashanthi, and Dr. Thomas Thundat

Title: Investigation of anomalous photo properties of BFO NTs
Objective: To explore the effect of surface states and defects on optoelectronic properties of BFO nanostructures. To demonstrate enhanced applications of photocatalytic activity using BFO NTs
Team members: Naresh Miriyala, Dr. Kovur Prashanthi, and Dr. Thomas Thundat

Title: Photothermal and Photoacoustic spectroscopy of trace analytes using microcantilevers
Objective: To evaluate photothermal and photoacoustic signals generated from IR absorption using a bimaterial microcantilever
Team members: Naresh Miriyala, Dr. Dongkyu Lee, Inseok Chae, and Dr. Thomas Thundat

Title: Polymer modified QTF as thermal sensors
Objective: To investigate the thermal sensitivity of polymer modified QTF in photothermal techniques
Team members: Naresh Miriyala, Dr. Xunchen Liu and Dr. Thomas Thundat

Title: Photothermal spectroscopy of femtogram level analytes using nanomechanical strings
Objective: To establish nanomechanical strings as excellent thermal sensors and demonstrate their application in molecualr identification using photothermal techniques
Team members: Naresh Miriyala, Tushar Biswas, Dr. Xunchen Liu, Dr. Thomas Thundat, and Dr. John P Davis

Title: Thermomechnaical behavior of bimaterial microchannel cantilevers under periodic IR
Objective: To investigate the thermomechanical behavior of BMC to address molecular identification in biosensing applications
Team members: Naresh Miriyala, Dr. Faheem Khan, and Dr. Thomas Thundat

Appendix E

Publications

E.1 Journal papers

1. K Prashanthi, **M Naresh**, V Seena, T Thundat, and V Ramgopal Rao. A novel photoplastic piezoelectric nanocomposite for mems applications. Microelectromechanical Systems, Journal of, 21(2):259-261, 2012.

2. K Prashanthi, **N Miriyala**, RD Gaikwad, W Moussa, V Ramgopal Rao, and T Thundat. Vibtrational energy harvesting using photo-patternable piezoelectric nanocomposite cantilevers. Nano Energy, 2(5):923-932, 2013.

3. **N Miriyala**, K Prashanthi, and T Thundat. Oxygen vacancy dominant strong visible photoluminescence from $BiFeO_3$ nanotubes. physica status solidi (RRL)-Rapid Research Letters, 7(9):668-671, 2013.

4. TS Biswas, **N Miriyala**, C Doolin, X Liu, T Thundat, and JP Davis. Femtogram-scale photothermal spectroscopy of explosive molecules on nanostrings. Analytical chemistry, 86(22):11368-11372, 2014.

5. K Prashanthi, P Dhandharia, **N Miriyala**, R Gaikwad, D Barlage, and T Thundat. Enhanced photo-collection in single $BiFeO_3$ nanowire due to carrier separation from radial surface field. Nano Energy, 13:240-248, 2015.

6. TS Biswas, Jin Xu, **N Miriyala**, C Doolin, T Thundat, JP Davis, and KSD Beach. Time-resolved mass sensing of a molecular adsorbate nonuniformly distributed along a nanomechnical string. Physical Review Applied, 3(6):064002, 2015.

7. **N Miriyala**, K Prashanthi and T Thundat. Magnetically separable ultra-thin-wall bismuth ferrite nanotubes with enhanced visible light photocatalytic activity. Manuscript ready for submission
8. **N Miriyala**, M F Khan and T Thundat. Thermomechanical behavior of bimaterial microchannel cantilevers under periodic IR radiation. Manuscript ready for submission
9. M F Khan, **N Miriyala**, J Lee, M Hassanpourfard, A Kumar and T Thundat. Rapid and low volume heat capacity measurement using bimaterial microchannel cantilever based micro-calorimeter. Manuscript ready for submission
10. **N Miriyala**, T S Biswas, J P Davis and T Thundat. Dynamic thermomechanical behavior of nanomechanical strings. Manuscript in progress

E.2 Conference participation

1. K Prashanthi, M Naresh, V Seena, T Thundat, and V Ramgopal Rao. A Novel Photoplastic Piezoelectric Nanocomposite for MEMS Applications, 8 th International workshop on Nanomechanical Sensing, May 2011, Dublin, Ireland
2. K Prashanthi, Naresh Miriyala and T Thundat. UV assisted photo-transport mechanism in multiferroic nanowires and its applications in chemical sensing, 9 th International workshop on Nanomechanical Sensing, June 2012, Mumbai, India
3. Naresh Miriyala, K Prashanthi and T Thundat. Enhanced Visible-light Photocatalytic Activity in ultra thin Bismuth Ferrite nanotubes", 9 th International workshop on Nanomechanical Sensing, June 2012, Mumbai, India.